Manipulating Light with Carbon Nitride Thin Films

Towards applications in metamaterials with organic polymeric carbon-nitride-based optical devices

---

vorgelegt von

Julya Stein Siena, M.Sc.

ORCID: 0000-0001-7412-7715

von der Fakultät II – Mathematik und Naturwissenschaften der
Technischen Universität Berlin
zur Erlangung des akademischen Grades

Doktor der Ingenieurwissenschaften
– Dr.-Ing. –

genehmigte Dissertation

Promotionsausschuss:

Vorsitzender: Prof. Dr. Reinhard Schomäcker

Gutachter: Prof. Dr. Dr. hc Markus Antonietti

Gutachter: Prof. Dr. Arne Thomas

Tag der wissenschaftlichen Aussprache: 10.08.2021

Berlin 2022

ACKNOWLEDGEMENTS

First of all, I would like to express my gratitude to everyone that was involved in this work somehow. It would have been impossible to complete any of the projects without the amazing team work with all my collaborators, thank you: Dr. Harry Mönig and Bertram Schulze Lammers for the in situ experiments and XPS analysis, Corinna Kaspar and Dr. Wolfram Pernice for the waveguides patterning and characterization, Dr. Cédric Boissiere for the EPP experiments, Dr. Thomas Kühne and Julian Heske for DTF calculations, Dr. Michael Tovar for XRD measurements, Oliver Oßwald and Prof. Dr. Bernd Smarsly for XRD fitting, Dr.-Ing. Oliver Görke for UV-VIS-NIR spectroscopy, Dr. Shahrouz Amini for nanoindentation tests, Prof. Dr. Ortwin Hess and Dr. Daniel Clarke for the help with the early stage development of the fishnet metamaterial, and so many others for great discussions, teaching, and advice: Dr. Glenna Drisko, Prof. Dr. Silvia Vignolini, Dr. Nadja Tarakina, Dr. Joao Robalo, among others.

I would like to offer my special thanks to Prof. Markus Antonietti, which was not only my supervisor but someone to have constructive discussions in every field. Thank you for giving me a tiny bit of your knowledge, for feeding my trust in science with a musician balance, and for the opportunity to work at MPIKG.

Many thanks to my co-supervisor Prof. Dr. Arne Thomas, for all the patience and fruitful discussions.

I really much appreciate the work of every technician I had help from: Reinhild Dünnebacke, Regina Rothe, Bolortuya Badamdorj, Heike Runge, Ursula Lubahn, and Jessica Brandt.

I also want to express my most profound gratitude to my parents, Ronaldo and Neuza, my sisters, Íria and Sully, and my nephews, Francesco, Lorenzo, and Frederico, for all the invaluable support and encouragement and for getting on so well with the long-distance journey I went for. Eu amo vocês demais. Thank you to my fiancé, Ivan Ilic, for making everything lighter during the last years and for supporting me unconditionally, besides teaching me some hardcore chemistry.

Lastly, I would like to thank all my friends and colleagues that were there with me during the whole process: Nieves (tea times were very necessary), Nikki (thank you also for the help with the thesis), Christene, Diana, Cansu (special thanks to you for all the care always), Ale, Esther, Milena, Ralf, Joao (meu portuga preferido), Tania (minha portuga preferida), Enrico, Agata, Bradley, Ipek, Marius, Stefano, Francesco, Baris, Volker, Majd, and Vale. In addition, I would like to thank my friends from all over the world for the company and for keeping my mind in the real world (here friends from my hometown, bachelors, masters, and many others).

Thank you all,

J.S.

“All that we see or seem is but a dream within a dream.”

Edgar Allan Poe, "A Dream Within a Dream" l. 10 (1849)

ABSTRACT

Polymeric carbon nitride (pCN) has emerged as a material with desirable optical and mechanical properties for optical and photonic devices. In this thesis, the high intrinsic refractive index and transparency through the visible part of the spectrum in pCN thin films were investigated and explored as potential parameters to guide and manipulate light in optical devices. Inserting the thin film properties in the field of artificially micro- and nanoengineered materials has created many possibilities, which has led this work to the fabrication of organic pCN-based waveguides and a proposition for low-loss flexible fishnet metamaterials.

In the first part of the thesis, the optical dispersion properties, composition, and structure of pCN thin films were investigated as a function of the key parameters employed in the chemical vapor deposition (CVD) process. Changes in the real and imaginary parts of the refractive index, C/N ratio, and morphology occurred with changing the precursor amount, the polymerization time, and the carrier gas flow rate. Non-zero values of the extinction coefficient in the out-of-plane have revealed a high optical anisotropy of the thin films, which is addressed to changes in composition and molecular orientation. In addition, the results also show possible routes to avoid gas-phase nucleation and increased roughness.

On-surface polymerization in situ studies on the polymerization mechanism, from the precursor melamine to pCN thin films, conclude that polymeric carbon nitride is composed of three different coexisting phases with different hydrogen bonding patterns.

In the second part of the thesis, polymeric carbon nitride-based photonic devices for telecommunication wavelengths are demonstrated. The high ordinary refractive index of the polymer of around 2, covering the visible and near-infrared wavelength range, enables small footprint devices, strong mode confinement, and efficient coupling through grating couplers. Proof-of-concept experiments with microring resonators show a Q-factor of 11721 for a wavelength of 1550 nm, meaning a propagation loss of about 31.32 dB/cm. Losses can be further improved with an optimized fabrication process.

Lastly, a new organic pCN-based low-loss metamaterial is proposed as a new artificially nanoengineered material to achieve properties and functionalities that are non-existent in natural materials. In this approach, a double fishnet of gold is alternated with pCN as the dielectric material, offering a flexible device able to achieve negative and zero refractive index.

KURZDARSTELLUNG

Polymeres Kohlenstoffnitrid (pCN) hat sich als ein Material mit wünschenswerten optischen und mechanischen Eigenschaften für optische und photonische Komponenten entwickelt. In dieser Arbeit wurden der hohe intrinsische Brechungsindex und die Transparenz von pCN-Dünnschichten im sichtbaren Teil des elektromagnetischen Spektrums untersucht und als potenzielle Parameter zur Leitung und Manipulation von Licht in optischen Komponenten erforscht. Die Nutzung von Dünnschichteigenschaften schafft viele Möglichkeiten im Bereich der synthetischen mikro- und nanotechnologischen Materialien, die in dieser Arbeit zur Herstellung von organischen pCN-basierten Wellenleitern und zu einem Vorschlag für verlustarme flexible Fischnetz-Metamaterialien führten.

Im ersten Teil der Arbeit wurden die optischen Dispersionseigenschaften, die Zusammensetzung und die Struktur von pCN-Dünnschichten in Abhängigkeit der Schlüsselparameter des chemischen Gasphasenabscheidungsprozesses (CVD) untersucht. Änderungen des Real- und Imaginärteils des Brechungsindex, des C/N-Verhältnisses und der Morphologie traten bei Änderung der Präkursormenge, der Polymerisationszeit und des Trägergasdurchsatzes auf. Nicht-Nullwerte des Extinktionskoeffizienten in der Out-of-Plane offenbarten eine hohe optische Anisotropie der Dünnschichten, die auf Änderungen der Zusammensetzung und der molekularen Orientierung zurückzuführen ist. Darüber hinaus zeigen die Ergebnisse auch mögliche Wege zur Vermeidung von Gasphasennukleation und erhöhter Rauigkeit auf.

In-situ-Studien zum Polymerisationsmechanismus vom Ausgangsstoff Melamin bis zu den pCN-Dünnschichten zeigen außerdem, dass das polymere Kohlenstoffnitrid aus drei verschiedenenmkoexistierenden Phasen mit unterschiedlichen Wasserstoffbrückenbindungs-mustern besteht.

Im zweiten Teil der Arbeit werden auf polymerem Kohlenstoffnitrid basierende photonische Bauelemente für Telekommunikationswellenlängen demonstriert. Der hohe ordentliche Brechungsindex des Polymers von etwa 2 im sichtbaren und nahinfraroten Wellenlängenbereich ermöglicht Bauelemente mit kleiner Grundfläche, starkem Modeneinschluss und effizienter Kopplung über Gitterkoppler. Proof-of-Concept-Experimente mit Mikroring-Resonatoren zeigen einen Q-Faktor von 11721 für eine Wellenlänge von 1550

nm, was zu einem Ausbreitungsverlust von etwa 31,32 dB/cm führt. Die Verluste können durch einen optimierten Herstellungsprozess weiter verringert werden.

Abschließend wird ein neues organisches pCN-basiertes verlustarmes Metamaterial als innovatives synthetisches Nanomaterial vorgeschlagen, um Eigenschaften und Funktionalitäten zu erreichen, die in natürlichen Materialien nicht existieren. Bei diesem Ansatz alterniert ein doppeltes Fischnetz aus Gold mit pCN als Dielektrikum, wodurch ein flexibles Bauelement entsteht, mit dem ein negativer oder ein Null-Brechungsindex erreicht werden kann.

LIST OF FIGURES

Chapter 2

Chapter 3

Chapter 4

Chapter 5

Chapter 6

NOTATION

ε – electric permittivity

μ – magnetic permeability

n – refractive index

k – extinction coefficient

AFM – atomic force microscopy

CMOS – complementary metal-oxide-semiconductor

CVD – chemical vapor deposition

DFT – density functional theory

EBL – electron beam lithography

EDX – energy dispersive x-ray spectroscopy

EM – electromagnetic waves

EPP – environmental ellipsometry porosimetry

FEM – finite element method

FF – filling factor

FFT – fast Fourier transform

FIB – focused ion beam

FSR – free spectral range

HRTEM – high resolution transmission electron microscopy

IC – integrated electronic circuit

K-K – Kramers-Kronig

LPCVD – low pressure chemical vapor deposition

MBE – molecular beam epitaxy

MM – metamaterial

MSE – mean squared error

nc-AFM – non-contact atomic force microscopy

NIL – nanoimprint lithography

NIM – negative index material

NTCDI – naphthalene tetracarboxylic diimide

pCN – polymeric carbon nitride

PIC – photonic integrated circuit

PMMA – poly(methyl methacrylate)

RI – refractive index

RIE – reactive ion etching

RMS – root mean square

SEM – scanning electron microscopy

SOI – silicon on insulator

SRRS – split-ring resonators

STM – scanning tunneling microscopy

TE – transverse electric mode

TEM – transverse electromagnetic mode

TL – Tauc - Lorentz

TM – transverse magnetic mode

TRI – total internal reflection

UHV – ultrahigh vacuum

XPS – x-ray photoelectron spectroscopy

XRD – x-ray diffraction

Contents

Chapter 1

Motivation, objectives and thesis outline

Motivation: Manipulating the interaction between light and matter at the micro- and nanoscale has been a strong and challenging field of research in the last two decades, opening up a whole new branch in modern optics and photonics. Controlling the way light rays move through or bounces off of an object is not an easy task, yet, new artificially engineered subwavelength materials, so-called metamaterials, have arisen to make the unthinkable possible. Although considerable efforts have only been made in recent years to create metamaterials with electromagnetic responses that have never been seen before, the idea behind it has been around for quite some time.

In the late 1960s, the Russian physicist Victor G. Veselago[1] published the first paper in which a hypothetical substance would interact with electromagnetic (EM) waves to give a response well known in the science-fictional universe of wizards: invisibility. Intriguing, right? He theoretically predicted that it was possible to have a material with a negative index of refraction when achieving negative electric permittivity ε (also known as dielectric response) and magnetic permeability μ (magnetic response) simultaneously. As a result, the light would bend backward, in the opposite direction as it does with positive refractive index materials, thus

creating the invisibility-cloaking effect. However, the concept of having a negative refractive index material (NIM) was for some time forgotten.

More than 30 years later, John B. Pendry[2], in addition to Veselago's theory, proposed the design of an artificial material structure known as "superlens" or "perfect lens", which due to the same negative optical constants unlocked the possibility of having super-resolution imaging beyond the diffraction limit. Pendry's research paved the way for the metamaterials field, pushing the boundaries of material design and processing as well as optical characterization methods. New micro- and nanofabrication technologies were developed in the following years, alongside vast improvements in computational capacity and speed, allowing for the simulation and design of devices for specific applications unimaginable with ordinary materials.

In 2000, Smith et al.[3] experimentally demonstrated a composite material featuring negative magnetic permeability for the first time. The authors constructed a periodic array of interspaced pure conducting (nonmagnetic) elements capable of supporting magnetic resonance in the microwave regime by just altering its geometry. That was the first time that artificial magnetism, earlier described by Pendry[4] in 1999, was performed using a magnetic split ring medium consisting of flat little rings with gaps, named split-ring resonators (SRRs). From this moment forth, a massive effort has been made to achieve arbitrary electromagnetic properties up to optical frequencies using materials consisting of artificial atoms (or "meta-atoms"), i.e., an assembly of units that exhibit a particular resonance response to an electromagnetic field – and here is the point where things began to be even more exciting! Within the following years, the metamaterials field was not anymore restricted to NIM (often called "left-handed") or to tiny metallic features. Instead, it was extended to nano- and micro engineered hybrid materials[5], block copolymers[6], conductive oxides[7], chiral materials[8], among others, to achieve a desirable phase-shift, polarization rotation, or amplitude, therefore, bringing on many different possible directions.

Recently, due to the rapid advance in the semiconductor industry, metamaterials are being developed to speed up communication and process information, mainly using high refractive index materials both in the optical and terahertz waveband. Hence, it is of great interest to investigate artificially structured materials that can strongly couple and manipulate light with a

low loss over a wide frequency range, unlocking the possibility of creating flat and flexible optics composed of extremely thin components[9]. Although required metamaterials properties may differ depending on the application, there are desirable characteristics for their development as ease scale down, increased performance, low cost, and nontoxicity. Those, together with the main rule to fulfill the right conditions for light manipulation between the optical and telecommunication ranges - which is to build unit cells much smaller than the target wavelength -, are what bring us here. How can we come up with a high refractive index, flexible and sustainable organic material with such tiny features to manipulate light? Moreover, how can we decrease dissipative losses in optical metamaterials if the composite's unit cells must be much smaller than the working wavelength to satisfy the effective medium theory?

One of the most significant challenges in the metamaterial field is the high loss in metamaterials both in telecommunication and optical frequencies[10]. Large losses severely limit their use in different advanced applications. Hence, new materials and designs which can be used to obtain lower losses are desirable[11]. The introduction of transparent organic polymers with high refractive indices into the metamaterial stacking can help to improve its performance. Carbon nitride thin films have recently been reported to have very unique optical properties, including the highest refractive index attributed to polymeric organic materials, along with high thermal stability and mechanical and electronic properties comparable to that of diamond and graphite[12,13]. Furthermore, organic-based metamaterials can offer interesting novel features compared to inorganic ones due to their ease of fabrication and structural flexibility[14].

Objectives: The purpose of this study is twofold. The first part is geared towards developing uniform, transparent, and flexible carbon nitride thin films with outstanding optical properties, followed by the investigation of the thin film's structure in the atomic scale - since, to this date, no effective characterization has been made to fully understand 2D carbon nitride structure. In the second part, we use nanolithography techniques for waveguiding efficiency and evaluate the optical properties of the micro-/nanostructured thin films for future low-loss organic-based metamaterials applications.

Outline

Understanding the fundamentals of electromagnetic waves is essential to follow up with the characterization methods, and results described further in this thesis. Thus, in **chapter 2,** I will provide some necessary background information on the optics of materials, metamaterials, and dielectrics waveguiding properties. In the following sections, I proceed with a short description of the nanofabrication methods applied for the synthesis and patterning of carbon nitride thin films, followed by a discussion about carbon nitrides, their interesting optical properties, and most reported applications in the literature up to date.

In **chapter 3,** I present a systematic investigation describing the importance of the influence of chemical vapor deposition (CVD) parameters on the composition, structure, morphology, and, most importantly, on the dispersion properties (real and imaginary parts of the refractive index at different wavelengths) of polymeric carbon nitride thin films. Specifically, I explain the relationship between the structure and composition of the thin films and their optical anisotropy. The key characterization method applied in the studies present in this chapter is the ellipsometry spectroscopy, which, in combination with other conventional techniques, provides a roadmap to understand the changes in the optical anisotropy according to the molecular orientation of the thin films.

In **chapter 4,** I provide a remarkable insight into the structure of pCN thin films through an in situ deposition process monitored by low-temperature scanning tunneling microscopy (STM) and non-contact atomic force microscopy (nc-AFM) in UHV. The on-surface polymerization of melamine on Cu(111) has revealed the coexistence of different phases and hydrogen bonding patterns, as well as the formation of a metal-organic hybrid at high temperatures.

In **chapter 5**, I explore, theoretically and experimentally, the waveguiding properties of nanostructured carbon nitride thin films. pCN thin films with just the right stacking and waveguide geometry can provide small footprint devices and strong mode confinement due to their exceptional high refractive index at telecom wavelengths.

In **chapter 6**, I summarize the main results presented in the previous chapters and suggest an exciting idea for a low-loss organic polymeric-carbon nitride-based fishnet metamaterial.

Chapter 2

Background

This work is based on the combination of two distinct subjects: optical metamaterials and polymeric carbon nitride thin films. In this chapter, the fundamentals of these two fields and their recent development of research will be briefly introduced.

2.1 Fundamentals of Optics and Metamaterials

Metamaterials (MMs) are broadly defined as artificially engineered electromagnetic materials designed to have properties beyond the ones we see in nature, hence the prefix “meta”. They are composed of subwavelength dielectric and/or metal structures tailored to provide peculiar responses when exposed to an electromagnetic field. Analogous to the fact that matter consists of atoms, metamaterials are formed by individual structures, termed “meta-atoms”, which control their electromagnetic properties. Because of the considerably much smaller size of the engineered meta-atoms compared to the working wavelength, the incident electromagnetic wave cannot “see” these small features, meaning that the electromagnetic response results from the interaction with the metamaterial as a whole, with no scattering from its little components.

This property may lead to MMs' definition as *effective* homogenous media[9,14]. In this chapter, some concepts related to metamaterials' physics and how they can be applied are reviewed.

2.1.1 Electromagnetic wave theory

"What is light, really?"

A wave as described by Huygens? Or a flow of tiny little particles, as proposed by Newton? Well, yes, and yes (quantum theory!). In the early 19th century, modern optics pulled different concepts together into one when Maxwell, a Scottish physicist, took the previous work of other illustrious physicists and added his own insights to create the electromagnetic theory and the definition of light as we know it today: electromagnetic waves[15]. Macroscopic Maxwell's equations are a set of four partial differential equations that show how electrical and magnetic fields are inextricably linked and are the basis of all light-matter interactions. In vacuum, the classical electromagnetic field can be described by:

$$\nabla \cdot \vec{E} = \frac{\rho}{\varepsilon_0} \tag{2.1}$$

$$\nabla \cdot \vec{B} = 0 \tag{2.2}$$

$$\nabla \times \overrightarrow{E} = -\frac{\partial \vec{B}}{\partial t} \tag{2.3}$$

$$\nabla \times \vec{B} = \mu_0 \left(\varepsilon_0 \frac{\partial \vec{E}}{\partial t} + \vec{J}\right) \tag{2.4}$$

Where $\overrightarrow{E}$ is the electric field and $\vec{B}$ the magnetic flux density vector, both in the presence of a charge function ρ and an electrical current density vector $\vec{J}$. The terms μ_0 and ε_0 are the permeability (magnetic response) and permittivity (electric response) of vacuum, respectively. The divergence condition in Equation 2.2 indicates the absence of magnetic monopoles (no magnetic charges) and is Gauss's Law for a static magnetic field. Equation 2.1 is its analog for the electric field. The last two equations correspond to Faraday's law of induction (2.3), which states that a change in the magnetic field with time produces a circulating electric field, and Maxwell corrected Ampere's law (2.4), expressing that an electric current and electric field create a circulating magnetic field.

In the presence of matter, one needs to reformulate the equations to consider all the light-matter interactions. The equations are now expressed in terms of two other additional fields, $\vec{D}$ (electric displacement) and $\vec{H}$ (magnetizing field), described as:

$$\vec{D} = \varepsilon_0 \vec{E} + \vec{P} \tag{2.5}$$

$$\vec{H} = \frac{\vec{B}}{\mu_0} - \vec{M} \tag{2.6}$$

Where $\vec{P}$ and $\vec{M}$ are the electric and magnetic polarization, respectively. Substituting the Equations 2.5 and 2.6 into Maxwell's and $\vec{P} = \vec{M}$ in free space, the result is:

$$\nabla \vec{D} = \rho \tag{2.7}$$

$$\nabla \vec{B} = 0 \tag{2.8}$$

$$\nabla \times \vec{E} = -\frac{\partial \vec{B}}{\partial t} \tag{2.9}$$

$$\nabla \times \vec{H} = \frac{\partial \vec{D}}{\partial t} + \vec{J} \tag{2.10}$$

Further, fields $\vec{E}$ and $\vec{H}$ are separated by taking the curl of the curl equations 2.9 and 2.10. Considering the speed of light in vacuum as $c = (\mu_0 \varepsilon_0)^{-1/2}$, we obtain a partial differential equation, called wave equation, for both the electric and magnetic fields:

$$\nabla \times \left(\nabla \times \vec{E}\right) = -\mu_0 \varepsilon_0 \frac{\partial^2 \vec{E}}{\partial t^2} = \frac{1}{c^2} \frac{\partial^2 \vec{E}}{\partial t^2} \tag{2.11}$$

$$\nabla \times \left(\nabla \times \vec{H}\right) = -\mu_0 \varepsilon_0 \frac{\partial^2 \vec{H}}{\partial t^2} = \frac{1}{c^2} \frac{\partial^2 \vec{H}}{\partial t^2} \tag{2.12}$$

These wave equations have the same form as Maxwell's macroscopic equations, except that the vacuum constitutive parameters μ_0 and ε_0 are now replaced by the corresponding constants for the medium, μ, and ε, and boundary conditions need to be determined[16,17].

2.1.2 Electrical constants and refractive index

As shown in section 2.1.1, the electromagnetic response of a metamaterial can be described by the two frequency-dependent macroscopic parameters $\mu(\omega)$ and $\varepsilon(\omega)$. Maxwell deduced the speed of travel for electromagnetic waves from his equations when he proved it as being equal to the square root of the relative electric permittivity multiplied by the relative magnetic permeability. This product is called *refractive index* (RI) and is denoted by n. Considering that the speed of light changes as it passes from one medium to another, the phenomena known as refraction, the refractive index can also be defined as the ratio of the speed of light in vacuum to its speed in the medium by the following expression:

$$n = \pm\sqrt{\varepsilon}\mu = \frac{c}{v} \tag{2.13}$$

Most of the materials we usually are dealing with are dielectrics and have a positive ε and a positive μ, which implies that Equation 2.13 gives the refractive index a real number and that light can propagate through such materials. It is possible to organize all the materials existing in nature according to their electric permittivity and magnetic permeability, as seen in Figure 2- 1: Electric permittivity and magnetic permeability diagram. Adapted from18.

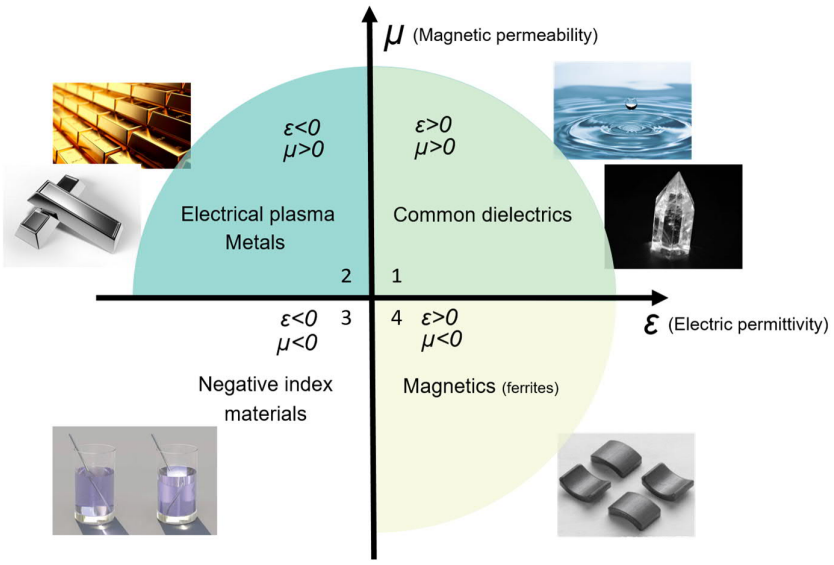

Figure 2- 1: Electric permittivity and magnetic permeability diagram. Adapted from[18].

Materials in the first quadrant include water, crystals, air, and semiconductors.

Moving to the second quadrant, if a 2D material with a negative ε and a positive μ is considered, the refractive index is then the square of a negative number. In this case, the result is purely imaginary, meaning that light cannot propagate through the material. This situation applies to heavily doped semiconductors and metals like gold and silver, which act as plasma at high frequencies. Above the resonance frequency, the external field oscillates too fast for the electrons to follow, and it dies off, creating an evanescent wave. Precisely due to this property, metals can exhibit collective electron charge oscillations, called surface plasmon resonance (SPR), and are able to confine light to extremely small areas, which is the basic idea behind nanophotonics.

In terms of optical frequencies, moving to the fourth quadrant, for natural materials, μ is very close to 1. Up to today, ferrites are the only known material with negative magnetic permeability when excited by electromagnetic waves below the magnetic plasma frequency. It is important to emphasize that natural magnetism at THz frequencies or higher has never been reported, although Pendry already proposed a solution for artificial magnetism using split-ring resonators (SRRs). As depicted in the third quadrant, having a negative RI as a product from

negative permittivity and negative permeability implies that the phase velocity propagates against the normal flux of energy. Let's make a straightforward analogy: when a stone is thrown into a lake, ripples in the water appear to go outwards. If the phase velocity propagates in the "wrong" way, wave ripples would go in the opposite direction. That is the same situation presented in the picture with the straw in a glass filled with a negative index material, the refraction goes backward.

As μ=1 for nonmagnetic materials, one gets $n = \sqrt{\varepsilon}$. Since the electric permittivity is frequency-dependent, the refractive index will also be a function of frequency ω. This wavelength dependence is known as *dispersion*. In transparency regions, the media exhibit normal dispersion, while anomalous dispersion is observed in spectral regions where strong absorption appears. When an electromagnetic wave propagates through a lossy material, it loses its energy by being absorbed or scattered, and the refractive index becomes complex. The real part of the complex RI is n and the imaginary part is the extinction coefficient k, the latter related to the damping of the oscillation amplitude of the incident field. The complex index $\widetilde{N}$ is related to the complex dielectric constant $\tilde{\varepsilon} = \varepsilon_1 - i\varepsilon_2$ and is given by:

$$\widetilde{N} = n - ik = \sqrt{\tilde{\varepsilon}} = \sqrt{(\varepsilon_1 - i\varepsilon_2)} \tag{2.14}$$

Where ε_1 and ε_2 are the real and imaginary parts of ε, respectively. Alternatively, from Equation 2.14, we can also rewrite the complex permittivity components as:

$$\varepsilon_1 = n^2 - k^2 \tag{2.15}$$

$$\varepsilon_2 = 2nk \tag{2.16}$$

If the complex number in Equation 2.14 is real at some particular wavelength, the electromagnetic wave propagates through the material without being absorbed ($k_{(\lambda)} = 0$) and the material is transparent for this specific wavelength.

2.1.3 Snell's Law of refraction

In the previous section, the refractive index concept, a measure of how fast light travels through a medium, was discussed. When an electromagnetic wave crosses a boundary between two different media, the speed of light changes, and the wave vector changes its propagation direction. This bending of the light ray is called *refraction*. Snell's law is used to predict the amount of bend the light ray undergoes through a relationship between the angle of the incident and transmitted waves when they interface at two different media. This refraction law is given by:

$$n_1 sin\theta_1 = n_2 sin\theta_2 \tag{2.17}$$

Where n_1 and n_2 are the RI of the two different media and θ_1 and θ_2 are the angles of incidence and refraction with the normal to the interface, respectively.

Suppose the light wave is incident from a positive RI material into a NIM. In that case, the refracted beam inside the medium is on the same side of the surface normal, as the incident beam[19,20]. In other terms, the refracted light would bend in the opposite direction, as already discussed in section 2.1.2 and shown in Figure 2- 2.

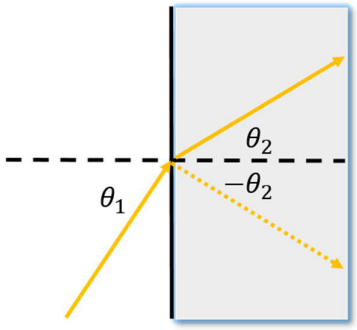

Figure 2- 2: Refraction in a positive refractive index media ($\boldsymbol{\theta_2}$) and a NIM ($-\boldsymbol{\theta_2}$).

2.1.4 Dispersion models in dielectrics

Optical properties of solid materials are usually represented by either the dispersion relation of n and k or ε_1 and ε_2. These material parameters are indirectly retrieved from reflection and transmission coefficients if one assumes that the effective medium is continuous. In this section, the dispersion models used in this thesis to quantify n and k wavelength dependence will be introduced.

A dispersion model is required to effectively provide the optical response as a function of the wavelength. First of all, it is essential to define the Kramers-Kronig (K-K) dispersion relations, which couple the real and imaginary parts of complex functions using integral relations. If the real part of the frequency-dependent complex refractive index n is known, one can use K-K relations to determine the imaginary part k and vice versa. It takes the form of:

$$n(\omega) = \frac{2}{\pi} P \int_0^{\infty} \frac{k(\omega')\omega'}{\omega'^2 - \omega^2} d\omega' \tag{2.18}$$

And

$$k(\omega) = -\frac{2}{\pi} P \int_0^{\infty} \frac{n(\omega')\omega'}{\omega'^2 - \omega^2} d\omega' \tag{2.19}$$

With ω' as the integration variable and P as the Cauchy principal value of the integral. Both equations are analogous for the complex permittivity function components. As per definition, the optical profile of a linear medium should obey the K-K relations[21–23].

One of the dispersion models used in this work is the Cauchy layer model. Its equation is adequate for determining a material's refractive index in the transparent energy range. Such a medium has no absorption in the measured frequency and vicinity, and the real refractive index exclusively describes the optical properties. For most transparent media in the visible spectral range, the index curves slightly upward at shorter wavelengths, a behavior which is well illustrated by the Cauchy dispersion equation:

$$n(\lambda) = A + \left(\frac{B}{\lambda^2}\right) + \left(\frac{C}{\lambda^4}\right) \tag{2.20}$$

Where A, B, and C are material-dependent fitting parameters.

For materials with a bandgap close to the measured spectral range, the primary absorption is precisely modeled by the Tauc-Lorentz (TL) dispersion function using a broad Lorentzian line shape with zero absorption below a defined bandgap energy. That is the case for amorphous semiconducting materials. It is used to parameterize the imaginary part ε_2 of the dielectric function optical constants. The real part ε_1 is obtained through the Kramers-Kronig relation. The TL theoretical model was developed by Jellison and Modine[24], by combining Tauc's joint density of states, which describes interband mechanisms, along with the Lorentz oscillator. The Lorentz model considers electrons to be bound to the nucleus in the atom by a spring-like force. The spring would be set into motion when electromagnetic field-electron interaction occurs, making the electrons oscillate. The Lorentz oscillator model describes this oscillation[25]. Taking both definitions into account, the TL model takes the form of:

$$\begin{cases} \varepsilon_2(E) = 2nk = \frac{AE_0CE}{E^2 - E_0^2 + C^2E^2}; E > E_g \\ \varepsilon_2(E) = 0; E \leq E_g \end{cases} \quad (2.21)$$

Where E_0 is the peak transition energy $E_0 = \hbar\omega_0$, C is the oscillator width, and A is a fitting parameter for the amplitude.

The real part of the dielectric function is obtained from Equation 2.21 by applying K-K relations[26,27].

2.2 Organic-based photonic devices

The precise shape, geometry, size, and arrangement of meta-atoms in metamaterials gives them their ingenious properties capable of manipulating electromagnetic waves either by absorbing, enhancing, blocking, guiding or rotating waves. The integration of organic optical materials into silicon photonics and metamaterials structures is of great industrial interest since it provides highly-efficient and low-cost devices for a wide range of frequencies[28]. Moreover, most optical technologies are currently based on inorganic materials, which are expensive and lossy[29]. The

following section will focus on the two most important topics for the present work: the use of organic-based thin films for waveguiding at telecom wavelengths and hybrid double-fishnet materials for optical loss compensation.

2.2.1 Organic-based optical waveguides

The semiconductor industry continuously develops new and miniaturized integrated circuits and electronic integrating devices to overcome information transmission speed limits. Alternatively to electronics, low cost of production and higher-end performance can be achieved by implementing integrating optics. Thus, using light-based device components could help surpass the bottleneck imposed by the limited wavelength of electronic devices. Low-loss waveguides are fundamental elements in integrated optics, used as optical interconnectors of different circuits. Generally speaking, they are essential in the transmission of high-frequency power, since high-frequency signals cannot travel at long distances without getting attenuated.

The electromagnetic response of waveguides can be designed by patterning arranged nanostructures to achieve specific guiding properties. They can trap electromagnetic waves locally and guide them in a specific direction. A basic patterned slab waveguide design is separated into two regions, one with an increased refractive index (core) and the other with a lower refractive index (cladding), as illustrated in Figure 2- 3.

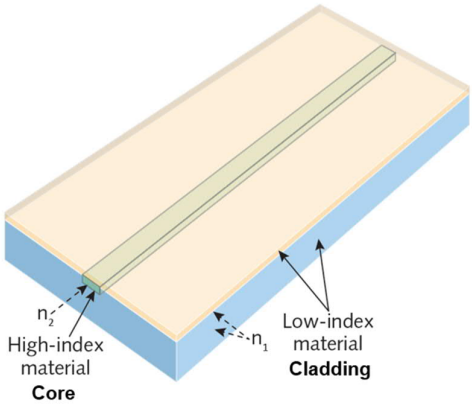

Figure 2- 3: Slab waveguide scheme with higher refractive index (core) and lower refractive index (cladding) regions.

Waveguides can confine light within the core of the system due to total internal reflection (TRI). When light is incident upon the lower RI medium, the ray is bent away from the normal, as we have previously seen in Snell's Law of refraction (Equation 2.17). Hence, the angle with which the ray bends is greater than the incident angle. As the angle of incidence increases, the refracted angle also increases. Considering a critical angle θ_c as an incident angle that produces refraction at 90º, if the light ray enters the lower RI region with an angle greater than θ_c, all the light is reflected back at the boundary between the high RI medium and the lower one, TIR occurs (Figure 2- 4), meaning light doesn't pass through the boundaries, and it is not refracted.

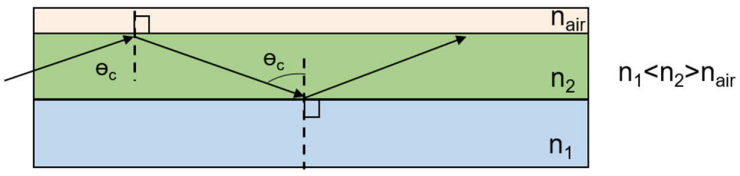

Figure 2- 4: Total internal reflection (TIR) in a slab waveguide.

Starting from the symmetry of the general Maxwell's equations presented in Session 2.1.1, and the interdependence of $\vec{E}$ and $\vec{H}$, we have seen that, in free space, electromagnetic waves are composed of electric and magnetic fields propagating in the same direction of travel but perpendicular to each other. It is easier to visualize it if we take as an example the universe as

we know it - made of space, time, and different fields. Those fields are just a way to assign a value to every point in space and time. Analogous to the ocean surface, where every point has a particular height at a given time, fields have waves that also move through space and time. However, instead of having a simple value as for the height of the ocean waves, electromagnetic waves are described by a vector, with a given direction and magnitude, and oscillates in the direction perpendicular (transverse) to its direction of travel (z, Figure 2- 5).

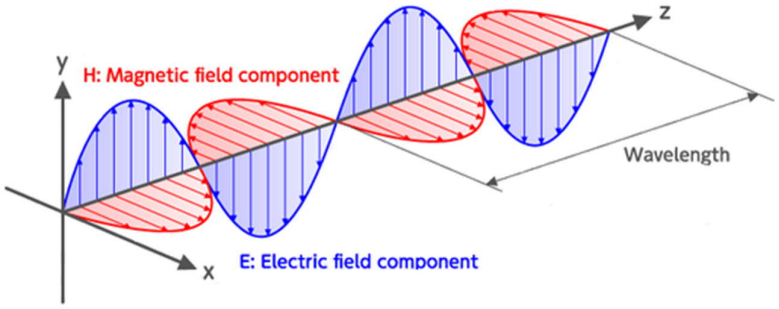

Figure 2- 5: Propagation of an electromagnetic wave with electric ($\vec{E}$) and magnetic ($\vec{H}$) fields transverse to the direction of travel (z).

The manner an electromagnetic wave propagates in a waveguide depends mainly on the boundary conditions imposed by the waveguide's physical properties. It can be conveniently described by the bound, or guided modes of the waveguide, which are solutions of Maxwell's equations[30]. For electromagnetic waves propagating in the longitudinal axis, i.e., the optical axis (z-direction), of a waveguide, the so-called *modes* or *eigenmodes* are classified as follows:

- **TEM** or transverse electromagnetic mode: this waveguide mode is characterized as a wave with both the electric and magnetic field vectors perpendicular to the optical axis of the waveguide, meaning there is no electric or magnetic field in the direction of propagation ($E_z = H_z = 0$). TEM modes are limited to specific geometries where there are two isolated conductors as, for example, in coaxial cables;
- **TE** or transverse electric mode: *TE* waves (also called ***H*** waves) have the electric field perpendicular to the direction of propagation, whereas the magnetic field has components along the direction of propagation ($E_z \neq 0, H_z = 0$);

- **TM** or transverse magnetic mode: *TM* waves (often called ***E*** waves) have a magnetic field but no electric field in the direction perpendicular to the optical axis ($E_z = 0, H_z \neq 0$);
- Hybrid mode: *TE* and *TM* waves are coupled – it has both field vectors in the direction of propagation ($E_z \neq 0, H_z \neq 0$). This mode does not exist in planar waveguides[28].

A dielectric rectangular waveguide only supports *TE* and *TM* modes, both of which can be retrieved through numerical calculation methods. The longitudinal field components E_z and H_z satisfy the scalar Helmholz equation, written as:

$$\nabla_t^2 \psi + k_c^2 \psi = 0 \tag{2.22}$$

Where $k_c^2 = k^2 - k_z^2$. Ψ stands for either E_z or H_z, and k_z is the propagation coefficient. The propagation constants, *k,* are given for a certain frequency, ω, and wavelength, λ.

Furthermore, the transverse field component can be obtained by substituting E_z and H_z into Maxwell's curl equations (Equations 2.9 and 2.10), and expressing the transverse fields in terms of longitudinal fields.

For each waveguide mode, there is an associated *cut-off frequency,* which is dependent on the shape and size of the waveguide. The cut-off value is the lowest frequency in which the mode can propagate with minimal attenuation, meaning the waveguide cannot carry a specific signal below this frequency. In rectangular waveguides, the dominant mode is the T_{10} mode, which is the one that has the lowest cut-off frequency. As seen in the scheme depicted in Figure 2- 6, several transverse electric modes (electric field transverse to the direction of propagation) can propagate through the waveguide, as long as it "fits" its cross-section.

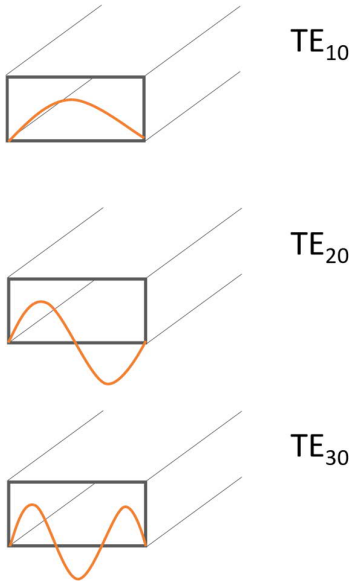

Figure 2- 6: Scheme of different transverse electric (TE) modes in a rectangular waveguide.

Each mode is denoted by TE_{mn} or TM_{mn}, where *m* and *n* represent the number of half-period variations in the field in the *x*-direction and the number of half-period variations in the *y*-direction, respectively. Having only the dominant mode propagating through the waveguide (single-mode condition) is an advantage for signal transmission with low attenuation. The field patterns become much more complex at higher frequencies, making it more challenging to design an efficient waveguide. Moreover, high order modes can couple to lower order modes, resulting in distortions and compromising the signal stability[31,32].

A wide range of materials can be used to fabricate optical waveguides. To this date, most of the commercial guiding optical devices are based on silicon/silica, lithium niobate, and III-V compounds[28]. Novel materials such as high refractive index organic polymers are promising candidates as transparent dielectrics metasurfaces for guiding light combined with lower index substrates, such as silica, or as free-standing patterned thin films. 2D organic materials are highly attractive in the semiconductor industry due to their ease of tunability, low-cost, mechanical flexibility, compatibility with different nanofabrication processes, and reduced toxicity.

2.2.2 Nanofabrication techniques

The development of metamaterials continues to move forward as new fabrication processes at the micro- and nanoscale advance. Most of the existing approaches were created in the semiconductor industry, motivated by Moore's Law (smaller, faster, cheaper), and are generally based on three steps: patterning, depositing, and etching[33]. As a patterning tool, a predominant *top-down* manufacturing approach called *lithography* is applied. This high throughput technique is mainly employed to define 2D and 3D features by removing the bits and pieces from a layer stack until getting the desired pattern size and shape. Pretty much the same process as Michelangelo used to do in marble to get his sculptures done, but on a much smaller scale. Nowadays, there are many methods that use different radiation sources of specific wavelengths for writing and printing micro- and nanostructures, such as photolithography (high throughput but low resolution), nanoimprint lithography (NIL), electron beam lithography (EBL), X-ray lithography, focused ion beam (FIB), and dip-pen lithography. The following section will focus on direct-writing (maskless) submicron patterning processes, specifically EBL and FIB, both used in the present work.

Currently, EBL is the industry-standard technique for high-resolution nanostructuring. It makes use of a highly energetic focused electron beam, which is accelerated towards a surface coated with an electron-sensitive resist thin layer. An example of an EBL process is shown in Figure 2- 7. As the electron beam scans a pre-defined CAD image across the polymeric resist (iii), it induces a chain-scission of the polymer, meaning that the polymer chain breaks into smaller pieces. This process reduces the polymer molecular weight and consequently increases its solubility in organic solvents[34,35]. The exposed area is then removed using a developer (organic solvent) to reveal the designed structure (iv). In this case, the polymer used is a positive resist. If, instead of scission, crosslinking occurs during the electron beam exposure, the polymer becomes insoluble, and it is considered a negative resist. After the development step, the patterns are transferred to the substrate/film by chemical or physical etching processes (v), and the resist thin layer is stripped out of the stacking (vi).

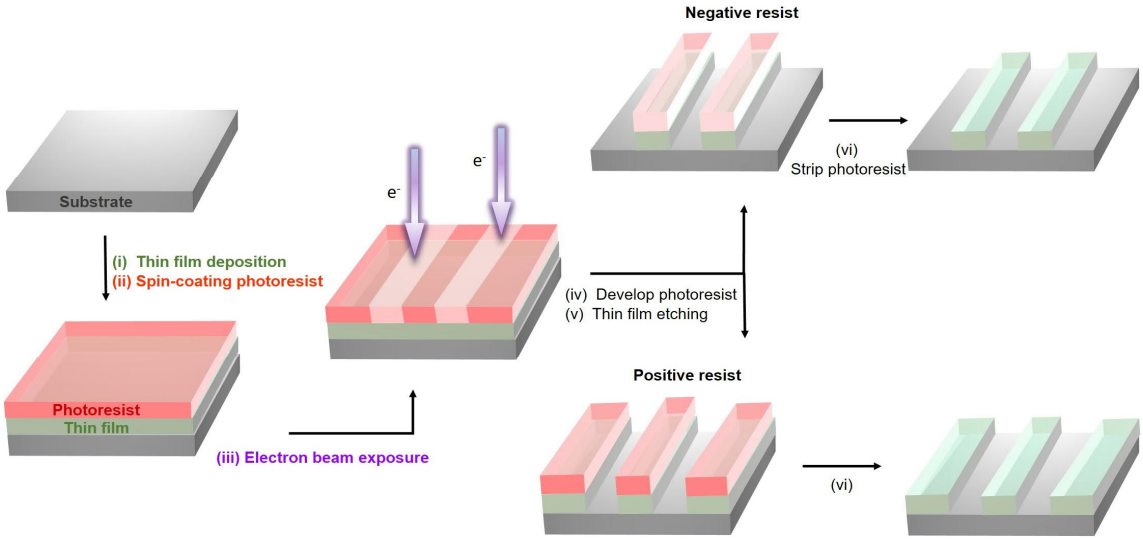

Figure 2- 7: Scheme of electron beam lithography processes considering positive and negative resist.

Due to its high resolution, EBL is used to produce optical communications devices such as waveguide components and other nanoelectronic and photonic systems down to less than 10 nm; it is also a mask-making technique. Although EBL has additional high sensitivity and density, it also presents some complicating factors such as delocalization of electrons in the resist film (forward scattering) and in the substrate (backscattering), which can cause pattern distortion and overexposure, a phenomenon known as the proximity effect. Furthermore, it is a high-cost process.

Another maskless nanofabrication process, called FIB, produces and focuses high energy ionized atoms instead of electrons. With FIB, it is possible to perform etching or milling of surfaces, sometimes with simultaneous imaging. The main difference between both methods is the beam source. Ions have greater mass, slower speed, higher momentum, and smaller penetration depth than electrons. As no backscattering occurs (ions are much heavier and scatter very little), proximity effects are negligible. Nevertheless, it is more challenging to focus the ion beam due to chromatic aberrations. The process is also much more time-demanding in terms of writing speed, and ion contamination/implantation can occur, altering the material's optical properties if direct-writing without a resist is used. Moreover, the most common metal ion source, Ga^+, has extremely limited exposure depth in the resist (<100 nm for 100 keV). In

PMMA, which is one of the most commonly used resists, it doesn't exceed 60 nm[36]. Considering the time of processing for high-resolution nanostructures, the preferred lithography method used in this thesis was EBL, whilst FIB was used as a proof of concept.

As previously mentioned, patterning and etching are not the only steps within a nanofabrication process, and neither are top-down approaches. Nanotechnology manufacturing of complex systems merges both top-down and *bottom-up* techniques, using the first one to miniaturize the components of an optical or electronic device and, the second one, to build up molecular blocks atom by atom. The latter case is applied to the deposition step of the fabrication (step (i) in Figure 2- 7). It is mainly focused on assembling basic units into larger structures, like building a house brick by brick. For this, chemical synthesis and self-assembly processes are used to form, for example, thin films and quantum dots. A bottom-up approach based on chemical vapor deposition was used in this work to obtain polymeric thin films, which were the basis of the waveguides and part of the metamaterials stacking. Details about this method are discussed in the next chapter.

2.3 Polymeric Carbon Nitride (C_xN_y)

Understanding the structure of binary compounds of carbon and nitrogen is essential for the development of a broad range of applications in the field of micro-and nanotechnology, including photocatalysis, optics, and photonics. In recent years, various carbon nitride-based materials have been shown to be of increasing industrial and scientific importance due to their outstanding mechanical and electronic properties that are comparable to that of diamond and graphene[12,13]. However, no effective characterization has been made thus far to fully understand the reaction mechanism that leads nitrogen-rich precursors to condensate in a 2D carbon nitride structure; this has also not yet been experimentally proved, although widely referred to as g-C_3N_4. In the last decades, a very thermostable aromatic tri-s-triazine moiety has been extensively studied and discussed as the final condensation product of molecular precursors such as melamine[37], cyanamide[38], dicyanamide[39], and urea[40]. First synthesized by Berzelius in 1830, and later named "melon" by Liebig[41] in 1834, it was identified as the high-temperature

phase of carbon nitride, preceded by different triazine and heptazine(tri-s-triazine)-based intermediate compounds named "melam" and "melem" – each of the mentioned being related to different de-ammonation degrees, e.g., different degrees of polymerization (Figure 2- 8). Further thermal treatment of melon would theoretically result in a completely condensed product with linked heptazine units, more recently postulated as "graphitic carbon nitride" (g-C_3N_4) due to its structural similarity to graphite[12,42].

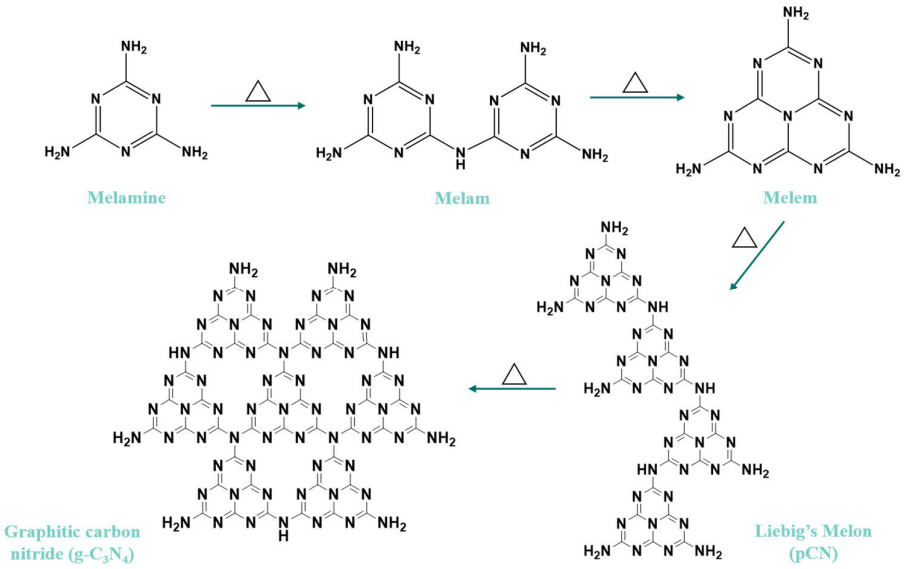

Figure 2- 8: Carbon nitride condensation cascade.

The so-called g-C_3N_4 is considered the most stable solid-state carbon nitride allotrope amongst the ones predicted theoretically by Liu and Cohen[43]: α-C_3N_4, β-C_3N_4, pseudocubic-C_3N_4, and cubic-C_3N_4. Henceforth, different attempts to obtain a material correspondent to g-C_3N_4 in terms of geometry and stoichiometry have already been made, but considerable content of hydrogen and defects within the polymer chain would invalidate the predicted structure, generating a high number of mistaken attributions. Although Liebig had already claimed that the composition of what he called "melon" – nowadays also named as polymeric carbon nitride (pCN) - was changing with different synthesis methods and equipment, recent studies are still referring to carbon nitride as the fully condensed pure g-C_3N_4 when obtaining melon related products with varying ratios of composition. Most postulated g-C_3N_4 structures have their triazine and heptazine ring systems linked through trigonal nitrogen, forming 2D sheets.

Regarding pCN, the 2D structure is formed by hydrogen bonds between the linear heptazine polymers with an offset, meaning they do not stack precisely at the same point above each other[44,45].

Carbon nitrides are widely reported as versatile wide-gap organic semiconductors, with bandgaps ranging from considerably low values to 2.8 eV. The possibility to tune the bandgap makes carbon nitride a promising polymeric photocatalyst for water splitting and pollutant degradation under UV radiation. Besides, bandgap engineering has a crucial role in the field of semiconductor optoelectronics[46–48]. Additionally, C_xN_y compounds are synthesized from nitrogen-rich organic compounds[41] widely produced on an industrial scale, making them a much more sustainable material than the inorganic counterparts currently used in optical systems. Most of the reports so far consider carbon nitride in its powder-based form, nonetheless, thin films have properties that differ from that of the bulk and are advantageous as optical coatings. In the next section, the properties of pCN thin films will be discussed in more depth.

2.3.1 C_xN_y thin films processing

Thin films optics is a broad subject permeating in different topics within optical devices. Most optical systems consist of optical surfaces with specific properties assured by a very thin optical coating layer ranging from tens to a few hundred nanometers. The coating is usually formed by one or more thin films of material with particular properties governed by composition, shape, and thickness, chosen to manipulate a desired range of electromagnetic waves. The properties of a thin film material substantially differ from the bulk properties due to the surface influence – the ratio between the surface and the volume is much larger in the thin film than in the bulk. The role of a thin film is to alter the reflection, transmission, and refraction of light concerning the behavior of the bare substrate and other layers[49,50].

Methods for synthesizing crystalline and amorphous carbon nitride thin films have already been reported using physical and chemical vapor depositions (PVD and CVD, respectively), including radio-frequency magnetron sputtering[51], microwave plasma CVD[52], pulsed laser

ablation (PLA) of graphite targets[53], and laser-induced CVD[54]. The majority of these works have resulted in rough and non-homogenous films[55]. On the other hand, thermal chemical vapor deposition using melamine powder as a precursor has shown to be a promising and easy way of fabricating carbon nitride thin films. It was firstly reported by Urakami et al.[56] in 2019, with a homebuilt hot-wall CVD system at atmospheric pressure (APCVD). The authors have grown high-quality thin films on different substrate surfaces by evaporating melamine at approximately 400ºC and condensing it on a substrate at 600ºC, under N_2 flow. The resultant films had a C/N ratio of 0.73, really close to the ideal value of 0.75, when considering the g-C_3N_4 structure. The system was optimized by Giusto et al.[13] in 2020 for a low-pressure chemical vapor deposition (LPCVD) system consisting of a furnace zone at 300ºC consigned to the sublimation of melamine and a second zone at 550ºC for the polymerization onto the substrate, also under N_2 atmosphere. C/N ratio was reported to be 0.71.

But what is chemical vapor deposition, and how does it work?

Shortened CVD, chemical vapor deposition is a versatile technique that enables the production of pure, uniform coatings of metals, polymers, and hybrid materials even when using contoured surfaces as a target. Moreover, it can be used for the fabrication of surface layers of varying phase composition and thicknesses. It is a modern basic manufacturing and engineering tool that is widely used in materials-processing technology, and is more frequently applied to nanostructured materials in applied optics and micro-and nanoelectronics.

Thin film growth by CVD is the result of a complex sequence of chemical reactions. The technology combines several scientific and engineering disciplines such as kinetics, fluid dynamics, thermodynamics, plasma physics, and chemistry. As a simple definition, the setup involves flowing a precursor gas (or gases) into a chamber containing one or more heated substrates to be coated. Various enhanced CVD processes setups are engineered and categorized according to the type of application, which can involve using hot or cold-wall reactors, with pressures ranging from below to above atmospheric, with or without reaction in the gas phase, and temperatures from 200ºC to exceeding 2000ºC. Different sources can provide the necessary energy for the reaction, as heat and photons, with thermal energy being the most common. Hence, thin film properties are highly dependent on the deposition process.

The basic concepts which dictate a CVD process are thermodynamics and kinetics. The first is responsible for indicating what to expect from the reactants as they reach the deposition surface at a given temperature. The second defines the transport process and determines how fast the reaction is going to happen. The sequence of steps taking place during the deposition is shown in Figure 2- 9.

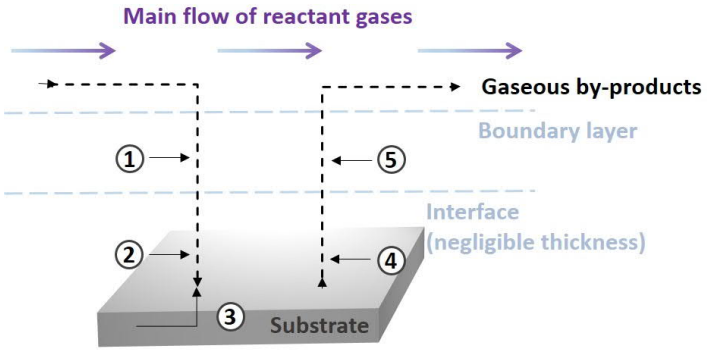

Figure 2- 9: Chemical vapor deposition (CVD) mechanism sequential steps.

First, the reactant gas enters the reactor by forced flow and diffuse through the boundary layer (1). As it passes over or comes into contact with a heated substrate, it is adsorbed by the substrate surface, initiating the condensation process with the formation of small clusters of material. Nucleation occurs when adsorbed atoms migrate on the substrate's surface, interacting with other atoms, until coalescence occurs, resulting in larger structures that lead to film formation (2). Under the right conditions, a surface chemical reaction takes place (3). It is followed by the desorption of volatile by-products and their disposal from the substrate (4) and, subsequently, their convective and diffuse transport away from the reaction zone (5)[57,58].

Inside the chamber reactor, the flow needs to be optimized so the thin film deposits uniformly onto the substrate with a maximum deposition rate. In most CVD reactors, the flow is in the viscous-dominated laminar regime. Within this regime, the molecules are slowed down near the substrate, creating a stagnant layer above it – the so-called boundary layer. An illustration of the general flow inside a tubular reactor is shown in Figure 2- 10.

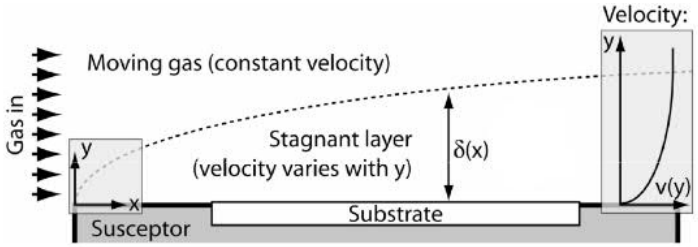

Figure 2- 10: Boundary layer velocity profile in the CVD reactor laminar flow.

The hydrodynamic boundary layer is defined, considering that, within these layers, velocity gradients and shear stresses exist, as described by Newton's law of fluid friction in Equation 2.22.

$$\tau = \eta \frac{\partial u}{\partial y} \tag{2.22}$$

Where τ is the shear stress, η is the fluid viscosity and $\frac{\partial u}{\partial y}$ the velocity gradient.

As the flow goes downstream, the slower moving fluid near the surface exerts frictional forces on the fluid that is further away, and each fluid layer gradually slows down the layer above it, increasing the boundary layer thickness with the distance from the substrate surface. A flow is never perfectly laminar throughout the flow stream, as there is always a certain degree of turbulence. Turbulent flows have a similar trend, with some differences in the velocity distribution. Suppose the disturbance in the turbulent region becomes unstable. In that case, the thickness of the boundary layer increases much more due to vortex formations, increasing the velocity gradient perpendicular to the stream[59]. In CVD processes, this lead to a vortex-shaped distribution of the thin films, with uneven thickness along the substrate surface.

The thickness of the boundary layer can be estimated by correlating it with the Reynolds number (*Re*) of the flow tube. For most CVD reactors, this number is around a few hundred, which still correspond to the laminar flow. The transition from laminar to turbulent flow occurs at $Re = 5\text{x}10^5$.

$$\frac{\delta}{x} = fn(Re_x) = \frac{4.92}{\sqrt{Re_x}} \quad (2.23)$$

With:

$$Re = \frac{\rho u x}{\eta} = \frac{\eta x}{\nu} \quad (2.24)$$

δ is the boundary layer thickness, and x is the distance from the leading edge where the transition occurs. ρ is the density, u is the velocity based on the tubular reactor's cross-section area, μ is the dynamic viscosity, and ν the kinematic viscosity[60].

Generally speaking, three basic growth modes exist for the formation of solid thin films under thermal equilibrium (Figure 2- 11): Frank-van der Merwe or layer-by-layer mode, Stranski-Krastanov or layer-plus-island mode, and Volmer Weber or island mode. The layer-by-layer growth (a) happens when the deposited material's atoms are more strongly attracted to the substrate than to each other, and the smallest stable nucleus occurs in 2D, resulting in planar sheets. This mode is commonly observed for semiconductor growth on other semiconductors. On the other hand, islands (c) are grown when the atoms or molecules in the deposited materials are more strongly bound to each other than to the substrate, and stable clusters nucleate directly on the substrate surface, growing into 3D islands of the condensed phase. This mode is valid for different systems of metals growing on insulators.

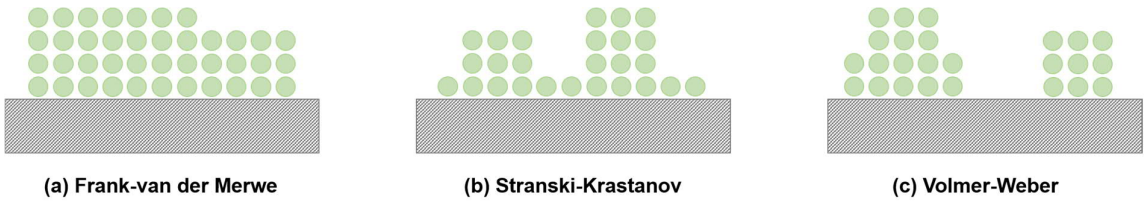

Figure 2- 11: Schematic representation of the three thin film growth modes: (a) layer-by-layer, or Frank-van der Merwe mode, (b) layer-plus-island, or Stranski-Krastanov mode, and c) island, or Volmer-Weber mode. Adapted from[61].

An intermediate of both modes mentioned above combines layers and islands during growth in a 2D (wetting) to 3D (dewetting) growth transition (b). It happens when, at some point, the subsequent growth of monolayers becomes unfavorable due to any change of parameters that

could induce defects, and the formation of islands takes place - mainly because the interface energy increases with the film thickness. This growth mode is typically observed for metal-metal, metal-semiconductor, gas-metal, and gas-layer systems. It is important to mention that the three growth processes involved in film fabrication were postulated for homogeneous nucleation, without considering any defects along the substrate surface. However, in practice, the growth process is not ideal, and heterogeneous nucleation occurs[61–63].

2.3.2 Optical properties of C_xN_y thin films

The study of C_xN_y compounds has attracted a lot of attention over the last two decades due to their remarkable optical and electronic properties. Several experiments have been performed on controlling the C/N ratio to increase or decrease the bandgap and achieve desired semiconducting functionalities. In semiconductors, the bandgap sets the maximum energy E_g (or minimum wavelength, λ_g) for which a material is transparent. As the wavelength approaches the bandgap wavelength, light moves slower, meaning n and k increase, and the material becomes less transparent (if n increases, transmission decreases)[64]. Thus, a correlation between E_g and refractive index has a significant influence on the band structure of semiconductors.

Although many studies have reported an easy tunability of gap and dispersion properties, they are quite inconsistent. In 1995, Wang et al.[65] showed that the refractive index and reflectance of carbon nitride thin films decreased as the nitrogen content increased, results also obtained later by Lu et al.[66] and Balaceanu et al.[67] On the other hand, in an article published in 2001, Broitman et al.[68] indicated an increase of n and bandgap with higher densification of the films. The authors reported that the void fraction (porosity) within the thin film decreased when having a higher nitrogen content. More recent ellipsometry investigations on C_xN_y thin films are in agreement with the latter description. Furthermore, the type of chemical bonds among the structure also dictates the properties of carbon nitride thin films. Different hybridization types can occur when carbon bonds with nitrogen, mainly forming sp^2 ('graphite-like'), sp^3 ('diamond-like'), and sp^1 bonds. It influences not only the hardness of the films (higher content on sp^2-bonded carbons means softer film and, sp^3-bonded carbons, harder) but also on

its optical properties[69]. According to Miyajima et al.[70], the lower the nitrogen concentration, the higher the probability of sp^3-hybridized carbons to be formed at high pressures. An increase in the sp^3 fraction gives the film more internal stress, creating localized states and larger π bonded clusters, decreasing the optical bandgap. Previous studies have also found that increasing the nitrogen content through different deposition methods favor the formation of low-density, sp^2-bonded carbon amorphous structures, with graphitized sp^2 sites primarily controlling the optical and electronic properties[71–74]. Still, it is important to note that regarding the influence of nitrogen content, different trends are observed according to the deposition system.

The optical bandgap of what is today considered "g-C_3N_4" has already been widely reported to range from 2.3 eV to 2.9 eV, referent to the absorption peak in the violet-blue part of the optical spectrum. The absorption edge in the visible, located between 400 nm and 450 nm, gives polymeric carbon nitride a yellowish color both in bulk and thin-film forms[48,67,75,76]. A red-shift in the absorption edge can be seen with subsequent polymerization due to loss of –NH_2 terminal groups and increased cross-linking, resulting in a brownish color. Further, photoluminescence (PL) studies have shown that when excited under UV at 365 nm, pCN thin films exhibit a bright blue emission around 463 nm. A decrease in PL intensity also causes a red-shift in the emission peak when polymerization temperature is increased[56,77]. Moreover, studies focused on the ellipsometry characterization of pCN films have revealed the highest refractive index within organic polymers[13]. The values of n and k at 630 nm in different studies range from 1.98 to 2.5 and from 0 to 0.2, respectively, varying according to the deposition method used, its parameters, and final C/N ratio. A trend in all the previous reports shows a significant increase in the refractive index of up to around 600 nm, followed by its gradual decrease over longer wavelengths, as described previously in the Cauchy Equation (2.20)[66–70,78,79].

High refractive indices at low wavelengths are due to the effect of the fundamental absorption of photons (electronic transitions) of carbon nitride films in the visible. Although many ellipsometry investigations have been done, none of them, to my knowledge, had considered the anisotropic nature of the 2D structure of pCN and its influence on the dispersion properties. A structural change in the out-of-plane direction can directly impact on the guiding properties

of the material. The anisotropy effect will be demonstrated later in this thesis.

Chapter 3

Thin film fabrication and characterization

One of the main goals of this work is to investigate the influence of chemical vapor deposition key parameters on the composition, structure, morphology, and optical dispersion properties of amorphous polymeric carbon nitride (pCN) thin films. The first part of this chapter is dedicated to the fabrication of the thin films through a chemical vapor deposition process, which had shown itself to be one of the most promising approaches to obtain high-quality films so far, as previously mentioned in Section 2.3.1 C_xN_y thin films processing

The second part is assigned to the characterization of the three sets of experiments: IP-x, t-x, and fw-x, which correspond to changing the amount of melamine, the polymerization time, and the gas carrier flow rate during the deposition process, respectively.

3.1 Fabrication

Amorphous polymeric carbon nitride thin films were grown using our in-house low-pressure chemical vapor deposition (LPCVD) system[13]. The setup consists of a two-zone furnace reactor that was specially designed for synthesizing 2D materials. As shown in Figure 3- 1, in the first zone (upstream), the chosen precursor, melamine ($C_3N_3H_6$), sublimates at 300°C, and it polymerizes on the substrates at the higher temperature (500°C) zone (downstream). The process was kept under a pressure of 10 Torr.

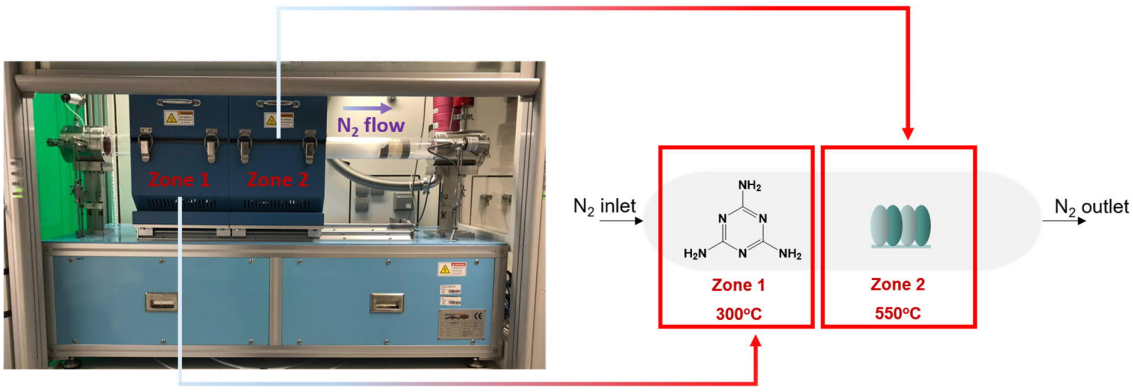

Figure 3- 1: CVD setup and scheme for the growth of pCN thin films on various substrates.

The precursor choice was made based on previous studies with the same or similar setup, which have shown the ease tunability of thickness and optical properties of pCN films. Melamine is a suitable nitrogen-rich solid compound that eliminates ammonia and undergoes condensation through a thermal polymerization process. Additionally, it sublimates at considerably low temperatures (≈ 300°C)[13,56]. During the deamination process of the melamine powder, an intermediate product called melem ($C_6N_{10}H_6$), considered the low-temperature phase of CN, is formed. Further polymerization of melem onto the high-temperature substrate is what leads to the formation of 2D carbon nitride sheets (high-temperature phase). However, for the efficient growth of low-roughness and homogeneous films, some basic requirements and aspects need to be considered when using a CVD system.

The substrate temperature influences the synthesis of the 2D structure due to the

polymerization degree of the s-triazine derivatives, melem, and melon. A different substrate temperature would lead to a different polymerization degree and, consequently, to a different structure of the s-triazine based film. The tri-s-triazines arrangements are known to be formed at around 390-400 ºC. Between 520-550 ºC, more ammonia is released, and the condensation into the polymer network occurs. Above 600 ºC, melamine condensates undergo extensive thermal degradation[42,45,80]. According to the results previously obtained for our in-house system, we have maintained the upstream and downstream furnaces at 300ºC and 550 ºC, respectively.

Another parameter to be considered is the nitrogen flow. Herein, N_2 was used only as a gas carrier, meaning it should not incorporate into the thin films. Some experiments using different N_2 flow rates (25, 50, and 100 SCCM) were performed to see how it would affect the C/N ratio, structure, thickness, and optical properties of the thin films. Additional experiments were also performed by varying the amount of precursor and reaction time. No systematic study has been reported so far to quantitatively and qualitatively access the effect of CVD operation conditions on morphological, structural, and optical dispersion parameters of pCN.

3.2 Systematic investigation of the deposition parameters

In this section, I will show the results obtained for each variable case, using standard ellipsometry, environmental ellipsometry porosimetry (EPP), IR ellipsometry, x-ray photoelectron spectroscopy (XPS), scanning electron microscopy (SEM), energy dispersive x-ray spectroscopy (EDX), high-resolution transmission electron microscopy (HRTEM), thin-films x-ray diffraction (XRD), atomic force microscopy (AFM), UV-VIS-NIR transmittance spectroscopy, and nanoindentation measurements. Except for the transmittance spectroscopy, all the mentioned experiments were performed on pCN thin films deposited on a Si wafer with a 2 nm native oxide layer. The UV-VIS-NIR measurements were carried out on thin films deposited on SiO_2 substrates.

3.2.1 Influence of precursor amount

Operating conditions of CVD processes are known to influence various properties of the deposited thin films. The first intent of this work was to develop thicker thin films using the same setup described previously by our group[13]. Due to further applications on optical devices such as strip waveguides, the thickness of the pCN thin films must not be thinner than 200 nm to be effectively used for light guiding in the visible range. For telecom wavelengths, a minimum thickness of around 300-400 nm is necessary. Those values are essential to preserve a single-mode operation waveguide whilst keeping low propagation losses through leaking. This concept will be further explored in the chapter dedicated to the nanofabrication of waveguides.

The experiments consisted of using the same CVD process recipe for three different precursor amounts: 10g, 15g, and 20g. Each step of the deposition process is shown in Table 1.

Table 1: CVD parameters for investigation on the influence of precursor amount. (x) = 10, 15 and 20g.

pCN (x)g	Step 1	Step 2	Step 3	Step 4	Step 5	Step 6
Upstream (ºC)	0	0	300	300	0	0
Downstream (ºC)	0	550	550	550	550	0
Heater time (min)	10	40	30	30	30	2
N_2 gas set (SCCM)	500	50	50	50	50	0
Pressure set (Torr)	10	10	10	10	10	10

The process goes as follows: first, the pressure is stabilized at 10 Torr, and a nitrogen flow of 500 SCCM is flushed into the quartz reactor tube for 10 minutes to clean any eventual contaminants that may be present (Step 1). Next, the downstream furnace starts heating up to 550 ºC, so the substrates are already hot enough to polymerize the intermediate products on their surface (Step 2). During Step 3, the upstream furnace is heated up at 10 ºC/min, and melamine starts to sublimate after 30 minutes. The carrier gas transports the intermediate products onto the substrate's surface for further polymerization until Step 4. After complete sublimation of the precursor, the downstream furnace is kept on 550 ºC for further condensation and annealing of the 2D structure (Step 5). As the last stage, the carrier gas is ceased, and both

furnaces cool down to room temperature still under vacuum (Step 6). The samples are then removed from the reactor and stored for further characterizations.

3.2.1.1 Spectroscopic Ellipsometry – dispersion parameters and molecular orientation

Knowing the dispersion parameters of polymeric organic thin films is essential for modeling and optimizing optical devices. Most optical systems designs, especially those presented later in this thesis, are based on experimental complex refractive index values. One of the best methods to investigate the optical properties of thin films is spectroscopic ellipsometry[81]. Ellipsometry studies can help to explore not only the dispersion parameters of the pCN thin films but also give some insights into their molecular packing and orientation. Briefly, thin films can be divided into three regions: air/film, film/film, and film/substrate interfaces. The molecules are oriented differently at specific interfaces of 2D materials depending on how the inversion symmetry is broken in between layers. This change in orientation has a strong impact on the light propagation and the electrical properties of thin films[82].

The influence of the anisotropic alignment and orientation of organic molecules on the optical properties of vacuum-deposited thin films was first reported by Lin et al.[83]. The authors investigated both real and imaginary refractive index parts of vacuum-deposited ter(9,9-diarylfluorene) films using variable angle spectroscopic ellipsometry. The ellipsometry results revealed a large uniaxial anisotropy, i.e., a large difference between the extinction coefficients in the in-plane (parallel to the surface) and out-of-plane (normal do the surface). The in-plane extinction coefficient was much larger than the out-of-plane, inferring that the molecules of the studied thin films tend to align their π-π^* transition dipole moments and molecular axes in the direction parallel to the substrate surface. The same result was also achieved in other previous studies for different organic conjugated polymers deposited under different conditions[84–87]. Although some studies have already reported the optical properties of pCN thin films through ellipsometry measurements, none of them has considered the anisotropic orientation of the molecules either caused by a change in orientation in-between transition layers or impurities.

Spectroscopic ellipsometry is a reflection technique that allows us to perform contact-free non-destructive studies of thin films. It detects the phase change in polarized light as it reflects light off of a surface or transmits through it. It does not directly measure the thickness and optical constants but rather uses collected data to solve models that estimate the thickness and dispersion parameters of interest[88]. In this work, the dielectric function of carbon nitride thin films deposited under different key parameters was derived from the data analysis of spectroscopic ellipsometry measurements with a J.A. Woollam M-2000U ellipsometer at multiple incidence angles in steps of 5° throughout the spectral region from 245 to 1000 nm. The optical response of the investigated samples was simulated by building a suitable optical model with Gen-Osc (General Oscillator) functions for the absorbing part of the spectra and Cauchy for the transparent one. The Gen-Osc layer uses a summation of standard oscillator lineshapes, and, in our case, Tauc-Lorentz oscillators were employed. Details about the fundamentals of the dispersion models can be found in Section 2.1.4 Dispersion models in dielectrics

For defined reflectance measurements, the incidence angle was set around the Brewster angle of the silicon substrate, ranging from 60° to 75°, so that it was possible to avoid getting signals from the substrate and optimize the reflection from only the surface. The Brewster angle is the angle of incidence at which there is no reflection of light with a particular polarization, and thus the light is perfectly transmitted. The probe spots resulted from the chosen incident angles are much smaller than the sample size. On the basis of the aforementioned previous studies on conjugated polymers, the molecules on the amorphous pCN films were expected to be horizontally oriented, with some degree of anisotropy perpendicular to the substrate plane. Therefore, after applying Cauchy and Gen-Osc, the layer was set to have uniaxial anisotropic optical properties.

A layer with anisotropic optical constants has the index normal to the surface (extraordinary) different from the index in the surface sample plane (ordinary). This difference is common with many polymer films that orient along a specific direction. Two Tauc-Lorentz oscillators were applied to the in-plane direction, and one to the out-of-plane – details about the oscillator parameters are described in the Appendix (Figures A-1, A-2, and A-3). The parameters were optimized until reaching the ‘best fit’ by minimizing the mean squared error (MSE), which

considers the difference in the experimental and model generated data and weighs it with respect to the standard deviations at each wavelength. Nevertheless, the model function system satisfies the K-K consistency. The dispersion results are shown in Figure 3- 2. The color difference between samples presented in Figure 3- 2(d) are due to the constructive and destructive interferences between light waves reflected from the top and bottom layers of the thin films, and it is dependent on the thin film thickness and angle of the incident light.

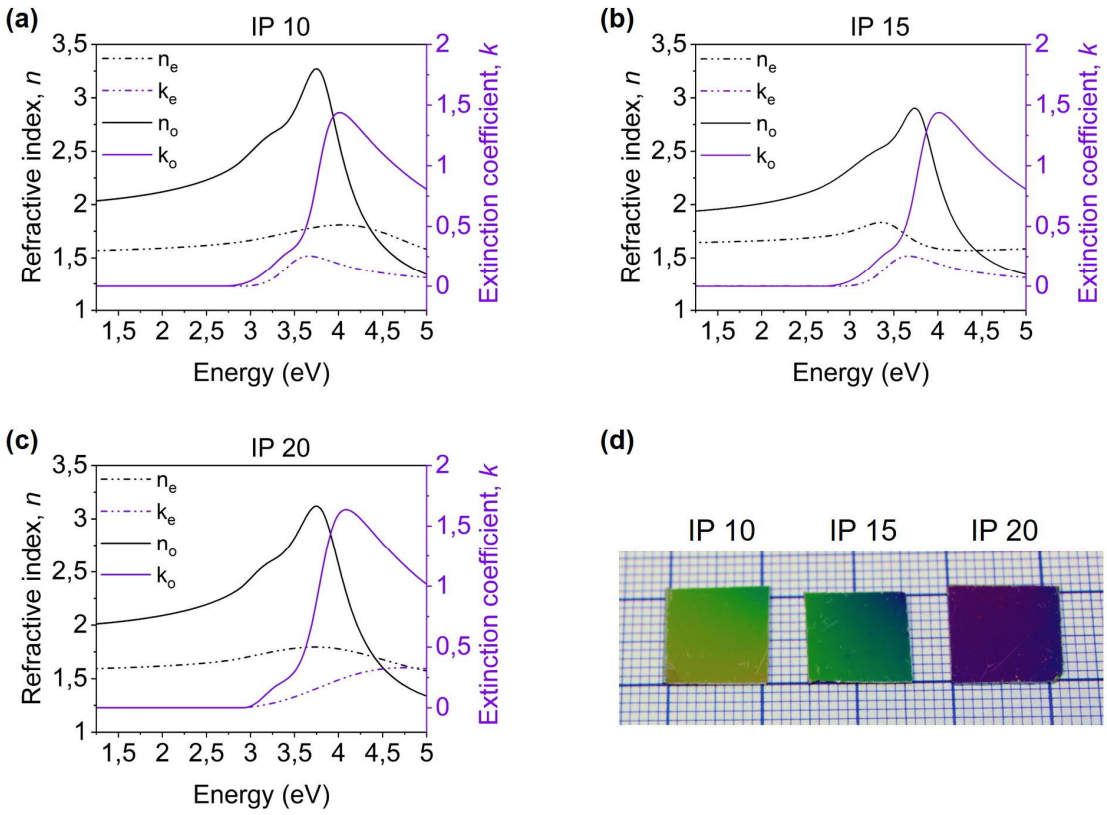

Figure 3- 2: Influence of precursor amount on dispersion parameters in the in-plane (n_o, k_o) and out-of-plane (n_e, k_e) using (a) 10g of melamine - IP 10, (b) 15g of melamine - IP 15, and (c) 20g of melamine - IP 20 deposited on a silicon wafer. (d) Picture of the correspondent samples, from left to right: IP 10, IP 15, and IP 20.

The values of k at the peaks in the absorption spectra of the films correspond to the maximum amount of excitation energy absorbed by the in-plane and out-of-plane dipoles present in the thin film. As the transition dipole moment for the lowest energy optical transition in conjugated polymers is nearly parallel to the polymer backbone, the peak values of k_o (solid lines) and k_e (dashed lines) indicate the average orientation of the polymer chains within the film. The non-

zero values of k_e revealed that some parts of the supramolecular crosslinked polymer chains are oriented perpendicular to the substrate plane, meaning π stacking is also present in the direction perpendicular to the substrate surface.

Furthermore, the anisotropy of optical parameters resulting from the polymer backbone lying preferentially in-plane (higher k) means there is a significantly higher polarizability along the polymer chain rather than perpendicular to it, and it is in agreement with the literature[82,83]. As shown in the spectra in Figure 3- 2, there are some variations in the dispersion parameters both in the in-plane and out-of-plane when changing the amount of precursor from 10g(a) to 15g(b) and 20g(c). Since those variations are not changing linearly with the thickness, as presented in Table 2 and obtained from the same function model, we can assume that the large differences in anisotropy from sample to sample (different tendencies for n_e and k_e curves) indicate a change in composition and stacking structure of pCN thin films. A variation of the C/N ratio would result in a different bonding structure and, therefore, in changes in optical anisotropy – this phenomenon will be explored later using IR ellipsometry.

At 630 nm wavelength, the pCN thin film is already transparent and has a continuous refractive index throughout the whole visible range. That is why the refractive index results described in Figure 3- 2 are attributed to this wavelength. The ordinary values of the RI (n_o) are in accordance with the literature and the previous statements that polymeric carbon nitride has the highest refractive index among organic polymers for the same wavelength range[13,65,66]. However, no one has ever considered the refractive index perpendicular to the sample surface for pCN. The sample with 10g of melamine has the maxima extinction coefficient at 4 eV, with k_o equal to 1.73 and k_e to 0.18. When using 15g and 20g of melamine, a maxima extinction coefficient at 4 eV was also achieved. The values for k_e and k_o are 1.44 and 0.19 for 15g, and 1.6 and 0.23 for 20g, respectively.

Table 2: Influence of precursor amount on the thickness and refractive index (n_o and n_e) at 630 nm wavelength and extinction coefficients (k_o and k_e) at 309 nm.

Sample	Thickness (nm)	n_o @630 nm (1.97 eV)	n_e @630 nm (1.97 eV)	k_o @309 nm (4 eV)	k_e @309 nm (4 eV)
IP 10	236.61	2.11	1.59	1.73	0.18
IP 15	263.10	2	1.66	1.44	0.19
IP 20	195.31	2.08	1.62	1.6	0.23

In the case of pCN films, it is notable from the spectra obtained by ellipsometry that the optical constants are changing with thickness, and not linearly. That makes the model fitting a bit tricky. A unique fit could only be achieved by applying multiple sample analysis and fitting several samples of identical constants but with different thicknesses together. And then, after that, all the optical constants are coupled. In our case, that was not possible precisely due to a large number of variations in the optical constants and fit parameters when changing samples. As a result, all the samples were analyzed in separated model functions.

Moreover, the thickness of the pCN samples increased from 10g to 15g, but when using 20g, the thickness decreased. Why? When using CVD under unoptimized conditions, thermodynamics and kinetics play a role in limiting the gas-phase transport and the surface reaction. In a CVD process, parameters such as pressure, process time, and gas carrier flux are set to control the reactor's growth rate and determine the maximum mass supported by the particular reactor system under specific conditions. All those parameters were first optimized for 10g of precursor, and when increasing it to 20g, the maximal support of mass in the system, which is constrained by external settings, was extrapolated. It means that, when increasing the precursor amount, the deposition rate also increases until a certain point (Figure 3- 3), as it did happen with the 15g sample. However, when extrapolating this point, there are higher reactant amounts inside the reactor tube per volume unit than the set parameters can support, and gas-phase nucleation occurs, slowing down the deposition. That is something that should be avoided in a deposition process because it causes not only local depletion of the reactant, resulting in a non-homogenous thickness, but also can incorporate particles within the thin film[89,90].

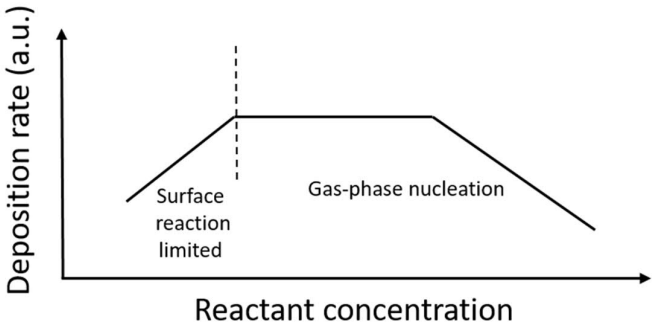

Figure 3- 3: Influence of reactant concentration on the deposition rate of a CVD process. Adapted from[90].

3.2.1.2 pCN thin film composition and structure

In order to further investigate the polymerization mechanism and understand the resulting carbon nitride composition, XPS experiments of each sample were performed. Bertram Schulze Lammers, from the Nanoscale Interface Analytics group at the University of Münster, was responsible for conducting the XPS measurements. He also helped with interpreting the results.

With XPS analysis, it is possible to investigate the bonding states of the pCN thin films, albeit it is only a surface measurement, meaning it does not go deep into the sample structure. Figure 3- 4 shows the XPS spectra for the thin films deposited with the three different melamine amounts. To investigate the chemical bonding of C and N atoms in the films, C1s and N1s core level spectra were recorded.

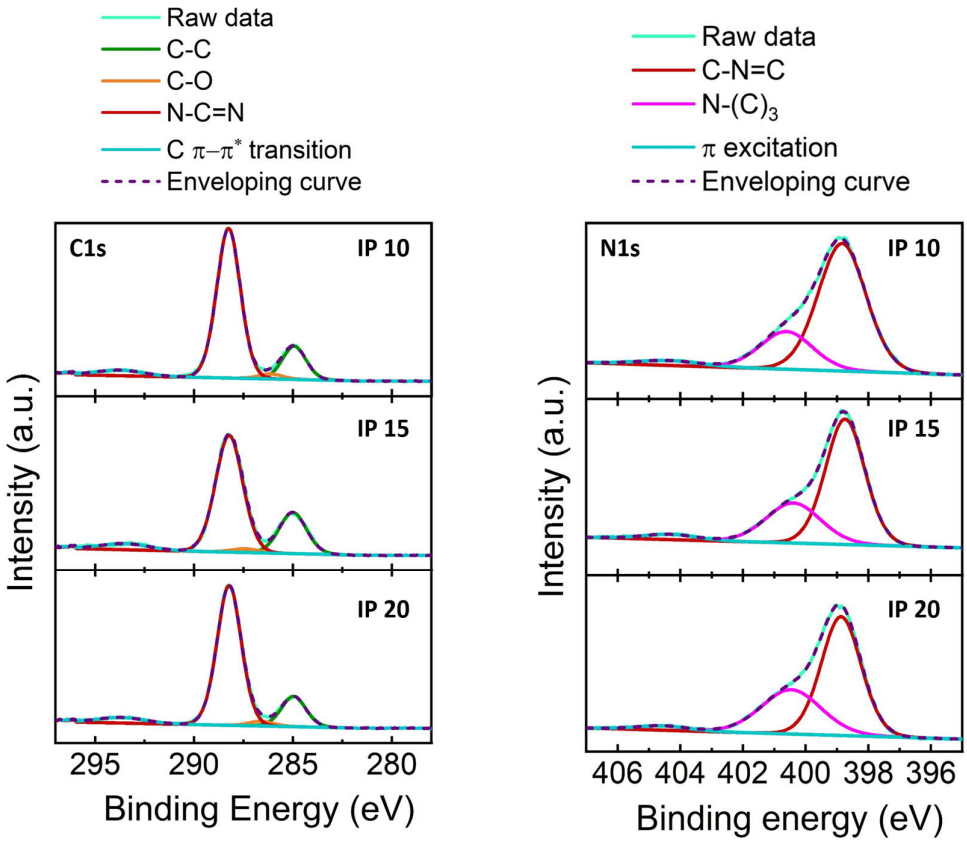

Figure 3- 4: XPS C1s and N1s spectra of samples IP 10, IP 15, and IP 20.

The deconvolution of the C1s spectra revealed peaks at around 285 eV for all the samples. In general, peaks in the range of 283.5-285 eV are attributed to C-C hydrocarbon bonds, often present on air-exposed samples, which is our case. Those are contaminations adsorbed on the film surface. The percentage of those adventitious carbon is different from sample to sample, 17%, 24%, and 21% for samples IP 10, IP 15, and IP 20, respectively[91,92]. This difference is mainly due to the time each sample was exposed to air since they were not kept under an inert atmosphere and not synthesized on the same day. The compositions and bonding states extracted from the XPS spectra are described in Table 3 for better comparison.

Table 3: Bonding types and composition as determined by the XPS spectra (C1s and N1s) for pCN samples deposited with different melamine amounts (IP 10, IP 15, and IP 20).

pCN (x)g	N-C=N (C1s)	C-N=C (N1s)	$N-(C)_3$ (N1s)	C/N
IP 10	43%	37%	20%	0.75
IP 15	42%	40%	18%	0.72
IP 20	41%	44%	14%	0.71

Peaks at 288.26, 288.23, and 288.30 eV were also revealed from IP 10, IP 15, and IP 20, respectively, and correspond to the sp^2 carbon of the heptazine rings (N-C=N)[13,91,92]. The small orange peak at 287 eV may have arisen due to the oxidation of carbon atoms on the surface when the sample was exposed to air (it follows the same trend of contamination as for C-C bonds when comparing samples)[91]. The weak signal at 294 eV is assigned to the C π-π^* transition[56].

The bonding states extracted from the N1s spectra have shown two prominent peaks with a slight shifting between samples. The most dominant one at the lower binding (398.81, 398.75, and 398.84 eV for 10g, 15g, and 20g of melamine, respectively) is attributed to pyridinic nitrogen bonded to two carbons (C-N=C), while the peak at higher binding energy (400.36, 400.37, and 400.61 eV) appears due to sp3 bonded $N-(C)_3$[54,56]. A possible explanation for the broadening of this peak within different samples is the presence of a variety of hydrogen bonding motifs. Hydrogen bonding motifs shift the peak with different strengths, causing many peaks to overlap at a similar position and resulting in what we interpret as broadening. This hypothesis could be better understood later in this thesis when the different types of hydrogen-bonding patterns, possibly coexisting in the pCN thin films, are demonstrated in Chapter 4. Furthermore, weak signals at 404 eV have already been attributed in the literature as charging effects or positive charge localization in heterocycles due to π excitations[56].

In addition, the carbon to nitrogen ratio of each sample was calculated from the percentages of the different bonding states obtained in the XPS spectra. The sample IP 10 had a C/N ratio of 0.75, which is the same as the theoretically predicted value for a perfectly condensed graphitic

structure. Samples IP 15 and IP 20 had a C/N ratio of 0.72 and 0.71, respectively, due to the decrease of the N-C=N bonds with the increase of precursor amount.

When comparing the XPS results with the ellipsometry ones reported in the previous section, one can observe that the sample with the lowest content of C-N=C bonds and the highest content of N-$(C)_3$ bonds was the one with the highest refractive (@630 nm) and the highest extinction coefficient (@309 nm) both parallel to the substrate surface (IP 10). In comparison, the sample with the highest percentage of C-N=C bonds and lowest for the N-$(C)_3$ had the highest extinction coefficient (IP 20) in the out-of-plane. One possible explanation for this trend is that having more sp^2 nitrogen bonding to 3 carbon atoms could enhance the polymer conjugation, resulting in higher absorption[93].

The three samples were investigated using infrared (IR) spectroscopy ellipsometry from 500 cm^{-1} (20 µm) to 5000 cm^{-1} (2 µm) and incidence angles of 65°, 70°, and 75°. As with standard VIS ellipsometry, IR ellipsometry is typically used to determine optical constants and structural properties of thin films and layered systems. The bands and amplitude shapes obtained in IR ellipsometric spectra are directly related to the transition dipole moments of specific molecular vibrations of the material, enabling its fingerprint scanning[94–96]. In the IR ellipsometry spectra, the extinction coefficient *(k)* values correspond to a volume unit of matter and do not depend on the film thickness. As we have seen in the previous ellipsometry results, the optical parameters change more according to the structure than to the thickness. The results for the IR spectra are shown in Figure 3- 5. Compared to conventional FTIR results, the well-resolved vibrational bands are due to the removal of any interferential effects from the electromagnetic wave when using an IR ellipsometry system. As already presented in the literature for bulk carbon nitrides, the spectra show a sharp band at 810 cm^{-1}, assigned to an out-of-plane bending vibration of triazine and heptazine ring systems[45,97]. The low-energy bands at 1252 cm^{-1} and 1322 cm^{-1} are assigned to the C-N stretching vibrations, while the bands at 1421 cm^{-1} and 1558 cm^{-1} are related to the C=N stretchings belonging to triazine modes. The relatively weak signal at higher energies in the stretching region from 3000 cm^{-1} to 3400 cm^{-1} proves the presence of NH and/or NH_2 groups in the pCN thin films structure[45,98].

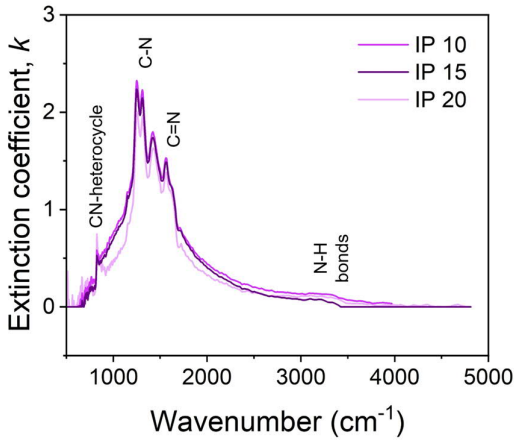

Figure 3- 5: IR ellipsometry spectroscopy spectra of samples IP 10, IP 15, and IP 20.

The intensity and broadness of the IR bands do not change between the samples according to the thickness but according to the amount of specific bonding patterns within the films, as already expected. The results follow the same trend as seen for the XPS spectra.

Scanning electron microscopy (SEM) and energy dispersive x-ray (EDX) spectroscopy were also performed to provide further insights into the structure and composition of the samples. As shown in Figure 3- 6, a thin film is homogeneously deposited on the substrate (there is a cut on the substrate that shows the edges of the pCN thin films) for all the samples. EDX elemental mapping (Figure 3- 7) confirms this observation. Also, it shows that carbon and nitrogen are homogeneously distributed throughout the samples.

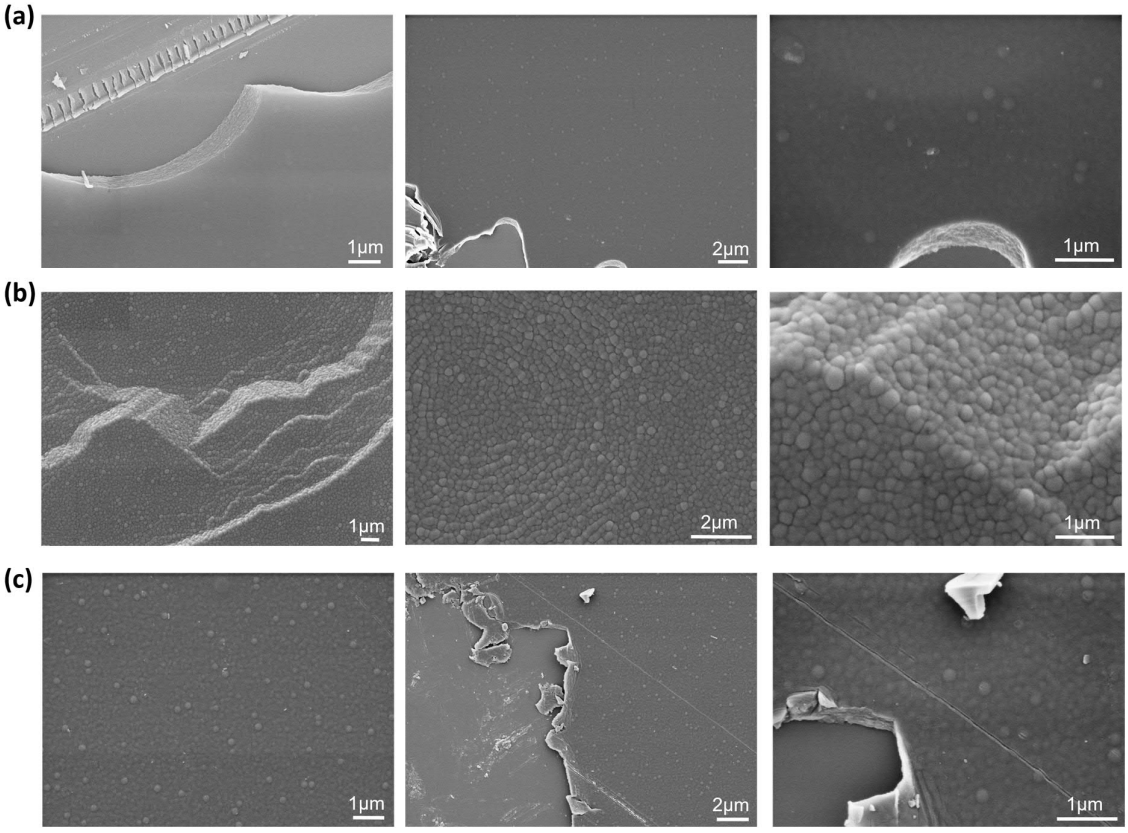

Figure 3- 6: SEM images of samples a) IP 10 (from left to right: 10 kx/10 kV, 5 kx/3 kV, and 20 kx/3 kV), b) IP 15 (from left to right: 5 kx/3 kV, 10 kx/3 kV, and 20 kx/3 kV, and c) IP 20 deposited (from left to right: 10 kx/3 kV, 5 kx/3 kV, and 20 kx/3 Kv) on a silicon substrate.

From the scratches in Figure 3- 6, it is possible to see that the films are composed of layers with different thicknesses. Moreover, samples IP 10 and IP 20 have a much more condensed and smoother surface than sample IP 15. The latter, which was previously mentioned as a product of the highest deposition rate between this set of samples, shows more grain domains of different sizes and isolated nucleation points. One critical step for the fundamental understanding of how the thin films are grown is the condensation of the material onto the substrate on a molecular scale, since the earliest molecules to condense on the substrate soon after exposure to the incident vapor strongly define the growth of the whole film structure. Further analyses on the morphological properties of the pCN thin films were conducted using atomic force microscopy (AFM) and are described later in this section.

The isolated bigger grains of similar diameter on the thin films' surface may have appeared because the reaction was carried out using a hot-wall CVD system. When using this kind of CVD reactor, the walls of the quartz tube and the substrates have the same temperature. This temperature distribution could lead to the film growth also on the inner surface of the tube walls in addition to the substrate deposition, resulting in secondary reactions and contamination. Another drawback from the hot-wall reactor, is that some particles are subject to fall from the top part of the tube to the substrate or film surface and form defects. Hence, the bigger particles seen in the SEM pictures could possibly be a result of a downfall of partially reacted particles from the inner wall or less condensed particles due to a limited polymerization time[61]. Additional SEM images can be found in the Appendix (Figure A-4).

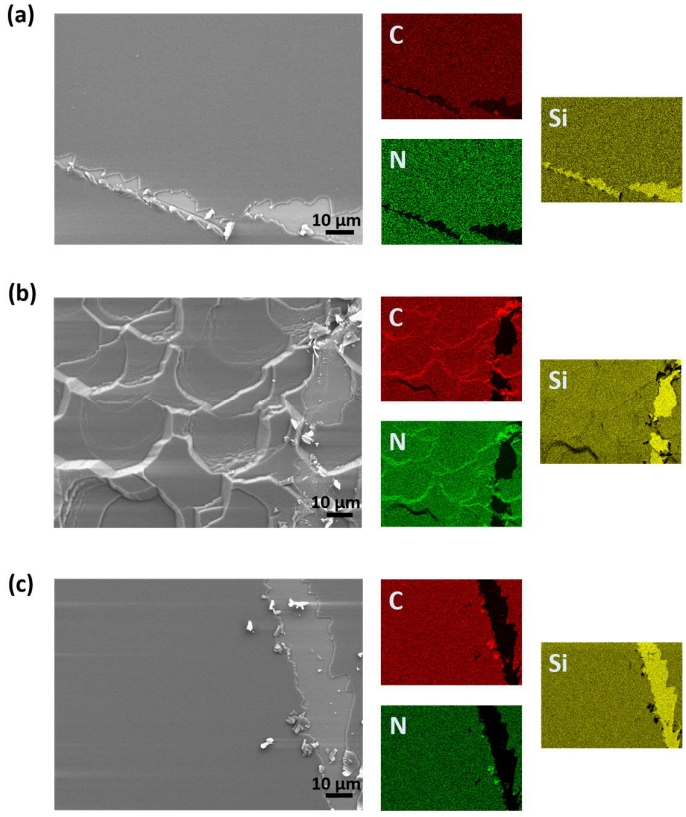

Figure 3- 7: SEM images and respective EDX elemental mapping of samples a) IP 10, b) IP 15 and c) IP 20 for carbon (red), nitrogen (green) and silicon (yellow).

The SEM images also reveal that the films are crack-free with a tightly packed grain structure. The grains have an overall size of about 100-200 nm. However, thin film x-ray diffraction (XRD) measurements (Figure 3- 8) have shown that all the samples have the pattern of an amorphous structure with a short-range order observed from a broad reflection centered at 27°, typically reported for carbonaceous graphite-like materials (commonly indexed as (002)). The reflection at this position corresponds to a 0.33 nm interlayer stacking[80].

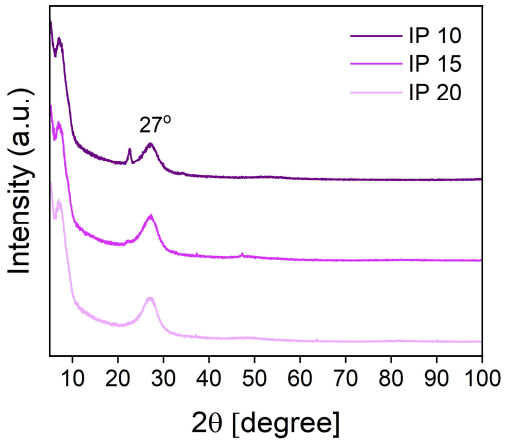

Figure 3- 8: Thin film XRD patterns of samples IP 10, IP 15, and IP 20.

A decreasing signal was also observed in XRD when comparing the pCN samples. It could either mean that the stacking height becomes shorter or that the disorder becomes higher, the latter meaning that the polymer chains preferred orientation decreases. The reflection at 7° is most probably an artifact. In short, in our XRD measurements, only basal *(00l)* reflections appeared. In addition, an XRD data fitting revealed that the samples are composed of small stacks, with more and less 2-4 layers by stack and a considerably high deviation of the stack sizes and the number of layers. The results indicate that the samples do not have layers with long-range order, which would explain the high optical anisotropy in the out-of-plane obtained with the ellipsometry measurements.

New SEM images were taken using a different detector. The images presented previously were all scanned with the conventional secondary electron detector (also known as SE2 or Everhart-Thornley detector). However, to get a better insight into the prominent grains of sample IP 15, the in-lens detector was used. The in-lens detector is able to collect the secondary electrons with higher efficiency, i.e., it is more sensitive to lower-energy secondary electrons, making it easier to get images with high contrast. As a result, the differences within the material are more pronounced, and the topographic information is more explicit, as shown below in Figure 3- 9. In the first image, the film is folded, being the surface at the top of the image brighter than the one at the bottom. It can be seen that the thin film shows a well-defined round granular shape with different sizes. The larger grain size can be attributed to a higher nucleation process due to changes in surface mobility/diffusion, which results in the overgrowth of neighboring grains.

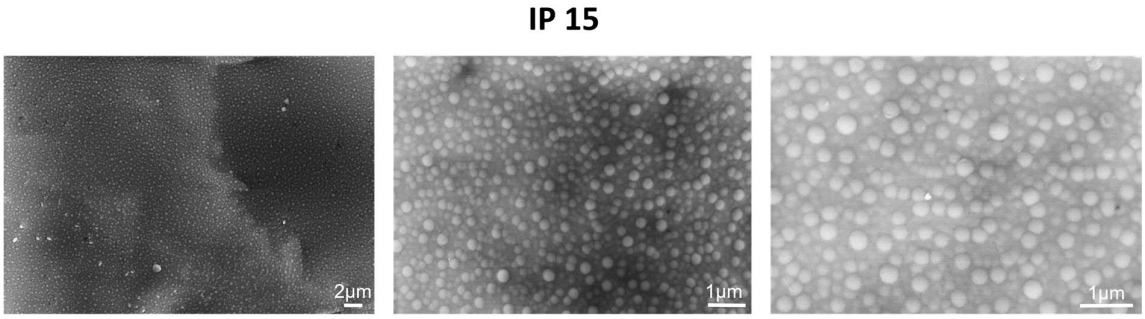

Figure 3- 9: SEM images of sample IP 15 deposited on a silicon substrate. The images were taken with the in-lens detector at different magnifications (from left to right 2.66 kx, 10.96 kx, and 17.5 kx) and electron high tension (EHT) of 5 kV.

In Figure 3- 10 it is possible to see the morphology of each round-shaped grain. Some of those grains have a scratch on their surface, revealing a core-shell-like structure. The difference in contrast between the outer surface of the spheroids and the inside content indicates that their core and shell have different compositions.

Any chemical vapor deposition process naturally exhibits a phenomenon called *shadowing*. During the deposition, uneven surface features are formed thermodynamically due to the vapor's directionality striking on the substrate surface, i.e., the obliquely incident atoms are preferentially deposited on higher spots or “hills” on the surface, leading to a long-range geometrical effect. The patterns seen in the SEM pictures can be attributed to this effect.

Additionally, the atoms do not arrive at the surface simultaneously, also contributing to a non-uniform deposition across the surface. This process results in a higher roughness during the thin film growth. On the other hand, another phenomenon occurs at the same time to counteract the randomness of the deposition and smooth the surface. Called the *re-emission effect,* it happens when the atoms do not stick on the "hills" but instead are knocked off and redeposited in a lower area. Both of the processes dominate over local effects as surface diffusion[99–101].

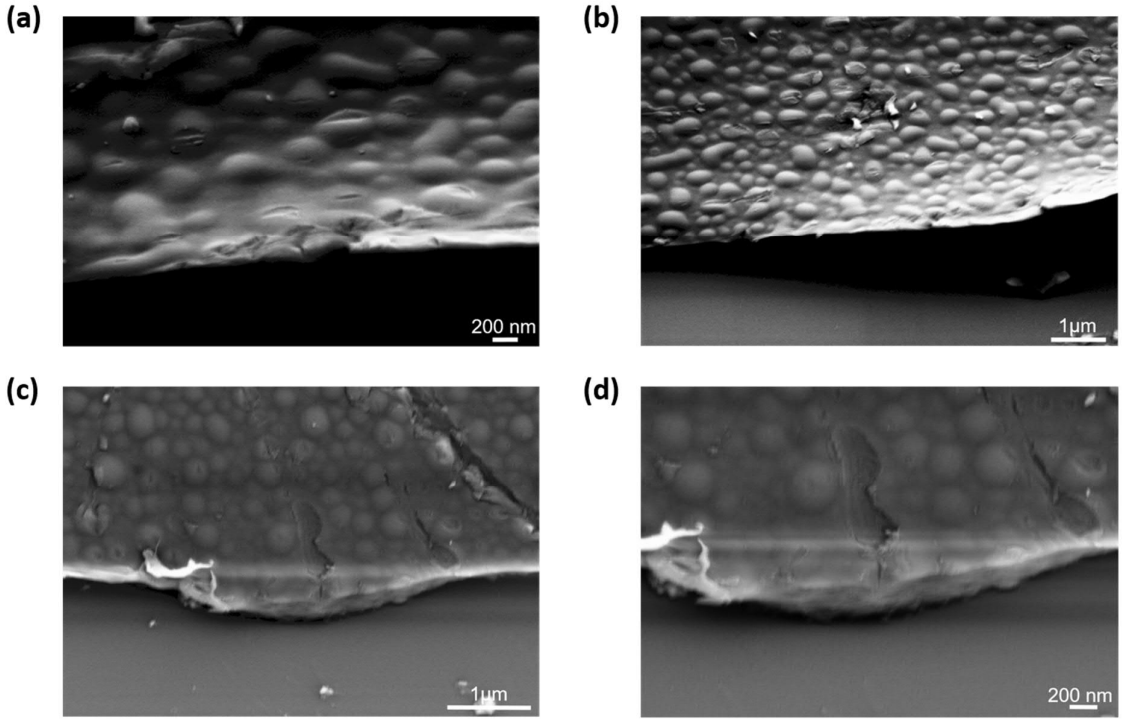

Figure 3- 10: SEM images of the core-shell spheroids from sample IP 15 deposited on a silicon substrate. a) 32 kx/ 4 kV, b) 13 kx/ 4 kV, c) 20 kx/ 4 kV, and d) 32 kx/ 4 kV.

High-resolution transmission electron microscopy (HRTEM) analysis of the sample IP 15, prepared with a microtome cross-section cut of the free-standing thin film, has shown the amorphous nature of the polymeric carbon nitride thin film (Appendix, Figure A-5).

The morphology of the pCN thin films was further analyzed by atomic force microscopy (AFM) using a Bruker JPK NanoWizard system with standard Arrow-NCR probe tips (<10 nm diameter), typical force constant of 42 N/m, and resonance frequency of 285 kHz. The experiments were carried out under AC-mode (tapping mode). Additionally, the images had a

pixel size of 512x512 and were taken within a 05-08 Hz LineRate range. All the images were flattened and processed using the JPK SPM data process software.

Analyses of nanoindentation measurements experiments on the thin films have revealed an elastic modulus (also referred to as Young's Modulus) of 18.2 ± 3.9 GPa, 15.4 ± 1.4 GPa, and 20.5 ± 2.9 GPa for samples IP 10, IP 15, and IP 20, respectively. It shows that the elastic moduli may depend on the thickness and are in the same range as other carbon nitride thin films already presented in the literature and previously by our group[13,102]. Moreover, the thinnest sample had the highest elastic modulus. The correspondent measurements were carried out with a penetration depth of 20 nm and can be found in the Appendix (Tables A1, A-2, and A-3).

Figure 3- 11 shows AFM amplitude and topography (*z* height) images (2 µm x 2 µm) for samples IP 10 (a), IP 15 (b) and IP 20 (c). Only sample IP 10 was evaluated with an additional 500 nm x 500 nm image due to the high similarity between the three of them. It can be seen that the films are crack-free and exhibit tightly packed small grains in spherical domains, as previously seen in the SEM images for a similar sized-area. The grains are mostly uniform in size, roughly 100 nm, with a few bigger grains distributed on the surface with sizes in the 200 nm range. The root mean square (RMS) roughness of the samples was extracted from the height counts of 2 µm x 2 µm images and is equal to 2.174 nm, 6.735 nm, and 3.933 for samples IP 10, IP 15, and IP 20, respectively. As mentioned previously, the thin film morphology depends on how the film growth process occurs, considering the deposition parameters and substrate. The roughness is a side effect of the layer growth. In amorphous thin films, there will be a preferential growth that follows the dominant grain orientation and islands formed after the nucleation process. This process is related to the *shadowing* and *re-emission effect* mentioned previously. Thus, having this preferential growth could lead to an increase of the surface roughness with increasing the thickness, also resulting in a change in the topography of the film[61].

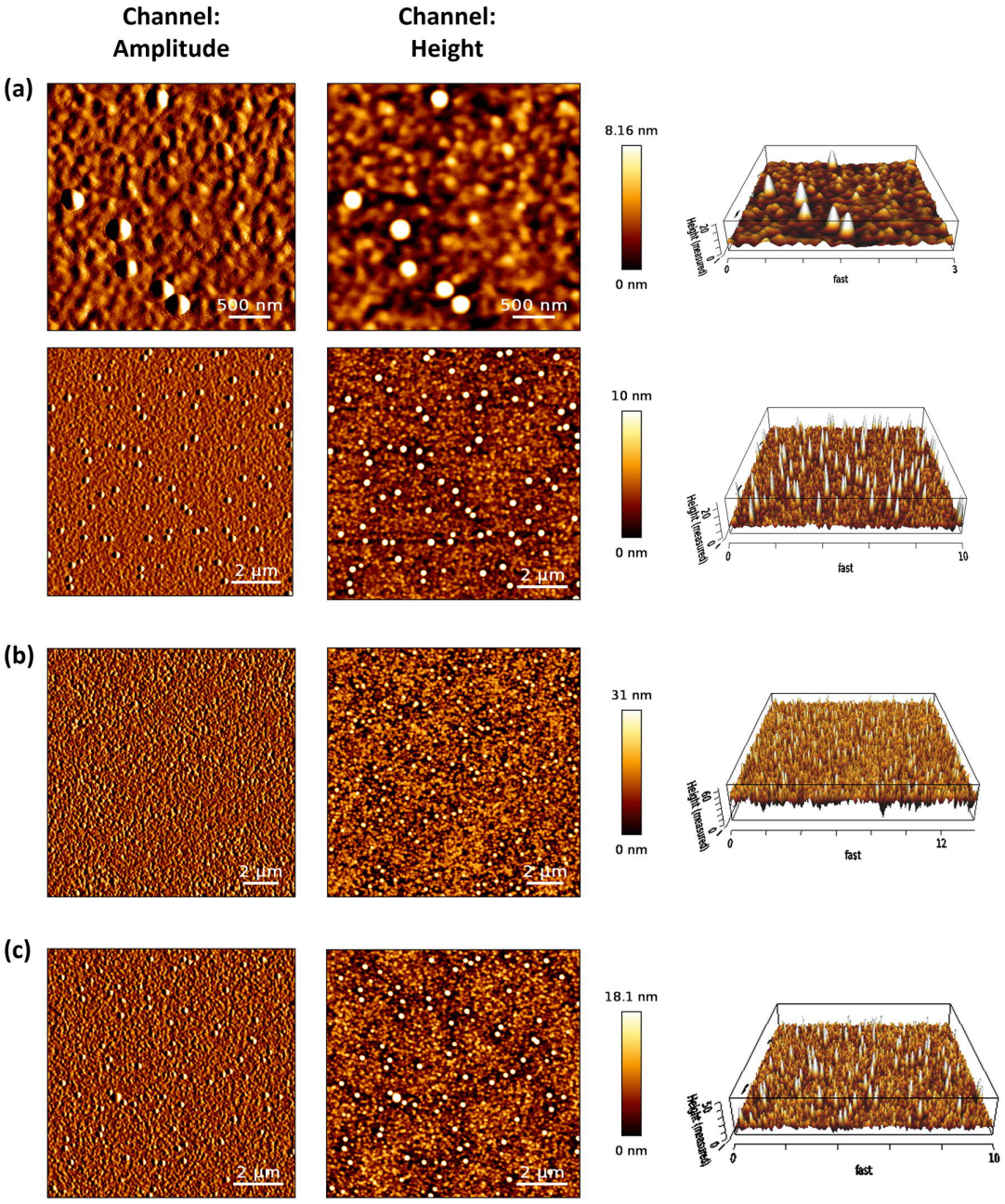

Figure 3- 11: AFM amplitude, 2D height and 3D height (topography) images of samples a) IP 10 (500 nm x 500 nm) and (2 µm x 2 µm), b) IP 15 (2 µm x 2 µm), and c) IP 20 (2 µm x 2 µm).

Spectroscopic Environmental Ellipsometry porosimetry (EEP) experiments were also carried out for another set of pCN thin films, deposited on a silicon substrate, varying the melamine amount, to investigate the presence of micropores. The measurements were made in collaboration with Dr. Cédric Boissiere at the Sorbonne University/ Laboratory of condensed

matter chemistry of Paris (LCMCP). The EEP technique basically consists of tracking the variations of the refractive index and thickness of the thin film when inducing the change of partial pressure of an organic solvent passing through the film inside a controlled chamber. The results are then plotted into an adsorption-desorption isotherm[103–105]. The EEP setup was recently developed to facilitate the study of porous thin films since it is not possible to use gas physisorption data, analyzed using the BET (Brunauer-Emmett-Teller) theory, for measuring the pores of thin films.

For the measurements, the pCN thin films were mounted inside the chamber, located on the ellipsometer sample stage. The incidence angle of the ellipsometer was set at 70° for all the samples. First, the thin film's properties were measured without any influence of a gas flow. Then, at atmospheric pressure, a dynamic flux of air containing a controlled relative pressure of isopropanol for the first experiment and ethanol for the second one was applied inside the chamber onto the thin film. The isotherms can be found in the Appendix (Figure A-7). Since there was no significant change in the refractive index nor thickness of the pCN thins films, no evidence of micropores (smaller than 2 nm) was found.

3.2.1.3 Optical transmittance

The optical transmittances of samples IP 10, IP 15, and IP 20 were measured in the UV-VIS-NIR range (350 nm to 3000 nm), and the spectra are shown in Figure 3- 12. As it can be seen, the film with the highest average optical transmittance is the one deposited with the highest amount of precursor (IP 20), with a value of > 80% between the end of the visible spectra and most of the NIR. The decrease in the average transmittance for samples IP 10 and IP 15 at the same wavelength range can be attributed to the higher absorption of the samples due to a higher conjugation of the polymer chains. The decrease in transmittance can also be explained due to morphological changes. Rougher samples result in higher reflection losses and induced surface scattering, which would explain why sample IP 15 has the lowest transmission (higher roughness). There is no significant shift in the absorption edge in the UV from sample to sample.

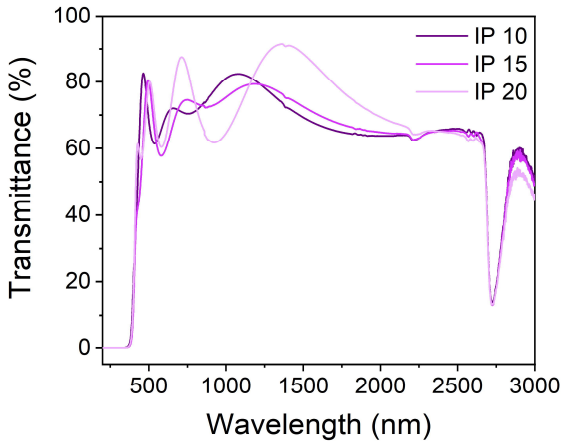

Figure 3- 12: UV-VIS-NIR transmittance spectra of pCN thin films synthesized with changing the precursor amount (IP 10, IP 15, and IP 20).

3.2.2 Influence of process time

Another critical parameter in CVD processes is the synthesis time. To study the effect of the deposition time on the pCN thin films, the same process steps described previously in Section 3.2.1 were used. The difference here is in Step 4, which is the polymerization process. It was now increased from 30 min (t-1) to 60 min (t-2) and 90 min (t-3), as seen in Table 4.

Table 4: CVD parameters for investigation on the influence of process time.

pCN 20g		**Step 1**	**Step 2**	**Step 3**	**Step 4**	**Step 5**	**Step 6**
Upstream (°C)	-	0	0	300	300	0	0
Downstream (°C)	-	0	550	550	550	550	0
Heater time (min)	**t-1**	10	40	30	**30**	30	2
	t-2	10	40	30	**60**	30	2
	t-3	10	40	30	**90**	30	2
N_2 gas set (SCCM)	-	500	50	50	50	50	0
Pressure set (Torr)	-	10	10	10	10	10	10

Also, from now on, the precursor amount was kept at 20g for two main reasons: to check if it was possible to re-optimize the process for this quantity of reactant by changing just one parameter in comparison to the previous section, and to try to obtain thicker thin films without losing the most relevant optical properties. That means that samples IP 20 and t-1 are the same, and some of the characterizations from sample t-1 are omitted further in this section since they were already presented in the previous one as IP 20.

3.2.2.1 Spectroscopic Ellipsometry – dispersion parameters and molecular orientation

The influence of the deposition time on the dispersion parameters was investigated using ellipsometry, with the same set parameters and function model as described in the previous section. All the results are shown below in Figure 3- 13. Thicknesses and optical constants values in the in-plane and out-of-plane are given in Table 5. Details about the modeling can be found in the Appendix (Figures A-7 and A-8).

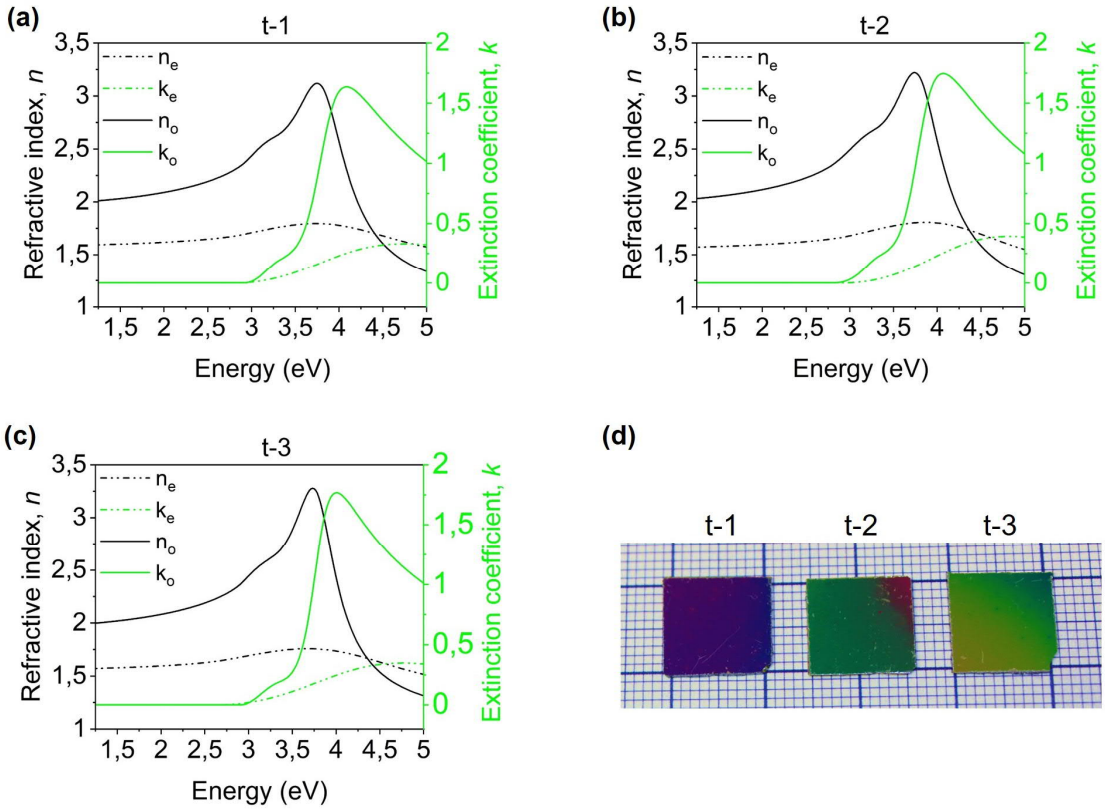

Figure 3- 13: Influence of deposition time on dispersion parameters in the in-plane (n_o, k_o) and out-of-plane (n_e, k_e) using 20g of melamine with times (a) t-1/ shorter, (b) t-2, and (c) t-3/ longer, deposited on a silicon wafer. (d) Picture of the correspondent samples, from left to right: t-1, t-2, and t-3.

As observed in the spectra in Figure 3- 13, there is no considerable influence on the structure and composition when changing the polymerization time between 30 and 90 min. The values of n_o and n_e are practically the same for samples t-1 and t-3, while the dispersion behavior of the refractive index changes slightly in sample t-2. Since there is no apparent significant change in structure, we assume that the optical dispersion variations are due to the thickness of the samples and small displacements from the stacking layers. The maxima extinction coefficient is again at 4 eV, typical for carbon nitrides, ranging from 1.6 to 1.77, not linearly with the thickness nor polymerization time.

Table 5: Influence of process time on the thickness and refractive index (n_o and n_e) at 630 nm wavelength and extinction coefficients (k_o and k_e) at 309 nm.

pCN 20g (time)	Thickness (nm)	n_o @630 nm (1.97 eV)	n_e @630 nm (1.97 eV)	k_o @309 nm (4 eV)	k_e @309 nm (4 eV)
t-1	195.31	2.08	1.62	1.6	0.23
t-2	346.59	2.11	1.59	1.75	0.25
t-3	280.27	2.08	1.59	1.77	0.24

Furthermore, the sample thickness increased considerably from t-1 to t-2, but decreased at t-3. After a certain period of time, the precursor is completely consumed in the reactor, and there is a lack of correct feed vapor composition. In such a non-equilibrium reactor-starved scenario caused by the overall depletion of the reactant, the growth rate decreases substantially, resulting in the thinning of the film. In addition to that, the inert gas also continues to hit the wafer without further material to polymerize (limited feed rate), facilitating the thinning of the film.

3.2.2.2 pCN thin films composition and C/N ratio

The set of samples produced with changing the polymerization time was also analyzed by XPS to gain more knowledge about the bonding states in the pCN thin films. Figure 3- 14 compares the C1s and N1s spectra obtained for samples t-1, t-2, and t-3. The deconvolution of both C1s and N1s core level spectra has revealed the same peaks for the samples synthesized using different melamine amounts but with different percentages. For the C1s spectra, at around 283.5-285 eV, peaks are attributed C-C hydrocarbon bonds from contamination during sample handling and transportation. Table 6 shows the composition of each sample extracted from the XPS spectra. It is important to remember that sample t-1 is the same as sample IP 20 (20 g of melamine, 30 min of polymerization), and it would not be discussed in details in this section. The difference in the contamination content is due to the fact that the samples were exposed to air during longer or shorter times. Peaks at 288.30 eV (t-1), 288.23 eV (t-2), and 288.36 eV (t-3) are related to sp^2 carbons (N-C=N). The weak signal at 287 eV corresponds to oxidized carbon due to contamination, and another weak peak at 294 eV is attributed to the C π-π^* transition.

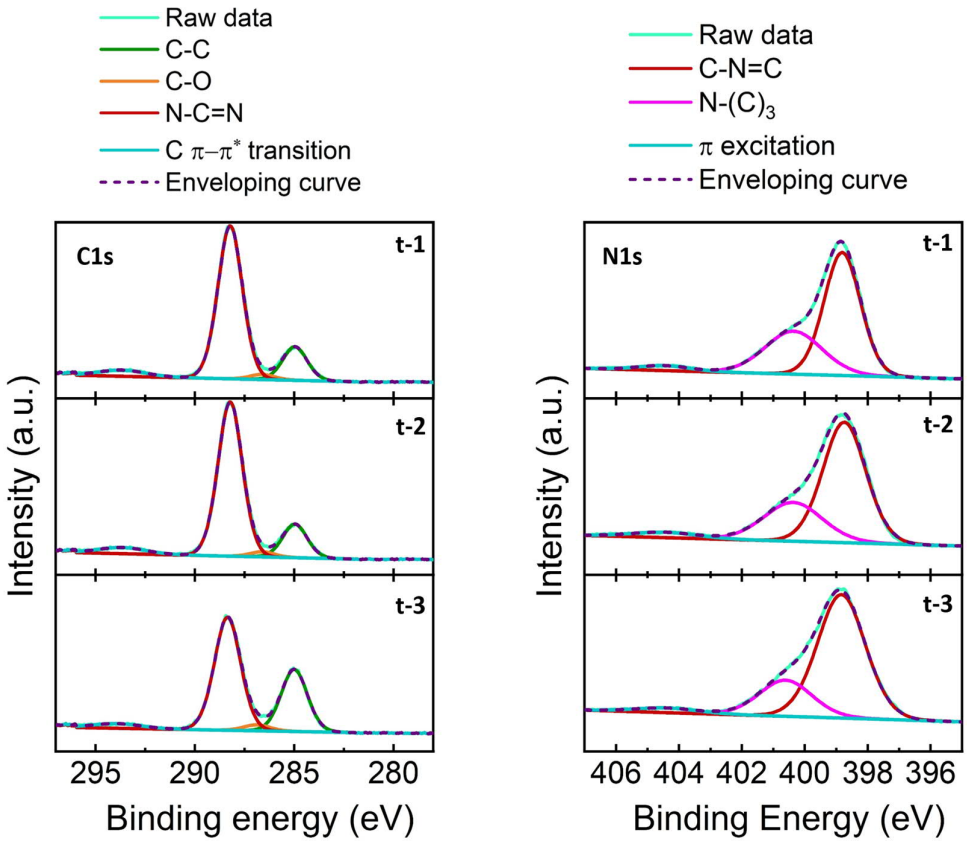

Figure 3- 14: XPS C1s and N1s spectra of samples t-1, t-2, and t-3.

The N1s spectra reveal prominent peaks at 398.84 eV (t-1), 398.74 eV (t-2), and 398.87 eV (t-3), which are attributed to C-N=C. The peaks at higher binding energies are related to sp^3 bonded $N-(C)_3$ and located at 400.61 eV (t-1), 400.39 eV (t-2), and 400.46 eV (t-3). There is a significant shift for $N-(C)_3$ between these samples, which could be explained by the increase in the hydrogen bonding content as the peak gets broader. The signal at 404 eV is attributed to charging effects.

The calculated C/N ratio for t-2 and t-3 from the extracted XPS data was 0.72 and 0.79, respectively. The C/N ratio increased with the time of polymerization due to the increase of the N-C=N bonds.

Table 6: Bonding types and composition as determined by the XPS spectra (C1s and N1s) for pCN samples deposited with different polymerization times.

pCN 20g (time)	N-C=N (C1s)	C-N=C (N1s)	$N-(C)_3$ (N1s)	C/N
t-1	41%	44%	14%	0.71
t-2	42%	40%	18%	0.72
t-3	44%	36%	20%	0.79

When changing the reaction polymerization time, the XPS spectra and standard ellipsometry results did not follow precisely the same behavior for the set of samples before, when comparing each other. The sample t-3 was the one with the lowest content of C-N=C bonds but not with the highest n_e at 630 nm. Also, it had the lowest k_e, not following the previous explanation that having more $N-(C)_3$ bonds would enhance the polymer chain length/conjugation. It would actually work in the opposite way, the more C-N=C bonds, the higher the absorption. The sample with the highest C-N=C content was t-1, which had the highest n_e for this set of samples.

Figure 3- 15 shows the SEM images for samples t-2 (a) and t-3 (b). The same grain structure as seen for the samples with different amounts of the precursor is depicted. However, the samples have a much more similar structure to sample IP 20 (t-1) because the same melamine amount was used. Sample t-2 (a) shows a more condensed and smoother surface than the sample with a longer polymerization time, t-3 (b). Furthermore, the layered structure is not so clear in the image with higher magnification for t-3, looking more like a columnar thin film growth. Also, the bigger spheroids on the sample surface seem to have a repetition pattern. Still, in the same image, it is possible to see some scratches that go through those bigger particles, where there is a change in the image's contrast. This change in the contrast indicates that the particles have a core-shell structure, as previously reported in this thesis for sample IP 15. Additional SEM pictures can be found in the Appendix (Figure A-9).

Moreover, the cross-section of the thin film edge in Figure 3- 15(a) shows some wrinkled spots between the polymer layers. We attribute the formation of the wrinkles to residual stresses originated from the temperature changes in the chemical vapor deposition process. The thermal

expansion mismatch between the substrate and the pCN can cause compressive stresses into the thin film, and so the system can release this internal stress, delamination occurs[106,107]. Yu and Hutchinson[108] have studied the mechanism underlying the thermal delamination of thin films due to film/substrate thermal mismatch. The authors have found that the stresses caused by the thermal contraction of the underlying substrate are transferred to the thin film through shear stresses on the interfaces close to the film edges.

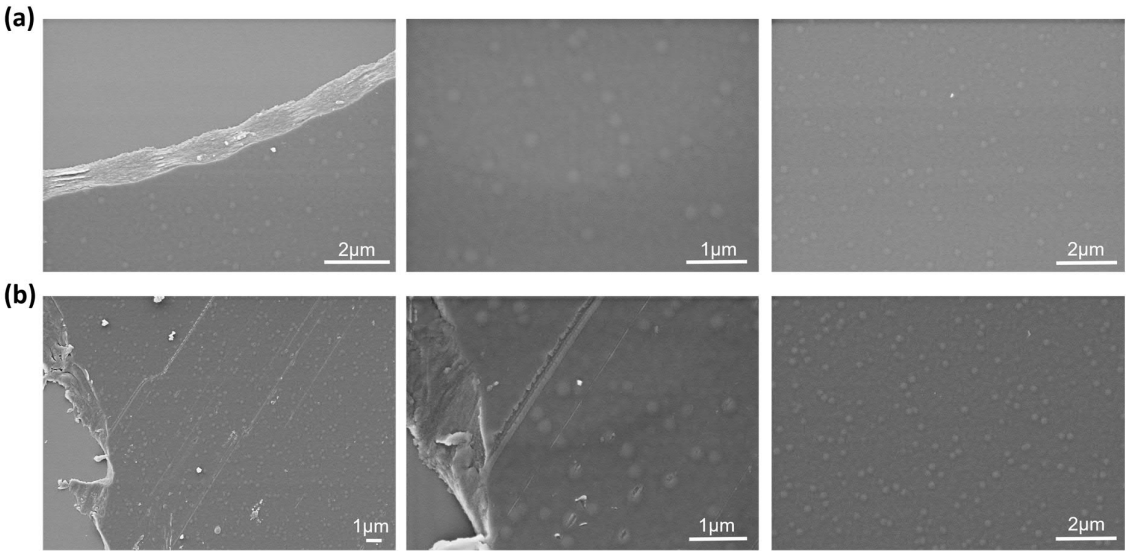

Figure 3- 15: SEM images of samples a) t-2 (from left to right: 10 kx/ 3 kV, 20 kx/ 3 kV, 10 kx/ 3kV) and b) t-3 (from left to right: 5 kx/ 3 kV, 20 kx/ 3 kV, 10 kx/ 3 kV) deposited on a silicon substrate.

According to the elemental mapping from EDX measurements presented in Figure 3- 16, carbon and nitrogen are homogenously distributed through the sample.

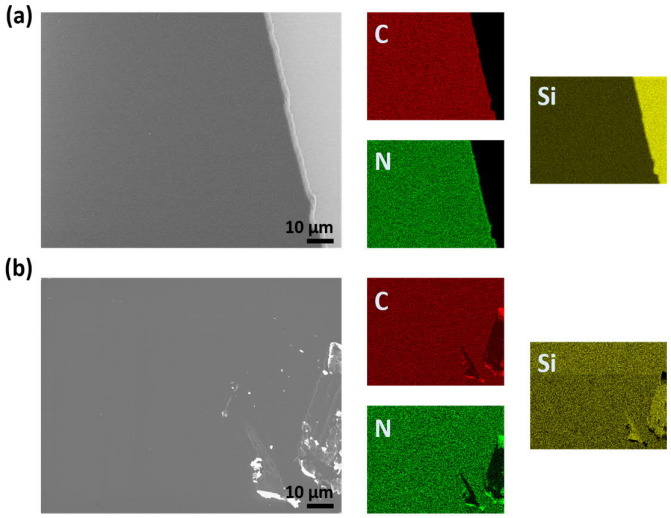

Figure 3- 16: SEM images and respective EDX elemental mapping of samples a) t-2 (60 min polymerization) and b) t-3 (90 min polymerization) for carbon (red), nitrogen (green), and silicon (yellow).

XRD and IR ellipsometry measurements had the same interpretation as before and can be found in the Appendix (Figure A-10 and Figure A-11, respectively). Additionally, the nanoindentation measurements (Appendix, Tables A-4 and A-5)) have shown a Young's Modulus of 14.8 ± 1.4 GPa for sample t-2 and 15.3 ± 1.9 GPa for sample t-3. Compared with the value of 20.5 ± 2.9 GPa from sample t-3 (IP 20), the thinnest film still follows the trend of having the highest elastic modulus. However, it does not occur between samples t-2 and t-3, although they show a considerably small change.

AFM amplitude and topography images scanned in tapping mode (Figure 3- 17) do not show considerable alterations from the images acquired with the previous set of samples. The grain boundary patterns are still the same, and the particles have the same size, in the range of 100-200 nm, which agrees with the SEM images.

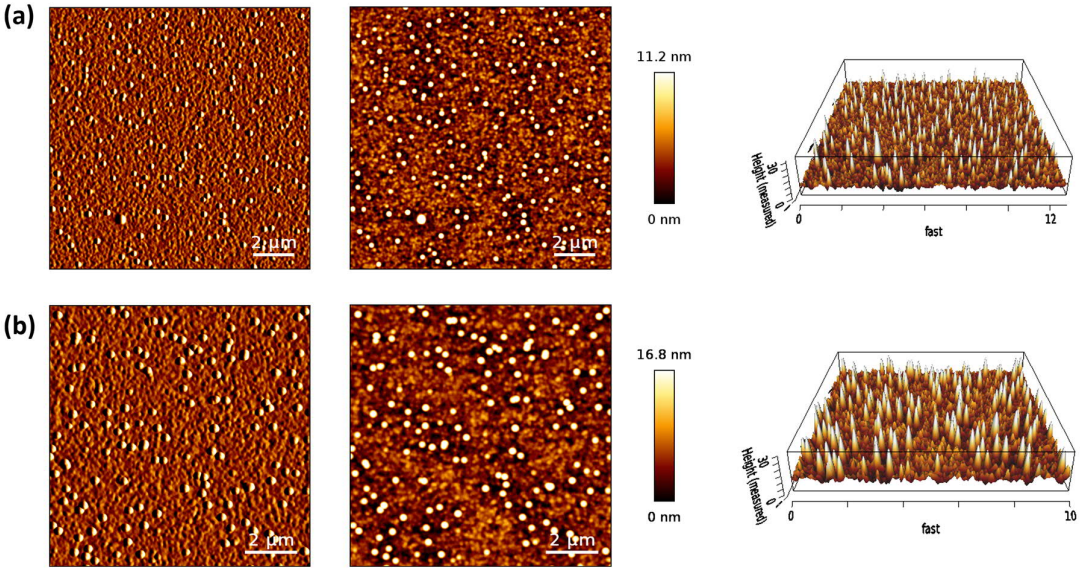

Figure 3- 17: AFM amplitude, 2D height and 3D height (topography) images (2 µm x 2 µm) of samples a) t-2 and b) t-3.

The RMS roughness calculated from the height counts of the (2 µm x 2 µm) imaged area is 2.321 nm and 3.653 nm for samples t-2 and t-3, respectively. In this case, the roughness did not follow an increase with the sample thickness but with the polymerization time. It indicates that sample t-3 has probably developed more nucleation sites during growth due to more random atoms being adsorbed and desorbed from the surface at a more prolonged reaction time.

3.2.2.3 Optical transmittance

The UV-VIS-NIR transmittance spectra for samples t-1, t-2, and t-3 are depicted in Figure 3-18. The thin film synthesized with a polymerization time of 30 min (t-1) is the one with the highest average optical transmittance with a large transparency window in the NIR range. Sample t-2 and t-3, which had a longer polymerization time, also have a transmittance average of > 80%. The difference between these two samples and sample t-1 is that there is a significant red shift in the NIR region for longer polymerization times. The increase and decrease patterns through the UV-vis region of the transmittance spectra, especially for sample t-2, are attributed to the interferences fringes. This pattern is affected by the thickness of the thin film since more layers create more interferences.

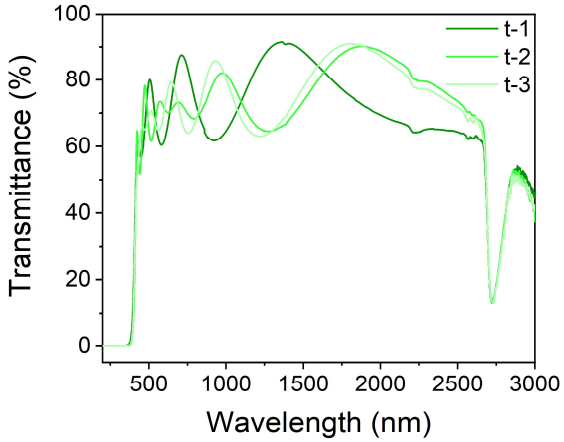

Figure 3- 18: UV-VIS-NIR transmittance spectra of pCN thin films synthesized with changing the polymerization time (t-1, t-2 and t-3).

3.2.3 Influence of N_2 flow rate

Another critical factor for the successful growth of high-quality pCN thin films is the flow rate control for the carrier gas. As described earlier, N_2 was only used as a carrier, meaning it should not influence the thin film's nitrogen content. To investigate the effects of different flow rates of N_2 on the properties of the thin films, the polymerization time was maintained at 30 min, the pressure at 10 Torr, and the amount of precursor at 20 g. Sample fw-2 had a flow rate of 500 SCCM (standard cubic centimeters per minute), just as all the samples from the two previous sections. Thus, fw-2 is the same sample as IP 20 and t-1. For samples fw-1 and fw-3, the flow rate was decreased in half and doubled increased, respectively, as shown in Table 7.

Additionally, the carrier gas flow rate can directly influence the absorption, desorption of intermediate compounds, and re-adsorption on the substrate. Hence, varying this parameter is essential to learn how to control surface reactions and the growth rate of the thin films[109].

Table 7: CVD parameters for investigation on the influence of N_2 flow rate.

pCN 20g		**Step 1**	**Step 2**	**Step 3**	**Step 4**	**Step 5**	**Step 6**
Upstream (ºC)	-	0	0	300	300	0	0
Downstream (ºC)	-	0	550	550	550	550	0
Heater time (min)	-	10	40	30	30	30	2
N_2 gas set (SCCM)	**fw-1**	500	**25**	**25**	**25**	**25**	0
	fw-2	500	**50**	**50**	**50**	**50**	0
	fw-3	500	**100**	**100**	**100**	**100**	0
Pressure set (Torr)	-	10	10	10	10	10	10

3.2.3.1 Spectroscopic Ellipsometry – dispersion parameters and molecular orientation

Ellipsometry measurements for samples fw-1 (25 SCCM), fw-2 (50 SCCM), and fw-3 (100 SCCM) were performed as described previously. The results are presented in Figure 3- 19. There is a considerably high difference between the spectra regarding the dispersion behavior of both in-plane and out-of-plane parameters. At the lowest N_2 flow rate used (a), the extinction coefficient normal to the plane, k_e, remains at zero for the whole measured wavelength range, meaning that the polymer chains are much more preferentially align parallel to the substrate plane. For samples fw-2 (b) and fw-3 (c), the optical parameters' changes in the perpendicular direction are much more evident.

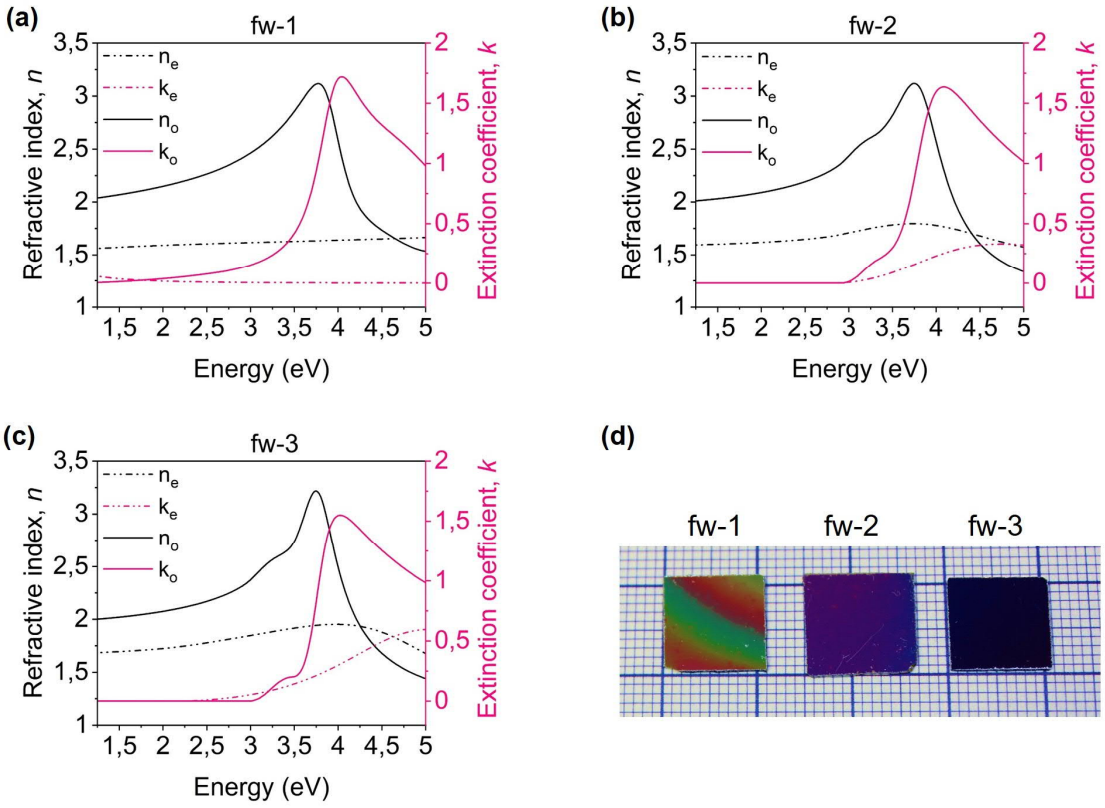

Figure 3- 19: Influence of N_2 flow rate on dispersion parameters in the in-plane (n_o, k_o) and out-of-plane (n_e, k_e) using 20g of melamine with times (a) fw-1, (b) fw-2, and (c) fw-3, deposited on a silicon wafer. (d) Picture of the correspondent samples, from left to right: fw-1, fw-2, and fw-3.

As a matter of comparison, sample thicknesses and values of ordinary and extraordinary refractive indices at 630 nm and extinction coefficients at 309 nm are described in Table 8. The thickness of the thin film decreases with the flow rate, indicating that the gas is, most probably, not just carrying the sublimated intermediates to condense on the substrate surface but also transporting some of the s-triazines away from the substrate.

Table 8: Influence of N_2 flow rate on the thickness and refractive index (n_o and n_e) at 630 nm wavelength and extinction coefficients (k_o and k_e) at 309 nm.

pCN 20g (flow rate)	Thickness (nm)	n_o @630 nm (1.97 eV)	n_e @630 nm (1.97 eV)	k_o @309 nm (4 eV)	k_e @309 nm (4 eV)
fw-1	631.33	2.14	1.59	1.7	0.002
fw-2	195.31	2.08	1.62	1.75	0.25
fw-3	67.02	2.07	1.72	1.55	0.30

An increase of the N_2 flow rate also resulted in lower refractive indices in the in-plane (but higher ones in the out-of-plane) and higher extinction coefficients in the direction normal to the plane, at the considered energy range. It suggests that by increasing the flow rate and 'losing' s-triazines, a more significant part of the polymer chains aligns in the perpendicular direction.

3.2.3.2 pCN thin films composition and morphology

The C1s and N1s core level XPS spectra for the samples synthesized using different gas carrier flow rates are shown in Figure 3- 20. The percentages corresponding to each bonding state extracted by the deconvolution of the mentioned spectra are presented in Table 9. The most dominant peak for the C1s spectra, at 288.3 eV (fw-1) and 288.25 eV (fw-3), corresponds to the sp^2 carbon of the heptazine rings (N-C=N). Sample fw-2 was characterized previously as IP 20 and t-1. The C-C bond peak from adventitious carbon at 285 eV was also deconvoluted, as well as the weak peak at 294 eV attributed to C π-π^* transitions.

The two peaks were extracted from the N1s spectra. The most intense one at lower energies was located at 398.88 and 398.79 eV for samples fw-1 and fw-3, respectively, and it is related to the C-N=C bonds of the heptazines. The weaker peak located at 460.60 eV for sample fw-1 and 460.26 eV for sample fw-3 is attributed to sp^3 bonded nitrogen. There is a considerable shift in between this last peak for samples fw-1 and fw-3, to which we could relate the hydrogen bonding amounts to the broadness of the peak.

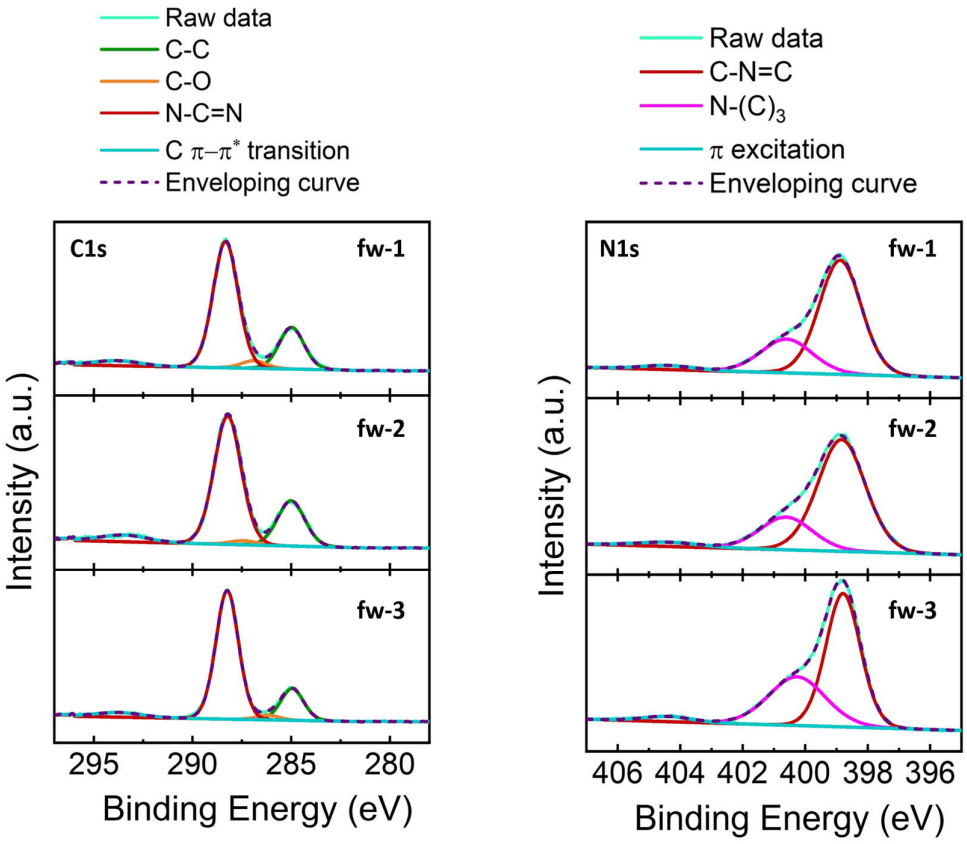

Figure 3- 20: XPS C1s and N1s spectra of samples fw-1, fw-2, and fw-3.

The calculated C/N ratio from the values presented in the three first rows of Table 9 were 0.74, 0.71, and 0.72. Due to the lower percentage of N-$(C)_3$ bonds, the thin film grown using a 50 SCCM gas carrier flow (fw-2) had the lowest C/N ratio. However, it did not follow a trend with the increase of the flow rate. With the flow rate set to 100 SCCM, the C/N ratio slightly increased, as it did with 25 SCMM when compared to 50 SCCM.

Table 9: Bonding types and composition as determined by the XPS spectra (C1s and N1s) for pCN samples deposited with different N_2 flow rates.

pCN 20g (flow rate)	N-C=N (C1s)	C-N=C (N1s)	N-$(C)_3$ (N1s)	C/N
fw-1	42%	42%	15%	0.74
fw-2	41%	44%	14%	0.71
fw-3	42%	36%	22%	0.72

When comparing the XPS data to the ellipsometry results, the sample with the lowest amount of N-$(C)_3$ bonds is the sample with a higher extinction coefficient in the in-plane direction. This result agrees with the previous set of samples (t-x) when saying that having more C-N=C bonds would result in higher absorption. However, it is important to emphasize that the first set of samples (IP-x) did not follow the same trend, possibly due to errors during data manipulation with the modeling of the optical dispersion or the deconvolution of the XPS peaks. Also, XPS is not reliably comparable to the ellipsometry data because it considers only the surface composition of the thin films.

The SEM images in Figure 3- 21 show the surface morphology of samples fw-1 (a) and fw-3 (b). From the pictures near the edges, it is evident that the samples have a layered structure, although they seem somehow irregularly distributed. Although it is also possible to see the spheroids distribution on the surface of the samples, with the same sizes as discussed previously for the other samples, the images in (a) show that sample fw-1 have a much higher compact structure indicating a higher degree of condensation. In the images presented in (b), those "residual" spheroids are almost entirely gone, and the overall surface seems much more tightly and uniformly packed. Additional SEM pictures can be found in the Appendix (Figure A-12).

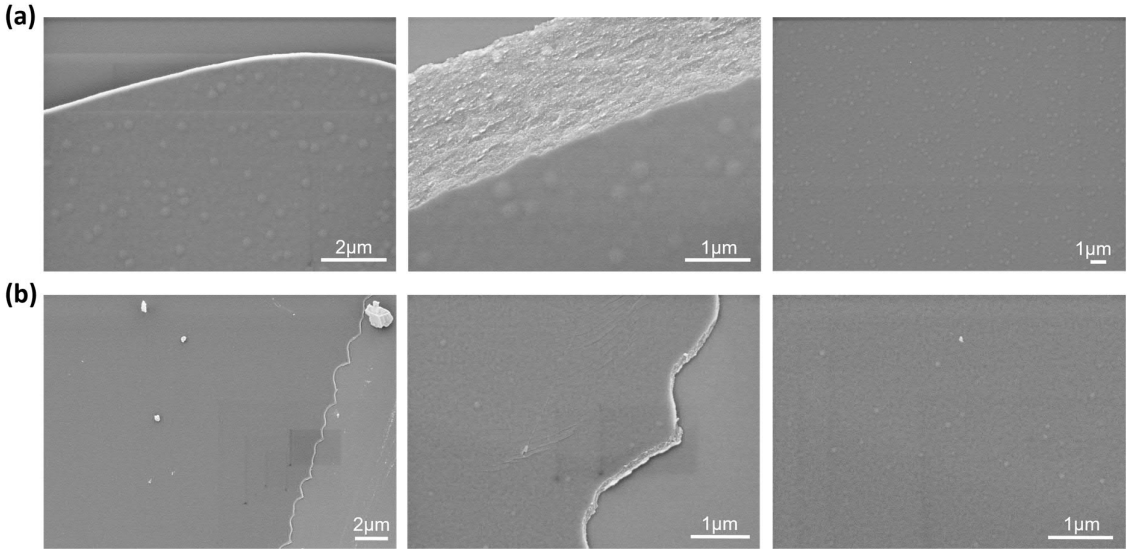

Figure 3- 21: SEM images of samples a) fw-1 (from left to right: 10 kx/ 3 kV, 20 kx/ 3kV, 5 kx/ 3 kV) and b) fw-3 (from left to right: 5 kx/ 3 kV, 20 kx/ 3 kV, 20 kx/ 3 kV) deposited on a silicon substrate.

EDX elemental mapping images are presented in Figure 3- 22 and show that the elements carbon and nitrogen are uniformly distributed through both samples (a) fw-1 and (b) fw-3.

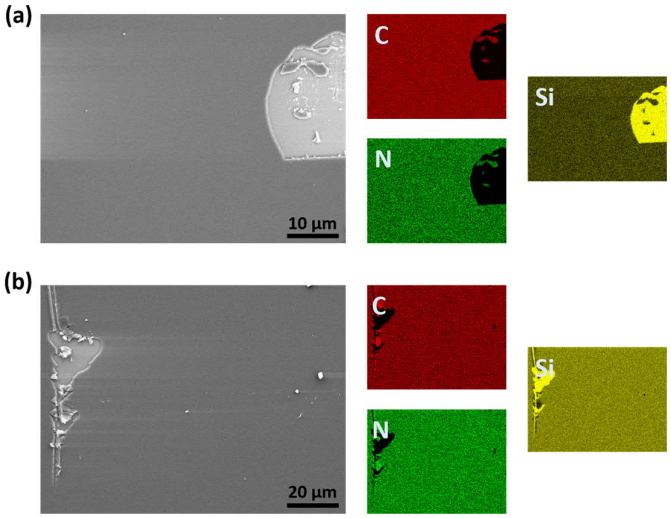

Figure 3- 22: SEM images and respective EDX elemental mapping of samples a) fw-1 (25 SCCM) and b) fw-3 (100 SCCM) for carbon (red), nitrogen (green) and silicon (yellow).

The Young's Modulus was calculated from nanoindentation measurements (Appendix, Tables A-6 and A-7)). Sample fw-1 had an elastic modulus of 13.4 ± 1.5 GPa and sample fw-3, 22 ±

4.7 GPa. For sample fw-3, the penetration depth used was 7 nm, and resulted in a much larger standard deviation. Again, the elastic modulus has shown a dependence on the sample thickness, with the thinnest thin film being the stiffest.

To further investigate the morphology of the thin films, AFM characterizations were employed, and the results are presented in Figure 3- 23. The images were taken over a scan area of 500 nm x 500 nm due to a higher discrepancy between this set of samples and the ones characterized previously. The RMS roughness was calculated over a scan area of 2 μm x 2 μm. Sample fw-1 has a roughness of 4.001 nm and sample fw-3, 5.597 nm. The difference in the roughness is due to a larger distribution of the grain sizes.

As seen previously in the SEM images, the morphology and grain distributions are quite different from samples IP-x and t-x. Samples fw-1 and fw-3 have a higher homogeneity and an increased amount of linked grains, each with a consistent size around 100 nm, similar to the morphology of the fw-2 sample (IP 20 and t-1). The AFM figures of sample fw-1 (a) scanned over a 500 nm x 500 nm area show the formation of elongated grains, indicating part of the coalescence process. Sample fw-3 (b) has much more grain boundaries than samples fw-1 and fw-2.

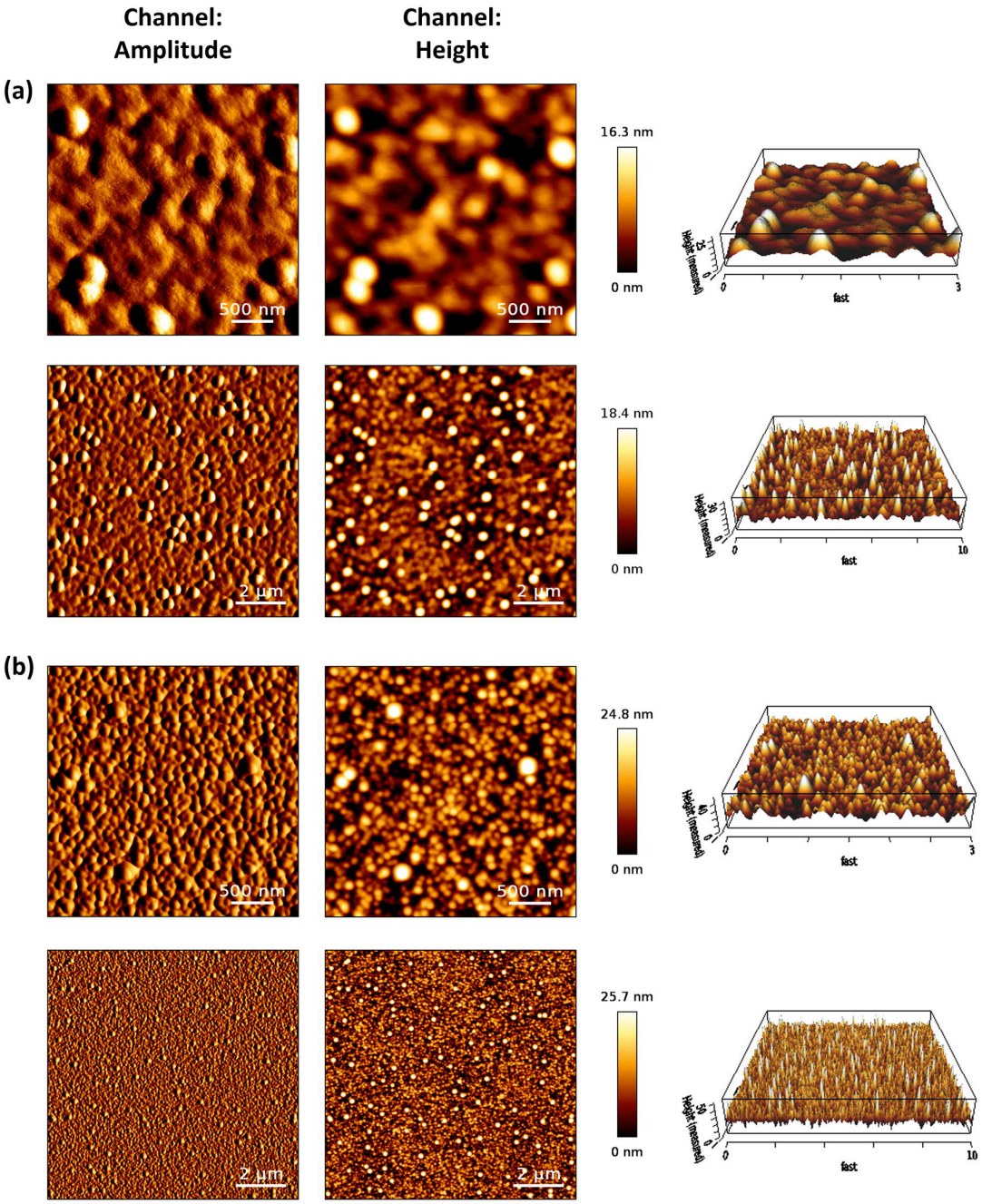

Figure 3- 23: AFM amplitude, 2D height and 3D height (topography) images (500 nm x 500 nm and 2 µm x 2 µm) of samples a) fw-1 and b) fw-3.

3.2.3.3 Optical transmittance

The UV-VIS-NIR range optical transmittance spectra of samples fw-1, fw-2, and fw-3 are shown in Figure 3- 24. The sample with the lowest nitrogen flow rate (fw-1) presents more interference patterns due to its thickness of 631.33 nm. The highest transmittance average of > 80% is achieved with the sample fw-2, while the transmittance decreases significantly between 1000 and 1700 nm with the fw-3 sample. However, the sample fw-3 is the one with the highest transparency in the visible region due to its lower absorption and thinner stack.

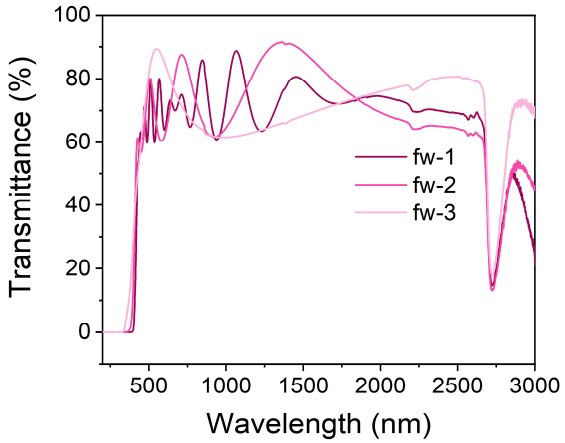

Figure 3- 24: UV-VIS-NIR transmittance spectra of pCN thin films synthesized with different N_2 flow rates (fw-1, fw-2, and fw-3).

3.3 Conclusions

High-quality and transparent polymeric carbon nitride thin films were successfully synthesized from a sustainable and relatively low-cost precursor under different chemical vapor deposition conditions. Changes in the refractive index, extinction coefficient, C/N ratio, and morphology of the thin films occurred with changing the amount of precursor used, the polymerization time, and the carrier gas flow, although not linearly. Non-zero values of the extinction coefficient in the direction perpendicular to the substrate surface have revealed a high anisotropy in the optical constants due to the change in orientation of some parts of the molecular chain from the in-plane direction to the out-of-plane. Since the optical anisotropy did not change linearly with the thickness for any set of samples, it was addressed to the change in composition and structure of the thin films. Increasing both the precursor amount and polymerization time has reached an extrapolation point, from which the thickness stops increasing and starts to reduce due to the presence of higher amounts of reactant per volume than the set parameters can support. When reaching this limit, changes in the film structure and distribution of grain sizes also occur, mainly induced from gas-phase nucleations. The roughness of the thin films also increased with the polymerization time due to the formation of more nucleation sites. A change in the broadness of the deconvoluted N1s XPS spectra indicates that due to a higher hydrogen bonding content between heptazine chains, the N-$(C)_3$ peaks get broader.

Chapter 4

In situ on-surface polymerization of pCN

The real structure of polymeric carbon nitride thin films is still under debate. Growing polymeric carbon nitride thin films on high symmetry surface planes as Cu (111) could give a new insight into the heptazine building blocks' conjugation and a more defined condensed structure. In this study, we report the *in situ* on-surface polymerization of carbon nitride thin films via chemical vapor deposition using melamine as a precursor under ultra-high vacuum (UHV) conditions. As a first step towards understanding the Cu (111) mediated reaction under the influence of increasing the substrate temperature, the thermal annealing experiments are followed by low-temperature scanning tunneling microscopy (STM) and non-contact atomic force microscopy (nc-AFM) with a metallic probe tip, which is functionalized at the tip terminations, resulting in imaging structural and chemical properties of the thin films with extreme precision. In scanning probe microscopy (SPM), functionalizing the microscope's tip apex strongly interferes with the imaging mechanisms. Having suitable, atomically well-defined terminations on the probe tip have been reported to be a key operation for imaging nanostructures on the atomic scale[110–114].

Gross et al.[110] have demonstrated, in 2009, that picking up a single CO molecule from a copper substrate surface onto a metallic tip during nc-AFM experiments led to small oscillation amplitudes and to the possibility of resolving atomic positions and bonds. From this moment forth, functionalizing the bulk copper apex of the tip with a single oxygen atom allowed imaging with submolecular resolution. However, CO-functionalized tips are quite flexible and can bend to reduce the interactions between the tip and the sample. That is a major drawback since this flexibility leads to the tilt of the CO molecule at the tip apex, resulting in considerable lateral deflection of the probe particles during scanning and, hence, to image ditortions[111,115].

Different alternatives have been recently proposed to overcome the imaging artifacts due to tip flexibility and increase the resolution. One option, for example, is to slightly indent the nc-AFM tip to a partially oxidized copper surface, resulting in the chemical passivation of the tip by the oxygen, meaning the oxygen atom gets covalently connected in a tetrahedral configuration to its upper copper atoms (Figure 4- 1). Due to the strong covalent connection of the terminal oxygen atom, the CuOx system contains a higher structural rigidity when compared to a non-passivated tip, and artifacts due to tip flexibility, such as virtual bonds, can be neglected in this case[112,116]. Moreover, nc-AFM imaging with intramolecular resolution was also previously demonstrated, at liquid nitrogen and room temperatures, with unknown molecules functionalized at the tip termination[117,118].

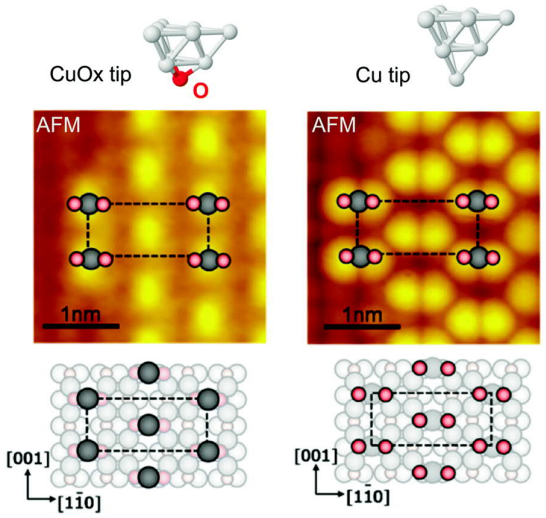

Figure 4- 1: nc-AFM topography images recorded with a CuOx- tip and a pure Cu tip on a c(6x2)O-reconstructed Cu(110) surface[119].

In addition to the CO-functionalized apex, Gross et al.[110] have also performed the low-temperature STM/AFM measurements using a qPlus sensor configuration based on a quartz tuning fork, leading to small oscillation amplitudes. The system facilitates the submolecular nc-AFM imaging at reduced tip-sample distances, where the image contrast is dictated by repulsive forces[111]. This type of configuration has demonstrated several advantages in subatomic resolution AFM imaging compared to traditionally microfabricated silicon cantilevers. Generally, in a high-resolution atomic force microscopy system, the cantilever should have a sharp tip (probe) at its end, and the probe should be sensitive enough to feel the tiny forces acting between individual atoms. For this, three crucial physical properties of the resonators should be considered: the stiffness (k), the eigenfrequency (f_0), and the quality factor (Q). Cantilevers with high stiffness and small oscillation amplitudes (< 1 Å) are desirable to achieve short-range regime forces, where chemical interactions contribute substantially. The energy dissipation (damping) from mechanical oscillations should also be minimized to achieve high force sensitivity, resulting in a high *Q-factor* (Equation 4.1).

$$Q = \frac{2\pi E}{\Delta E_{cycle}} \tag{4.1}$$

Where ΔE_{cycle} is the energy loss per cycle in a damped oscillator, and E is the energy stored in the cantilever ($E = \frac{kA^2}{2}$).

Furthermore, the change of the eigenfrequency with the temperature $\frac{\partial f_0}{\partial T}$ should also be considered since temperature variations can cause the cantilever to bend, affecting f_0 enough to cause a tip-sample drift. One of the main reasons why qPlus sensors often include a quartz tuning fork is that quartz is much more resistant than silicon in terms of thermal drift/frequency variations[120,121].

All of the above mentioned desirable parameters can be attained using a commercial quartz tuning cantilever in q-Plus configuration. Sweetman et al.[117] were able to detect high-contrast intermolecular hydrogen bonds and intramolecular C-C bonds in a 2D naphthalene tetracarboxylic diimide (NTCDI) assembly (Figure 4- 2). The authors identified that the nc-AFM metallic tip termination was functionalized with a NTCDI molecule, working analogously to the CO-terminated tip reported by Gross et al. Nonetheless, qPlus sensors with tungsten tips were used to generate the contrast images.

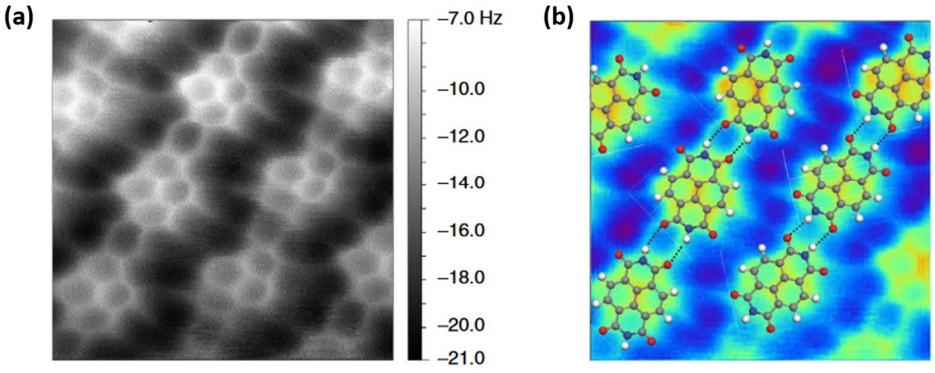

Figure 4- 2: a) Constant height DFM image of a hydrogen-bonded NTCDI island on Ag:Si(111)- (O3xO3) R30°surface acquired at 77 K. Image size 2.1 by 2.0 nm (oscillation amplitude, 275 pm); b) Overlay of the model of NTCDI on a contrast-adjusted section of the image shown in **a**.[117]

Both STM and nc-AFM techniques have the ability to investigate the progression of on-surface reactions and allow the initial, intermediate, and final stages to be characterized. This

approach offers the possibility of understanding chemical reactions deeply, down to submolecular resolution. In this work, the *in situ* STM/nc-AFM experiments were done in collaboration with the Nanoscale Interface Analytics group from the University of Münster and performed by Bertram Schulze Lammers with the help of his supervisor, Dr. Harry Mönig.

4.1 *In situ* experiments on a single crystal copper surface

A crucible was set up inside the high-resolution STM/nc-AFM UHV system to place a small amount of melamine on the evaporator placed near a holder with the substrate, Cu (111), supported by an electrical heating stage. We assume that the deposition happened in the ballistic regime, as it occurs in molecular beam epitaxy (MBE) systems, and that the sublimated molecules traveled in a straight line from the precursor to the substrate. The melamine condensation and deposition into a polymerized carbon nitride structure were followed *in situ* in a low-temperature scanning probe microscopy (SPM) system while increasing crucible and holder temperatures. A commercial quartz tuning fork cantilever in a qPlus force sensor configuration, with an electrochemically etched tungsten wire as a probe tip (f_0 = 28 kHz, *Q-factor* = 5822 at 77 K), was used for imaging both in STM (tip height controlled for contrast adjustment) and nc-AFM (constant-height) configurations. The tip apex was passivated with an unknown sharp molecule during the *in situ* experiments in current mode while indenting the tip onto the melamine samples.

For the first experiment, the melamine temperature inside the electrically heated crucible initially rose up to 100 ºC for 10 minutes, while the Cu(111) was kept at room temperature. In the following experiment, melamine was sublimated at 300 ºC, and the polymerization process took place on the substrate at 250 ± 40ºC (1.9A, 13V) for 30 min, with an addition annealing for 5 min (1.4A, 9V). To further check what would happen when Cu(111) is heated at a higher temperature than that of the pCN polymerization, the maximum power supply available was used in a separated polymerization process. For this, melamine was sublimated at 300 ºC, and the deposition occurred on the substrate at the highest temperature possible for the UHV setup, for 10 min. The maximum substrate temperature was obtained at 2.4A and

20V, implying it was hotter than 600ºC.

Figure 4- 3(a) is a low-temperature STM image acquired during the first experiment. It is possible to see that the monolayer of melamine molecules are adsorbed on the Cu(111), forming an arrangement of flower-shaped domains with linked hexagons, each composed of six melamine molecules, as emphasized in the molecular model shown in Figure 4- 3(b). The model was made based on a previous STM study with melamine structures on Au(111) surfaces[122]. According to the authors, the stabilization of the proposed melamine arrangement is achieved by double hydrogen bonds between the melamine molecules. Our FFT analysis in Figure 4- 3(d) suggests that each flower-shaped reconstruction component aligns along the [11-2] direction with an intermolecular distance of 0.45 nm. It also implies that the melamine molecules are adsorbed on the Cu(111) surface in a vertical configuration[123,124]. In the center of the STM image (a), some melamine rings start to "open", and the polymer chains align in different directions with further annealing. The ring-opening process was already reported by Lin et al. under different conditions[123].

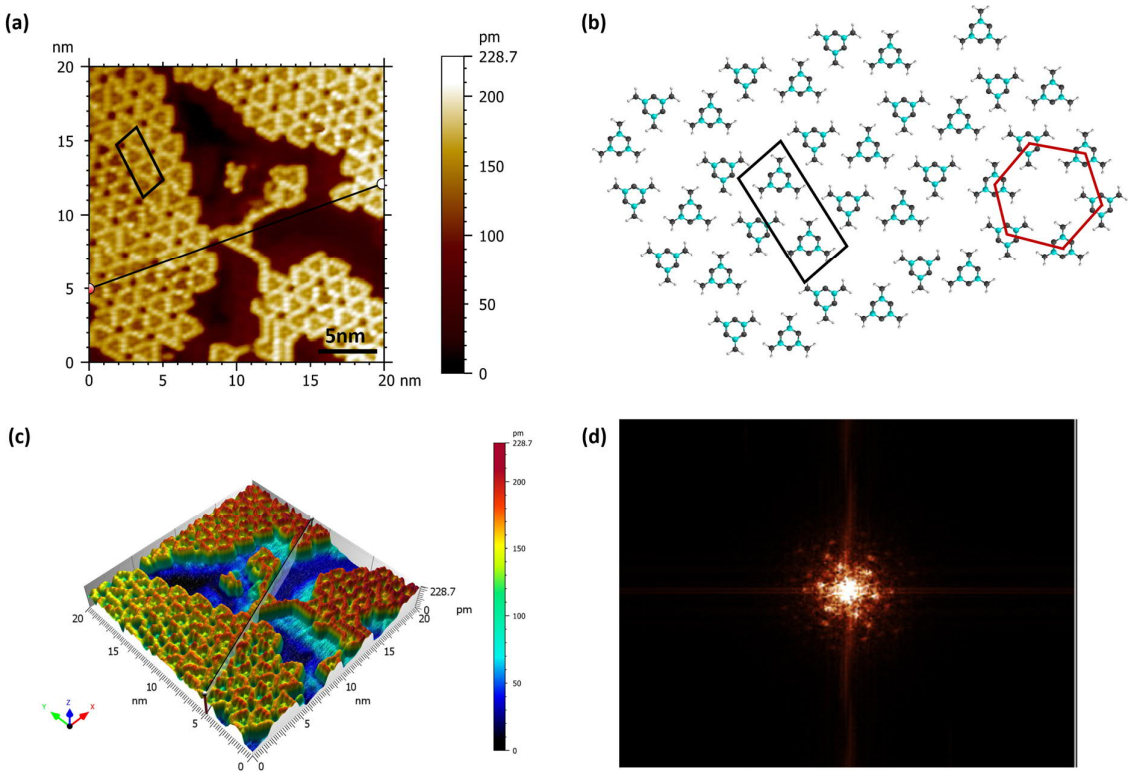

Figure 4- 3: *In situ* STM first polymerization with melamine sublimating at 100 ºC, for 10 min, deposited on Cu(111) at RT. a) STM image with its b) molecular representation (N in blue, C in grey, H in white), c) 3D image, and d) FFT.

Further polymerization and reorganization of the molecular arrangement upon thermal annealing are shown in Figure 4- 4(a). The substrate temperature was around 250 ºC. At this temperature, melamine had already gone through the deamination processes forming melem and, further, melon. But how did we manage to get the polymerized carbon nitride structure at a much lower temperature when doing the *in situ* measurements than the 550 ºC we have used in the CVD reactor? In the case of our STM/nc-AFM setup, the system works under UHV conditions, meaning the pressure inside the chamber is lower than 7.5 x 10^{-10} Torr, while in the CVD system, the reaction was performed under 10 Torr. UHV systems have a much more complex pumping setup than our CVD machine. That is strictly necessary to keep the samples with a spotless surface in the absence of oxidation and any adsorbed contaminations. Also, a UHV setup enables obtaining high quality factors (Q-factors) on the cantilever oscillation. An effective Q-factor of the cantilever has been reported as one of the most critical figures-of-merit of an STM/nc-AFM system in UHV[125]. Besides, in the UHV vacuum regime,

the equilibrium vapor pressure at a given temperature increases. Hence, the sublimation may occur at lower temperatures than in typical reaction chambers at higher pressures. Reducing the pressure allows melamine not only to sublime at lower temperatures but also to avoid decomposition during the deposition process and gas-phase reactions.

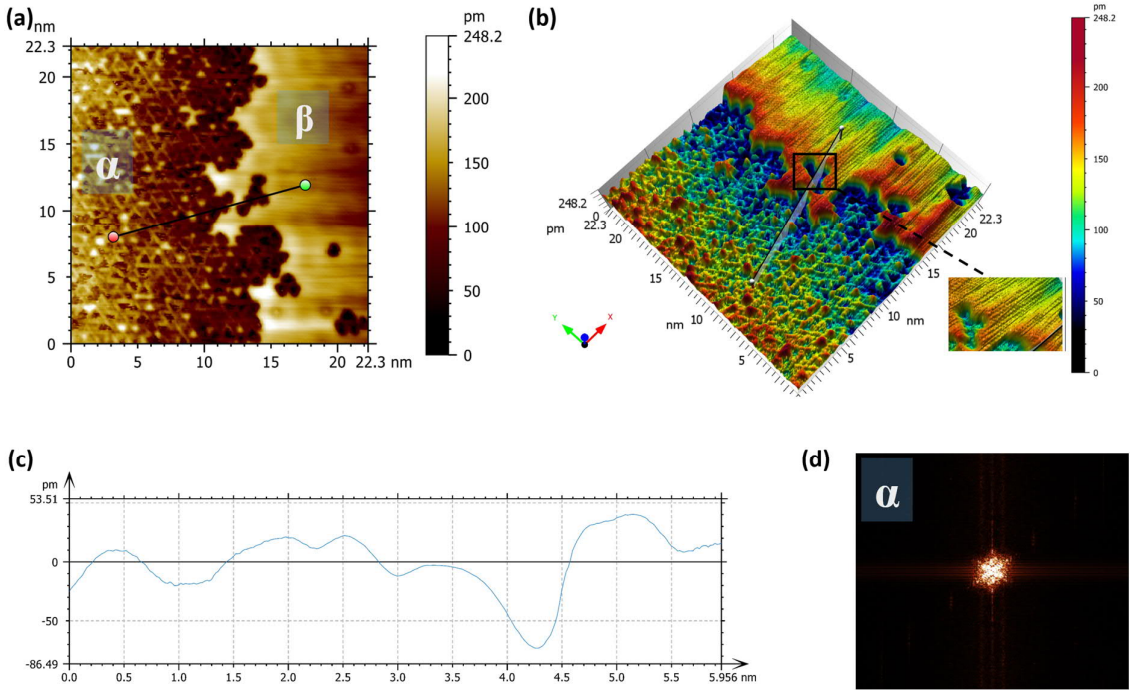

Figure 4- 4: *In situ* STM of the second polymerization process (α and β phases) with melamine sublimating at 300 °C and substrate at 250 °C. a) STM image with its b) 3D image, c) traced profile, and d) α –phase FFT.

It is possible to see perfectly the linked heptazines (each triangle) on the α-phase (a). They are not fully connected in a zig-zag shape, but instead, they form a 3-fold symmetry with a displacement of ½ from the predicted Liebig's melon structure. Another phase coexists in the same image, here named β-phase. As shown in the 3D image (b) and in the extracted profile (c), this new β-phase is located at a higher surface than the pCN patterns. The scale indicates that the metal step edge of Cu(111) is 208 pm, which points out that some molecules are in the lower terrace (also seen by the patterns). It seems that the polymer molecule is covalently binding with a surface copper atom and somehow "pulling" it out of the surface, forming a hybrid copper-polymer. One hypothesis is that, at higher temperatures, the amino groups at the end of the melon molecule start to dehydrogenate, forming strong N-Cu bonds, sort of like a metal-organic covalent bonding. The organic molecule pulls the copper adatom up to get the

most stable hybrid bonding, and, most probably, this process is starting by the edges due to the opened terminations. It is also much easier to pull or take copper adatoms from a step edge than from the closed surface. When Cu surfaces are submitted to elevated temperatures, the detachment of Cu atoms occurs from atomic step edges, resulting in adatoms around this area[126].

Figure 4- 5 shows constant-height Δf (frequency-shift) and current small-scaled images of a region from the α-phase. The frequency-shift images allow the submolecular investigation of the pCN structure. On the right side of the first image, it is possible to see condensed 3-s-triazines in a structure similar to what is known as graphitic carbon nitride. However, the g-C_3N_4 structure repetition does not go far. Most of the polymer chains are arranged into two different "melon-kind" structures, aligned like ribbons, each stabilized with a strong hydrogen-bonding pattern, separated by half displaced heptazines. The hydrogen-bonding patterns were name α-phase (1) and α-phase (2), and the correspondent molecules are depicted in Figure 4- 6.

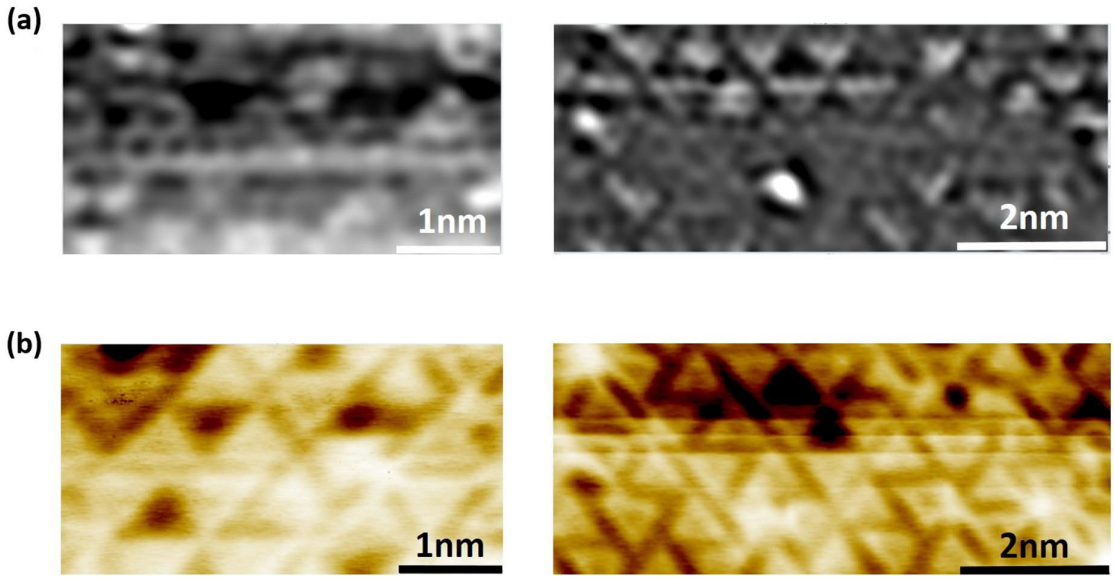

Figure 4- 5: *In situ* constant-height nc-AFM images in a) frequency-shift and b) current modes, with three visible molecules (g-C_3N_4 and melon with two different hydrogen bonding patterns), where each triangle is a heptazine.

The configurations of the α and β phases were also observed by Lin et al.[123] during an *in situ* STM self-assembling of a melamine monolayer on Cu(111). The authors have first deposited

melamine at room temperature. With annealing temperatures up to 150ºC, only the β-phase was imaged. In contrast, further annealing up to 200ºC resulted in the initial formation of a completely new phase transition (here named α-phase), which was partially transitioned at 300ºC. After XPS experiments, resulting in a nitrogen-to-carbon ratio of 2, the α-phase was not attributed to melon-like structures but to polyguanide chains, which we are not in agreement with. A consistency between the periodicity of the Cu(111) and the dimension of the α-phase was also mentioned in their work, indicating a strong geometric dependence of the polymerization process on the Cu(111) substrate.

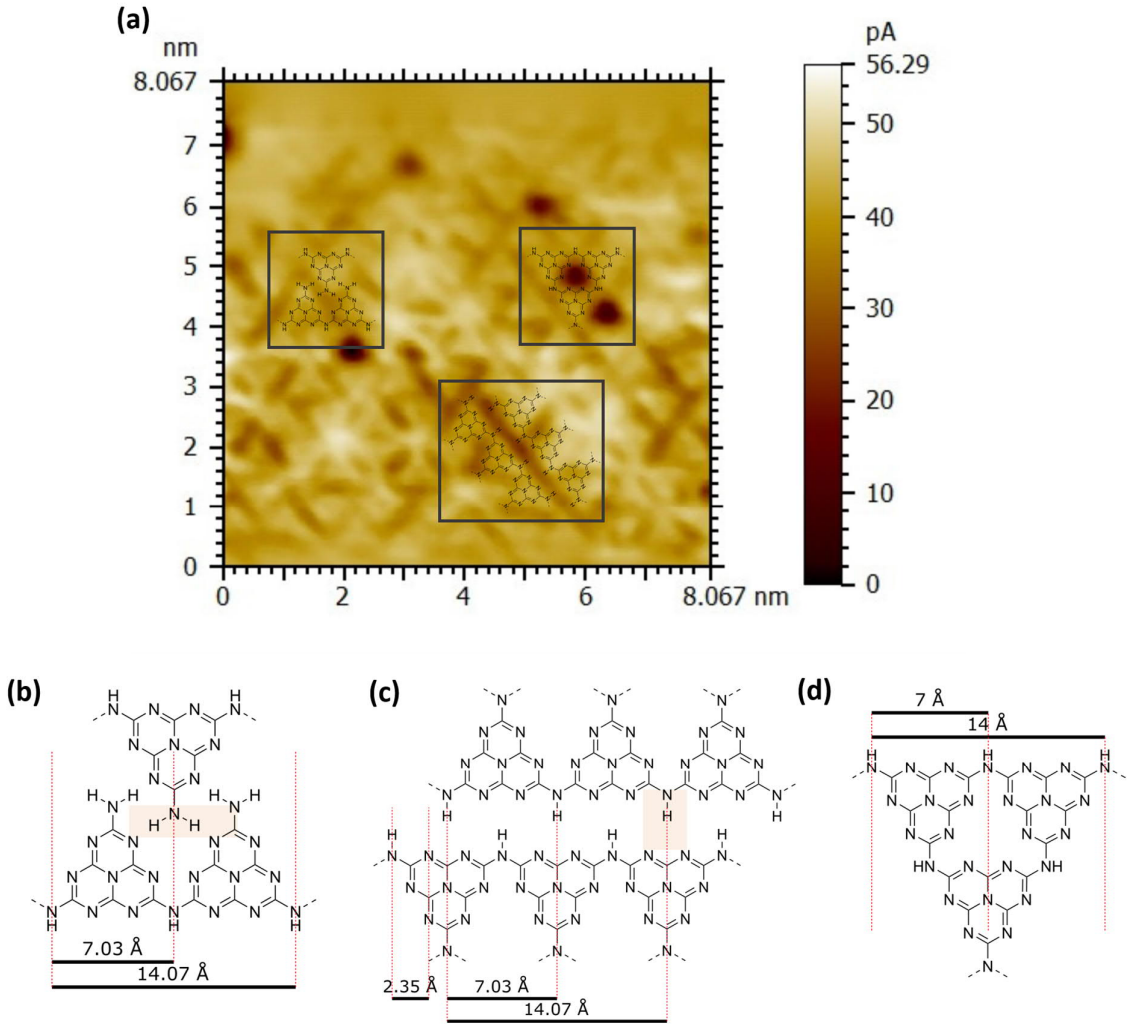

Figure 4- 6: Matching overlay of the three phases of pCN on a) *In situ* constant-height nc-AFM image, and the correspondent extracted molecules with their respective calculated distances b) melon-like α-phase (1), c) melon-like α-phase (2), and c) g-C_3N_4.

In this work, density functional theory (DFT) calculations were carried out to understand why different bonding patterns and ½ displacements appear more frequently than the previously reported phases in the literature, mainly g-C_3N_4. Those calculations were made in collaboration with Julian Heske and Prof. Dr. Thomas Kühne from the Dynamics of Condensed Matter (DCM) group at the University of Paderborn.

To investigate the orientation and interaction of heptazine units of the displaced units of the α-phase on Cu (111), structures of two melem-based dimers were considered a model. While the condensation of these carbon nitrides leads to polymers that are usually connected through amino groups in the corners of the heptazine units, the dimers are oriented so that their edges face each other. The impact of the displacement of the heptazine units was studied by varying the dimers' position relative to each other, and the atomic structure was optimized using DFT-based calculations. According to the findings, there is no indication of covalent bond formation in the mentioned positions. Having covalent bonds between the terminal nitrogen atoms of the tri-s-triazine units is highly energetically disfavored. The possible planar dimers structures and their respective relative energies are shown in Figure 4- 7.

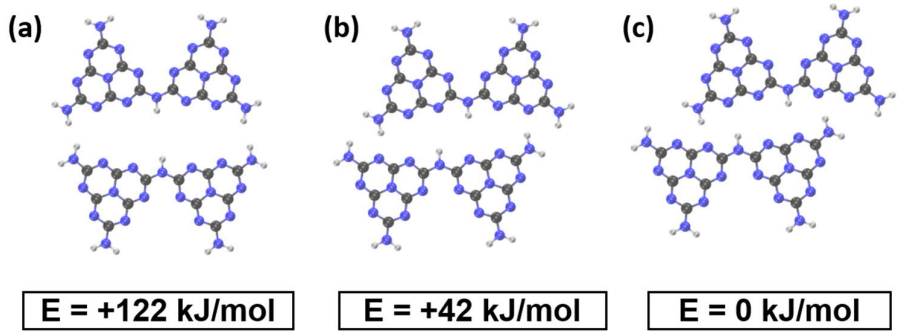

Figure 4- 7: Structures and energies of melem-based dimers with different relative orientations (C in grey, N in blue).

The first melem-based dimer structure (a) has the highest energy and is the least stable one. This finding can be interpreted as a result of the intermolecular repulsion of the hydrogen atoms. The two other dimer structures, (b) and (c), bond with different molecules through hydrogen-bonding with nitrogen atoms and have lower energy. With this, we can say that the ½ displacement of heptazine in the α-phase results from the hydrogen bonds formed towards

each other, following the previous statement that in this part of the structure, there are no covalent bonds.

As already discussed, in the α-phase obtained by *in situ* STM/nc-AFM, there is a mixture of different local occurring structures with the displaced heptazines units polymerized in a "melon-like" arrangement and some few fully condensed graphitic spots. Cohesive energy values can reveal which structure is more thermodynamically favorable. Therefore, the cohesive energies were calculated for each studied polymeric structure: melem, melem-based displaced dimers, Liebig's melon, g-C_3N_4, and the two hydrogen-bonding patterns found in the α-phase with the ½ displaced heptazines (Figure 4- 8). The calculations agree with the literature trend that the molecules' cohesive energy increases with the polymerization degree[12]. However, the fully condensed g-C_3N_4, which has the lowest cohesive energy and, hence, is the most thermodynamically favorable structure, was not achieved, neither was a pure 2D Liebig's melon.

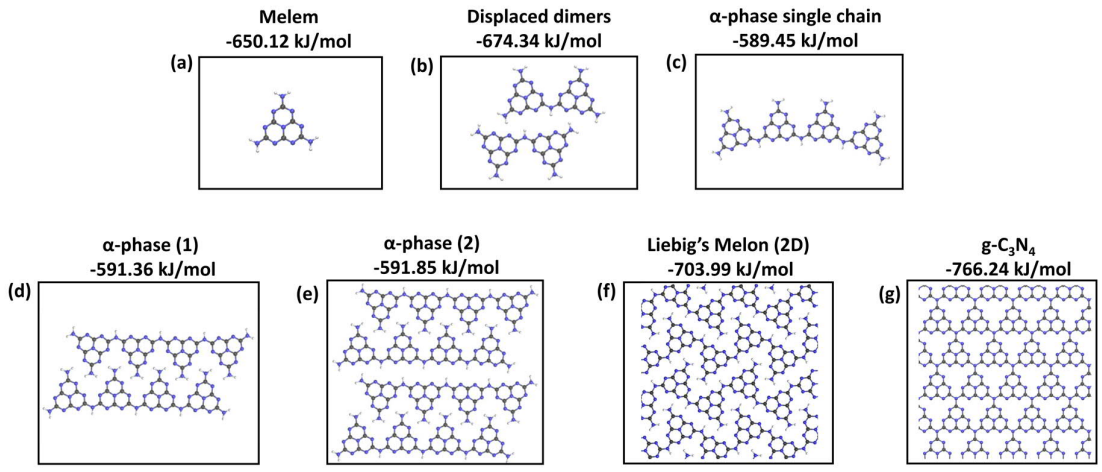

Figure 4- 8: Calculated cohesive energies correspondent to a) melem, b) melem-based displacement dimers, c) alpha-phase single chain, d) alpha-phase hydrogen bonding pattern (1), e) alpha-phase hydrogen-bonding pattern (2), f) Liebig's melon and (g) graphitic carbon nitride.

A combination of the STM/nc-AFM images and DFT calculations have shown that there are much more of the α-phase arrangements, which have higher cohesive energy than the graphitic carbon nitride and Liebig's melon structures. This situation is commonly seen in reactions that are under *kinetic* control. It means that g-C_3N_4 is the most stable *thermodynamic* product.

However, the *kinetic* products (the ones associated with the lowest energy barrier to their formation) are easier to form – in this case, the α-phase structures. In short, monomers and low molecular weight oligomers with the here-found orientations are still likely due to the energy barriers and an incomplete condensation process. Because of the very high cohesive energy (-541.69 kJ/mol), 1D periodic structures of the alpha-phase tend to undergo structural deformation, whereas isolated structures are perfectly plane. That is why the formation of long polymer chains is not likely to happen according to both theoretical and experimental results presented in this thesis. Additionally, the structures can interact locally with the different adatoms in the copper surface plane, resulting in different polymer chain orientations.

To gain more insight into the surface structure dimensions and compare them with the theoretically predicted molecule, the constant-height nc-AFM (current) was used (Figure 4-9). The 2D Fast Fourier Transform (FFT) spectral analysis of a plane view of the same α-phase region reveals lattice spacings of 0.32 nm, 0.54 nm, 0.62 nm, 0.79 nm. These values are in excellent agreement with the direct dimension measurements from the nc-AFM image and DFT calculations (Appendix, Figure A-13). Nevertheless, due to defects and different hydrogen bonding patterns, there are some small plane distance variations. As already reported in the literature, a material composed of tri-s-triazine units should have a six or threefold symmetry with distances of roughly 0.72 nm[12].

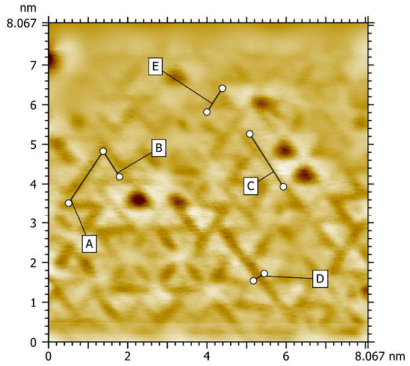

Distances	Unit	A	B	C	D	E
HDist	nm	1.574	0.7650	1.581	0.3315	0.7139

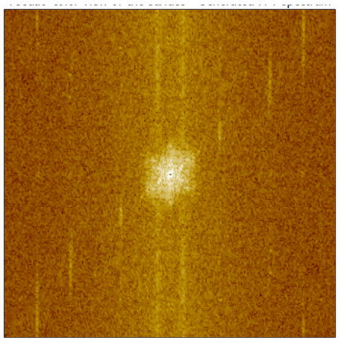

Figure 4- 9: Constant-height dF nc-AFM image of pCN and its direct image dimensions measurements on the left with the corresponding FFT on the right.

To investigate potential catalytic effects and local interactions with adatoms within the copper substrate and understand how the pCN structure would behave at higher temperatures, the highest power supply of the STM/nc-AFM system was employed. The reaction product was obtained at a temperature higher than 600 ºC. Low-temperature STM pictures were taken while heating the substrate from the temperature used at Step 2 up to the maximum range. As an intermediated product, a new phase was added to the polymer structure, the ɣ-phase, pointed out in Figure 4- 10(a). Although the brightest structure on the right side of the image was denoted as this new phase, it looks pretty similar to the α-phase, but in a higher terrace. About the β-phase, it can be that some adatoms of copper are being incorporated into the α-phase forming it, as explained previously. However, another explanation would be that passivation occurs due to molecular fragments, which appear darker in the image. The brighter spots both on (a) and (b) images are probably due to different positioning of the atoms, which could enhance the signal of the measurement depending on how it stands on the surface[127].

Upon further heating, another new phase starts to be constructed. Here named δ-phase, it is shown in details in the image (b). Interestingly, its 3D corresponding image shows it has a much higher step than the phases before. The difference in height and possibly orientation can be attributed to the fact that neighboring polymers are able to stabilize each other. Polymeric carbon nitride is known to start decomposing at temperatures higher than 600ºC, being completely gone at 700ºC due to highly reactive carbon and nitrogen fragments[12]. It decomposes due to thermally initiated dehydrogenation and can form a copper-organic hybrid, mainly at the edges because of the amino terminal groups and adatoms, resulting in a surface-directed alignment of the chains, most probably due to the reconstruction of the Cu (111) surface. The measured periodic distance between each spheroid in these linear molecular chains is about 0.37 nm, and the angle formed between the vertical alignment end the “right leg” is around 129.1º.

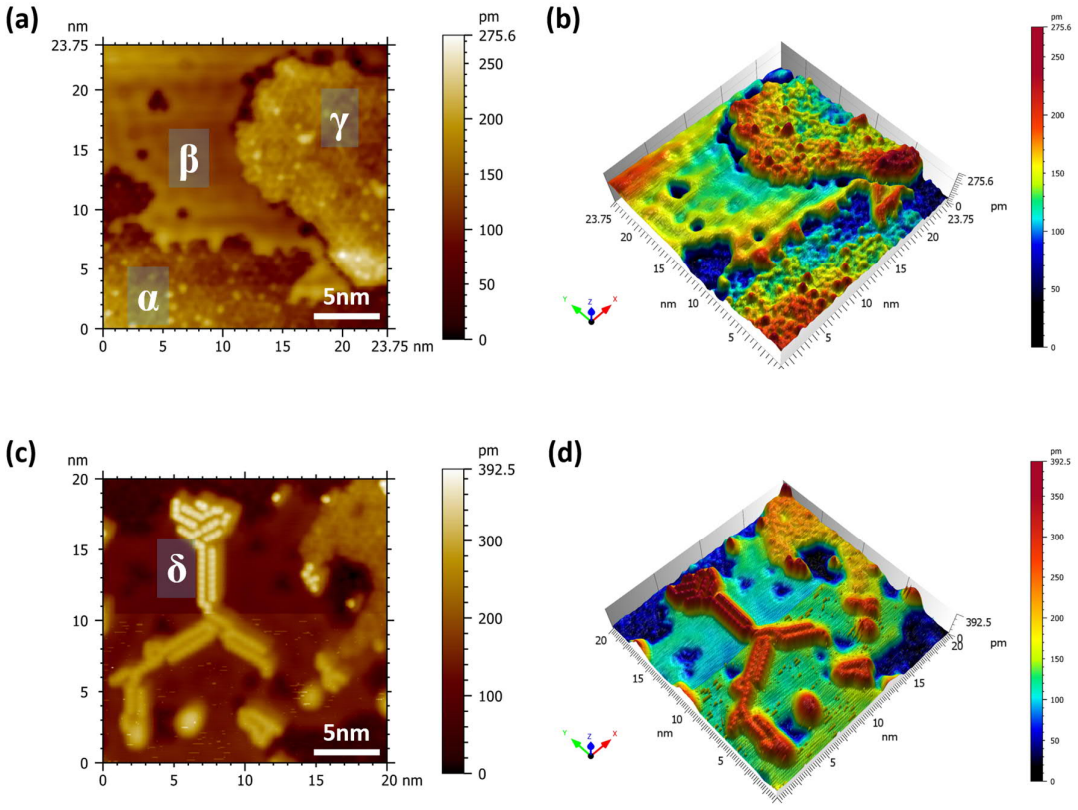

Figure 4- 10: *In situ* STM during the last polymerization process (α and β phases) with the substrate heating up to the maximum temperature. a) STM image of α, β, and ɣ- phases with its b) 3D image, c) δ-phase constant height image and its b) 3D image.

When the copper substrate achieved the highest temperature possible within the SPM setup, preferential adsorption of the polymer occurred, forming long-range alignment chains of the δ-phase, as shown in Figure 4- 11, in a similar geometry as that on Cu(111) surfaces. Furthermore, the distances extracted from the FFT spectrum are equal to 0.77 nm and 1.2 nm.

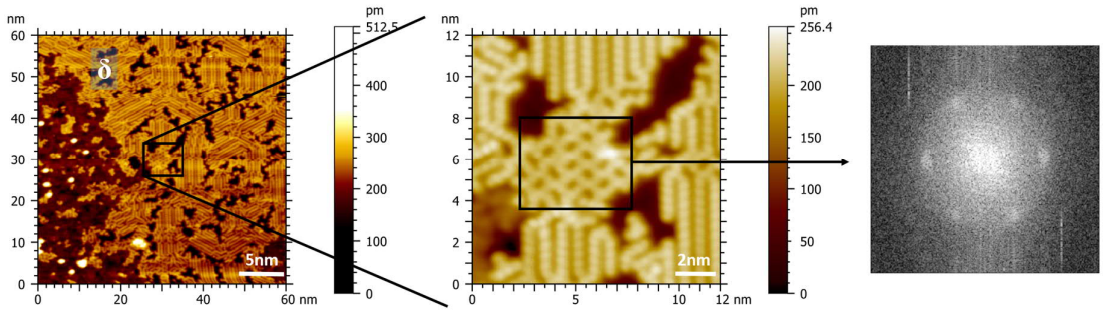

Figure 4- 11: *In situ* nc-AFM of the δ-phase during the last polymerization step with the substrate already at the maximum temperature (> 600 °C) and its correspondent FFT.

XPS spectra results of the *in situ* polymeric thin film sample at the last stage (Appendix, Figure A-14 and Table A-8) have shown a weak signal of oxygen contamination, resulting from a partially oxidized copper surface during the substrate manipulation. The deconvolution of the N1s spectrum resulted in two distinct and intense peaks and a much weaker signal. The first one is located at 397.61 eV and can be attributed to the formation of copper-nitrides due to complete dehydrogenation of the amino groups on the terminations of the carbon nitride structure [128,129]. If all the terminal groups of the organic molecules form N-Cu bonds, the hybrid metal-organic molecules tend to be flat-oriented. The second peak at 399 eV is slightly weaker and corresponds to pyridinic-N. These two main peaks found from the N1s spectrum have a nearly equal peak area, meaning a similar amount of both bonding states and consistency with the nitrogen types in the melamine molecule[130]. The much weaker signal at 400.41 eV corresponds to $N\text{-}(C)_3$ bonds. The deconvoluted C1s spectrum counterpart revealed a weak peak at 285 eV, assigned to C-C bonds, a second strong peak at 287.5 eV, attributed to N-C=N bonds, and a weaker signal at 288.4 eV, which can be due to contaminations from the copper substrate. The C/N ratio calculated from the percentages of the bonding states is equal to 0.49.

Additional DFT studies were made to determine how the organic molecules preferentially orient on the copper surface from the first step of the deposition process. When deposition of organic polymers occurs in non-metallic substrates where there is no significant interaction between the organic molecules and the substrate, the molecules usually are preferentially oriented upright standing on the substrate. That happens because the molecules try to maximize the overlap of their π systems among themselves. On the other hand, when the deposition occurs on metallic

substrates such as copper, there is a higher interaction with the organic molecules, and they try to maximize this overlapping by flat-orienting on the surface. It is essential to consider that there is also an intermediate state and that every time the molecules meet with step edges, a complex change in orientation by twisting, rotating, and bending can also occur. The flat-oriented result of the adsorbed organic polymer molecules on Cu (111) found on our DFT calculations is shown in the Appendix (Figure A-15). A high energy of -174.7 kJ/mol is released during the adsorption of the molecules, which is an indication of the strong interaction between the copper surface and melamine molecules.

4.2 Conclusions

In summary, surface-supported polymerization of melamine molecules on a reconstructed Cu (111) has been investigated by low-temperature STM/nc-AFM, with a metallic probe tip passivated with an unknown molecule, in UHV environment. The submolecular STM/nc-AFM images taken throughout different polymerization experiments have shown in detail the formation of different phases, including the highest degree of condensation of polymeric carbon nitride thin films, here named α-phase. In addition to the *in situ* measurements with the microscopy setup, DFT calculations have revealed that a long-range polymer chain was unlikely to be formed due to local effects. Moreover, the pCN phase was attributed to "melon-like" structures with ½ displacement between the linked heptazines with a complex hydrogen-bonding pattern. Upon further heating at temperatures higher than 600 ^{o}C an unknown structure was formed. XPS spectra have confirmed the literature's statements that over 600 ^{o}C, pCN starts to decompose, losing hydrogen from terminal amino groups. As a consequence, the reminiscent nitrogen bond with copper atoms to form a metal-organic hybrid. The results provide a controlled growth of different polymer phases and alignment of the molecular chains on the copper single crystal surface.

Chapter 5

Polymeric carbon nitride-based photonic devices

Over the last decades, photonic integrated circuits (PICs) have experienced a massive development. Analogous to well-known miniaturized integrated electronic circuits (ICs), the integration of various optical elements on a single chip is a crucial parameter for developing optimal telecom, Datacom, and sensing devices. In order to achieve a compact integration of photonic circuits, high-refractive index wavelength-scale structures are a crucial requirement. PICs combine many features on a single chip, such as wavelength filtering, modulation, and photodetection. These systems increasingly rely on advanced materials with extremely specific requirements on materials properties. Nowadays, most commercial PICs are based on silicon photonics since it is the only technology that allows the high-density integration of optical components due to the high-refractive-index contrast of silicon-on-insulator (SOI) waveguides and the compatibility with the complementary metal-oxide-semiconductor (CMOS) process technology[131–134]. However, compared to currently inorganic materials employed in the PICs industry, and due to intrinsic properties, polymer-based integrated photonic devices are inexpensive to fabricate, compatible with established processing methods, and flexible to meet a broad range of applications such as telecom on-chip optical communications and signal processing.

In the previous chapters, the structure and the high refractive index of polymeric carbon nitride thin films in the in-plane and out-of-plane were deeply investigated. Based on the ellipsometry spectroscopy data, pCN thin films deposited by low-pressure chemical vapor deposition under different conditions have revealed a n_o of above 2 to 1.9703 nm from the visible to the near-infrared range in every sample, in addition to having high-transparency (transmittance >80%) at 1550 nm. Moreover, pCN thin films are mechanically flexible and thermostable up to ≈ 600ºC. These properties make pCN thin films highly attractive for waveguide core components in integrated optical systems.

Generally speaking, a high level of integration in photonic devices requires the core material to have a considerable high refractive index to allow light to be confined in the material effectively by total internal reflection (TIR). Furthermore, the higher the refractive index, the smaller the integrated optical components such as waveguides and optical resonators. For reference, the refractive index values reported for most polymers in the visible and NIR range are about 1.3 to 1.7[135–137]. At the same frequency range, pCN has its value from around 2 to 1.9703, the highest ever reported for optically transparent polymers, thus turning polymeric carbon nitride thin films into one of the most attractive polymeric material for integrated optical systems.

In this chapter, the optical properties of high ordinary refractive index pCN thin films are explored in order to implement photonic devices operating at near-infrared optical frequencies (λ=1.5 μm). The fabrication procedure and optical dispersion properties of the pCN thin films are described in Sessions 5.1 and 5.2, respectively, followed by the simulation and fabrication of the polymeric carbon nitride-based photonic devices presented in Session 5.3. The optical performance of the devices was experimentally characterized and is described in Session 5.4.

The fabrication and characterization of the photonic devices were made in collaboration with Corinna Kaspar and Prof. Dr. Wolfram Pernice from the Responsive Nanosystems group at the Physics Institute/CeNTech, University of Münster.

5.1 Thin film deposition

A low-pressure chemical deposition system was used to grow amorphous polymeric carbon nitride thin films from melamine powder, under N_2 flow, on 2 µm thermal oxide/ 380 µm Si wafers. Details about the LPCVD setup and deposition mechanism were previously discussed in Chapter 3. The polymerization time and amount of melamine used were reoptimized from the systematic investigation presented in this thesis, considering the parameters employed when achieving samples with lower roughness and increased thickness. As previously mentioned in this thesis, the pCN thin films must have a minimum thickness of around 300-400 nm for effective light coupling and guiding in the telecom regime.

The steps of the optimized deposition process are shown in Table 10. A quartz boat with 40g of melamine was positioned in the center of the upstream oven, while the substrates were located at the end of the downstream furnace. For this recipe, not only the polymerization time was increased, but also the ramp time to heat up and cool down both furnaces. These last parameters were increased to reduce the thermal stress due to the use of a SiO_2 thickness on top of the silicon wafer. In the systematic investigation presented in Chapter 3, we have used a silicon wafer with a 2 nm natural oxide layer on top. However, to avoid propagation losses, i.e., light losses from the waveguides to the higher refractive index substrate, a thermal oxide layer of at least 2 µm has to be used between the silicon and the deposited thin film to isolate the circuit from the wafer optically. Silicon has a much higher refractive index than the pCN thin film, and a native 2 nm oxide layer is not enough to prevent the modes from leaking to the substrate instead of being guided in the polymer.

Table 10: CVD parameters for the deposition of pCN thin films to be used in integrated optical devices.

pCN 40g	Step 1	Step 2	Step 3	Step 4	Step 5	Step 6
Upstream (ºC)	0	0	300	300	0	0
Downstream (ºC)	0	550	550	550	550	0
Heater time (min)	10	40	60	200	40	2
N_2 gas set (SCCM)	500	50	50	50	50	0
Pressure set (Torr)	10	10	10	10	10	10

Organic polymers present a significant drawback regarding their applicability in photonic devices – propagation losses. Wave attenuation effects ,i.e., losses in light intensity and amplitude, are generally associated with intrinsic (when they originate from the basic properties of the material) and extrinsic (impurities or resulting from the fabrication process) losses such as electronic transition absorption, vibrational absorption, Rayleigh scattering, impurities, and inhomogeneity[138]. For guiding light at telecom wavelengths on a chip, it is imperative to use materials that allow low absorption and scattering to achieve low-loss light confinement. As for the losses by strong scattering effects, the major lossy source is the sidewall roughness, either coming from the thin film deposition process or being a residual roughness from the etching process[139–143]. In order to track the surface roughness from the as-deposited thin films, the surface topography was investigated using atomic force microscopy.

Figure 5- 1 shows the root mean square (RMS) area roughness of different pCN thin films deposited on the 2 µm thick thermal oxide on a silicon wafer (a and b) as well as on a fused silica wafer (c). The as-deposited film features the highest roughness with S_q=2.4 nm. It was possible to reduce this value to S_q=1.6 nm by optimizing the procedure with an additional plasma treatment of the SiO_2/Si wafer. All the substrates were first cleaned with acetone and then isopropanol (IPA) for 30 minutes each in an ultrasonic bath, followed by drying with N_2. The additional plasma cleaning step was made by treating the thin films with a mixture of Ar and O_2 (70:30 SCCM) for 2 minutes at 60 W and a pulsing duty ratio of 255. Remarkably, the RMS area roughness of the pCN thin film deposited on the fused silica wafer has the lowest value with S_q=1.0 nm. This might be due to the much lower thermal expansion coefficient of the fused silica compared to the silicon wafer (fused silica has 1/5 of the thermal expansion coefficient of Si), meaning it is extremely thermal shock resistant[144,145]. The mismatch between the thermal coefficients of SiO_2 and Si can result in a higher thermal stress and structure modification when using the 2 µm thick thermal oxide on a silicon wafer at 550°C during the CVD process. The same would not occur with the fused silica substrate. Moreover, there is an evident change in the morphology when using the fused silica substrate, with considerably smaller grains, attributed to different nucleation densities compared to the thermal oxide silicon wafer.

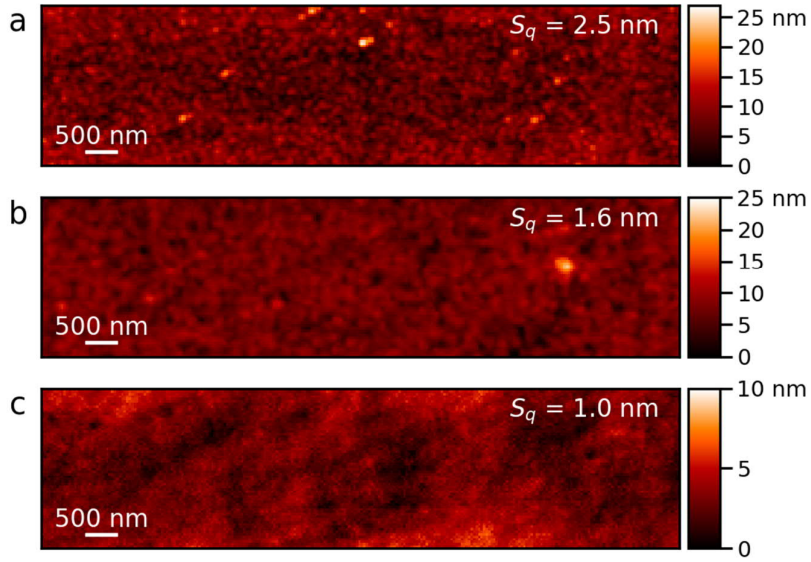

Figure 5- 1: Atomic force microscopy images of CVD polymeric carbon nitride surfaces. RMS area roughness for the pCN thin film deposited a) on a 2 µm thick, polished thermal oxide layer on a silicon wafer, b) on the same substrate submitted to plasma treatment, and c) on a polished fused silica wafer.

5.2 Optical dispersion properties

The optical dispersion properties of the pCN thin films were characterized by generalized ellipsometry using a J.A. Woollam M-2000 system. The samples were measured from 370 to 1670 nm with incidence angles from 55° to 75° in steps of 5°. For all the incidence angles, the beam spot was much smaller than the sample. The fitting model was created considering the pCN thin films to have anisotropic optical properties. Explanations about the anisotropy of the organic polymeric thin films were given in Chapter 3. The 2 µm thermal oxide layer of the wafer was fitted using a Sellmeier dispersion formula. For the transparent part of the pCN thin film, a Cauchy model was applied, and for the absorption range, Gen-Osc (general oscillators) were used. The function parameters are described in the Appendix (Figure A-16).

Measurements were taken with the focus probe at different spots from the same sample, and the fit was performed using multisample analysis, e.g., the optical constants were coupled together for various spots of the same sample (thicknesses were not coupled between focus spots). Multisample analysis is a simplified assumption that analyzes different data sets

simultaneously to extract the different layer thicknesses and fit the average optical constants over various samples. However, this is not useful for pCN thin films when coupling different samples since they show variations in the optical dispersion behavior compared to each other. Regardless, such analysis can help to reduce the parameter correlation when measuring different spots of the same sample.

The polymeric carbon nitride thin film with a reduced roughness, resulting from the pre-plasma treatment of the SiO_2/Si wafer (Figure 5- 1b), was chosen as the optimal dielectric thin film to fabricate the waveguides. Although the films deposited on fused silica have presented a much lower roughness, using insulator wafers is much more complicated during the nanopatterning step with EBL due to charging effects from the electron beam, which induces severe pattern distortion[146–148]. Multisample analysis results for the low-roughness pCN thin film, here named TC-1, are shown in Figure 5- 2. The extracted enlarged area from the extinction coefficient curves shows that k_o is always higher than k_e throughout the operating wavelength range, indicating anisotropic behavior, in good agreement with the previous results in this thesis, indicating a higher absorption from the whole visible to NIR range along the preferential orientation of the polymer backbone in the in-plane.

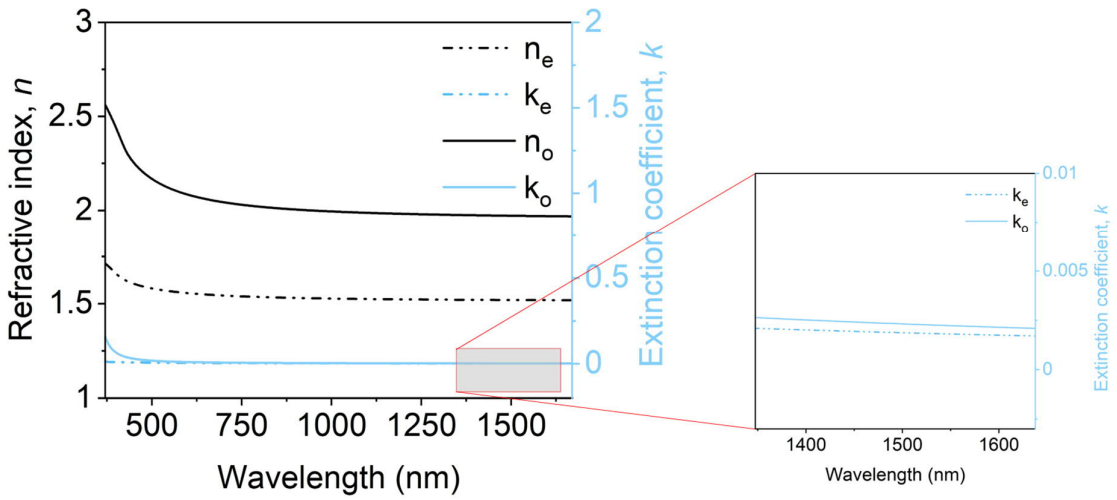

Figure 5- 2: Optical dispersion parameters in the in-plane (n_o, k_o) and out-of-plane (n_e, k_e) of sample TC-1 (40g of melamine polymerized on a 2 µm thermal oxide/ 380 µm Si wafer).

The values of ordinary and extraordinary refractive indices and extinction coefficients at the photonic device working wavelength (1550 nm) are presented in Table 11. Thicknesses values fitted for the different measured focus spots using multisample analysis, coupling the optical properties of Figure 5- 2 were 389.98 nm, 374.80 nm, 340.62 nm, and 382.15 nm.

The ordinary refractive index value at the optical wavelength 1550 nm (sometimes called C-band) is 1.9703, considered a high-refractive index for transparent polymers. Such values could only be achieved, to the best of our knowledge, by incorporating functional groups into the polymer or synthesizing hybrid materials such as organometallic polymers[149,150]. A waveguide core element material with such a high refractive index enables a compact design and good mode confinement within the waveguide channel. The successful performance of optical dielectric waveguides is directly related to the difference in the refractive index between the core material and the cladding (surrounding media). This difference in the refractive index is called 'index contrast' and is represented by Δn[151]. Higher index contrast values allow for a large integration scale and feasibility of more complex circuits as, for example, ring resonators.

Table 11: Refractive index (n_o and n_e) and extinction coefficients (k_o and k_e) extracted from the ellipsometry optical dispersion results at the waveguide working wavelength (1550 nm).

Waveguides sample (TC-1)	@1550 nm
n_o	1.9703
n_e	1.5191
k_o	0.0022
k_e	0.0018

5.3 Simulation and fabrication of photonic devices

As previously mentioned in Chapter 2, a waveguide is composed of a region of higher refractive index (core) compared to its surroundings (cladding). The most often used waveguide geometries in integrated optics are planar waveguides, which provide confinement of the optical fields in only one direction, and rectangular waveguides, which allow for the integration of more complex circuits by optical confinement in two directions. Rectangular waveguides work analogously to metallic stripes in an electrical integrated circuit. The basic rectangular waveguide structure consists of a higher index strip region (in our case, pCN) and confinement media surroundings all around it with a lesser refractive index (air and fused silica or thermal oxide on silicon). When the surrounding materials are different, for example, when the upper cladding is air, and the bottom one is a substrate with a refractive index different from that of air, the waveguide is considered asymmetrical[152]. Our stacking on the SiO_2/Si and also on fused silica wafers makes an asymmetrical system, as depicted in Figure 5- 3.

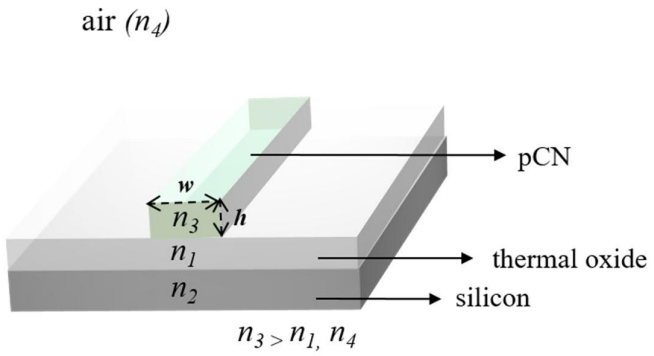

Figure 5- 3: Schematic of a polymeric carbon nitride-based strip waveguide on a SiO_2/Si substrate considering its refractive index (core) and the surroundings (cladding).

According to the Snell's Law of refraction, when having incidence angles greater than the critical angle, total internal reflection (TIR) occurs, and light is guided along the *z*-direction (parallel to the film surface). Furthermore, the analysis of the electromagnetic wave propagated in the waveguide can be made using Maxwell's equations. These equations result in eigenvalues, which are the different modes that the material can propagate based on its patterned geometry and optical parameters at specific working wavelengths. Strip waveguides support two-dimensional fields as transverse electric (*TE*) and transverse magnetic (*TM*) modes.

Depending on the transmission mode, the axis of oscillation in electromagnetic transmission may have different orientations to the direction of travel. In the TE mode, the electric vector ***E*** has no component in the direction of propagation, meaning the electromagnetic field is transverse to the direction of propagation. On the other hand, in the TM mode, the magnetic vector ***H*** is transverse to the direction of propagation, having no component in the mentioned direction[153]. The theory behind both modes was already explored in Session 2.2.1.

A numerical mode analysis based on the Finite Element Method (FEM) for the optical wavelength of 1550 nm was carried out based on the optical dispersion results for pCN obtained by spectroscopy ellipsometry. The FEM is widely used for the analysis of the surface modes propagating along a dielectric waveguide. It solves boundary-value problems, e.g., problems given in a partial differential equation for a specific domain, by discretizing the domain into small elements and approximating the field solution within each element. In this work, the primary purpose of performing numerical simulations using the FEM was to obtain insights into the performance of the polymer-based waveguide with varying geometrical parameters (width) whilst keeping only a single guided mode per polarization direction (single-mode condition)[154].

The model considered a 310 nm high carbon nitride strip waveguide on a fused silica substrate ($n_{1550\ nm}$ = 1.4451) and air cladding (n=1.0). The ordinary refractive index of the polymeric carbon nitride was chosen to be oriented in the waveguide plane (x-z-plane). The extraordinary index was set perpendicular to the substrate, pointing along the y-direction. Figure 5- 4 shows the normalized electric field distribution of the fundamental TE-like mode (n_{eff}=1.6262) and the weakly guided second TE-like mode (n_{eff}=1.4474) of a 1.6 µm wide waveguide. In optical waveguides, the term "effective refractive index", represented by n_{eff}, corresponds to the measure of the overall delay of the light beam propagating in the waveguide. It is a key parameter in guided propagation since it depends not only on the wavelength but also on the mode in which the light propagates and the whole waveguide design.

Further, in the numerical investigations, no TM-like mode was guided for the considered geometry due to the low index contrast between the extraordinary index of the pCN thin films and the fused silica substrate, which amounts to only 0.0698. This small difference in the

refractive index makes the mode leak into the substrate instead of being guided in the pCN. For a single-mode waveguide, the width was reduced to 1.55 µm.

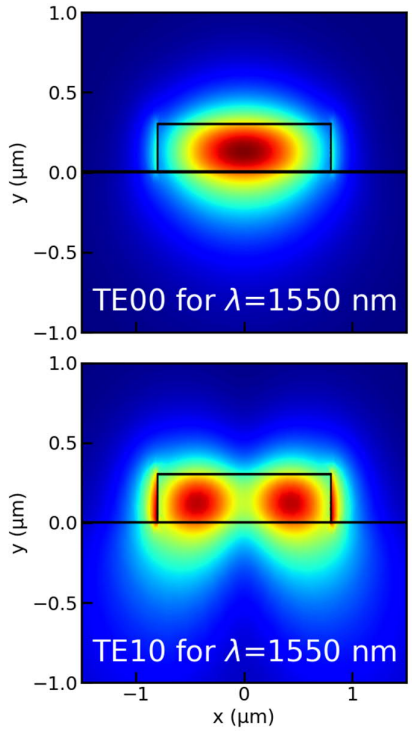

Figure 5- 4: Simulated electrical field of waveguide modes for a wavelength of 1550 nm, a 310 nm high, and 1.6 µm wide carbon nitride waveguide on fused silica and air cladding supports the fundamental TE_{00} mode and the TE_{10} as a weak second mode.

The polymeric carbon nitride-based photonic devices were fabricated using EBL and a subsequent dry etching process. For this, AR-P 672.045 (PMMA positive E-beam resist) with a thickness of about 350 nm was spin-coated on the cleaned samples and exposed with a 100 kV Raith EBPG5150 system. PMMA was chosen as the resist because other types of resists mainly require a wet etching step with a developer based on water. When carbon nitride thin films enter into contact with water, the film starts to peel off the substrate easily. The peeling-off process time varies depending on the energy matching with the substrate. Still, it will always peel off eventually if just washed or soaked in water, and this is something that must be avoided in the nanofabrication process. The ease of producing free-standing pCN thin films is advantageous for substrate transfer and fabrication of flexible optical devices.

The fabrication was followed by the development and reflow of the resist. Further, the structures were transferred into the carbon nitride thin film by reactive ion etching (RIE) with a CF_4 plasma using an Oxford PlasmaPro 80 system. The residual resist was removed with acetone. All the basic steps for the EBL patterning and etching are depicted in Chapter 2, Figure 2- 7. As a proof of concept, a recipe for patterning carbon nitride thin films was also developed for a focused ion beam (FIB) system. The details about the parameters used and SEM images of the patterned thin films can be found in the Appendix (Figure A-17). Due to the much longer patterning time with the ion beam, we gave preference to the EBL process.

Another critical issue for developing highly integrated circuits is the efficient coupling of light between the submicron-patterned waveguide and an optical fiber. A large mismatch in the mode field size between both optical components can cause significant losses[155]. The system typically consists of an input grating coupler, a connecting waveguide circuit, and an output grating coupler. Then, an optical fiber connected to a tunable laser is located over the input grating and, another optical fiber connected to a photodetector is positioned over the output grating. For a better coupling optimization, the fabrication was made varying the grating period and fill factor. Here shortened FF, the fill factor is referred to as the fraction of the grating period that is filled with the grating material. Figure 5- 5 shows how those parameters were changed. The transmission spectra of the waveguides coupled to gratings with different fill factors were measured and are found in the Appendix (Figure A-18).

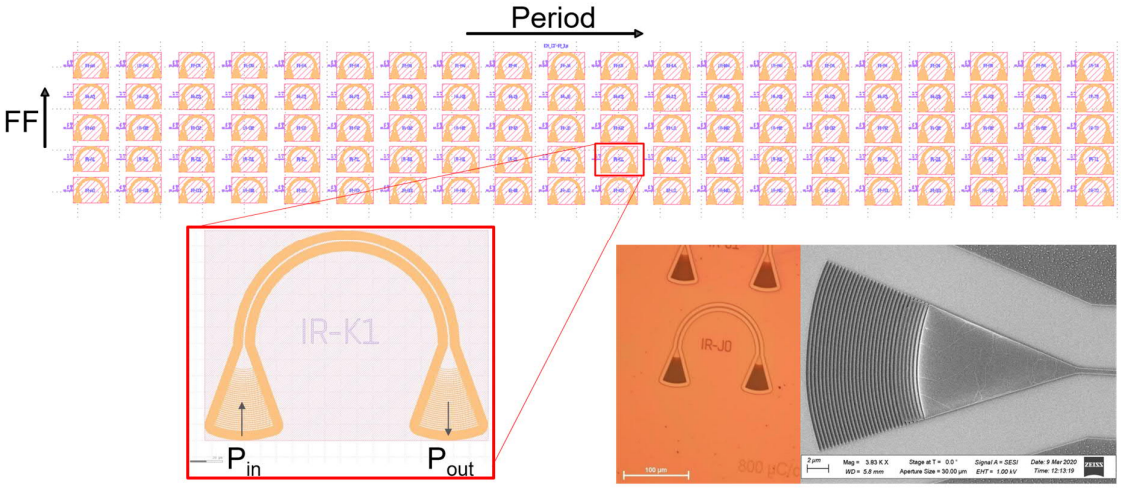

Figure 5- 5: Grating coupler optimization steps by changing the grating period and fill factor. Zoom-in region image shows how light is coupled to the gratings. P_{in} is the optical power reaching the input grating, and P_{out} is the optical power measured by the photodetector. The SEM picture shows one of the gratings structures as well as the waveguide circuit.

Proof-of-concept experiments were successfully done by experimentally characterizing the photonic device circuit with the help of microring resonators. Generally, ring resonators consist of an optical waveguide on a closed-loop. When the ring and the waveguide circuit are brought close to each other, some light from the waveguide couples to the ring, until they interfere constructively in the loop and enter in resonance. Different experiments were conducted to optimize the mirroring resonator geometry (gap and radius), as shown in Figure 5- 6. For this, quality-factor (Q-factor) were evaluated to describe the losses in the different systems, e.g., how underdamped the resonator is. The Q-factor is defined as the ratio of the initial energy stored in the resonator to the energy lost in one radian of the oscillation cycle.

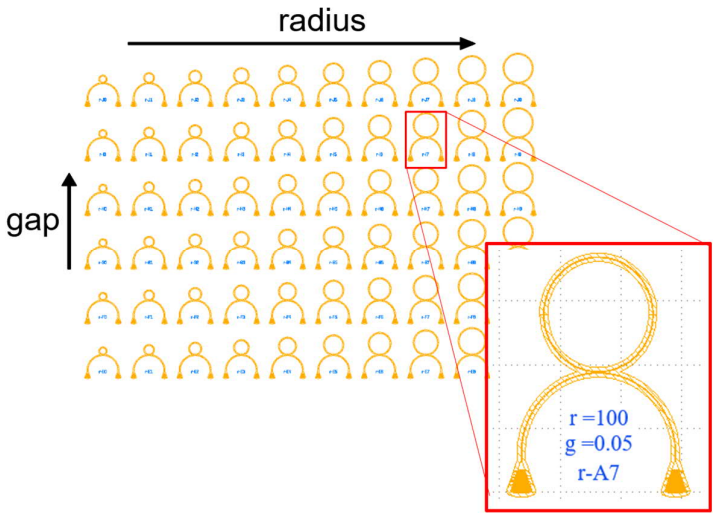

Figure 5- 6: Microring resonators optimization by changing gap size and radius of the ring.

Figure 5- 7 shows scanning electron microscope (SEM) images of the resulting optimized photonic devices. The smallest designed gap between the microring resonator and the waveguide of 50 nm could be well resolved (Figure 5- 7a). The apodized grating coupler (Figure 5- 7b) was optimized for a center wavelength of 1550 nm, having a period of 1.2 µm and a filling factor of 0.6. Figure 5- 7c shows a micrograph of a waveguide which was taken under the angle of 25°. The straight waveguide sidewall and the substrate surface draw an angle of approximately 94° (measured with the AFM), which implies a very directional etching process. The sidewall seems to be quite rough, although the upper waveguide edge is sharp. Thus, the roughness is likely not due to a rough electron beam resist but is instead induced during the dry etching or resist removal. The RMS surface roughness on top of the devices amounts to about *Sq*=7 nm. We assume that this value and the roughness of the sidewalls can be reduced by further optimizing the deposition and fabrication process.

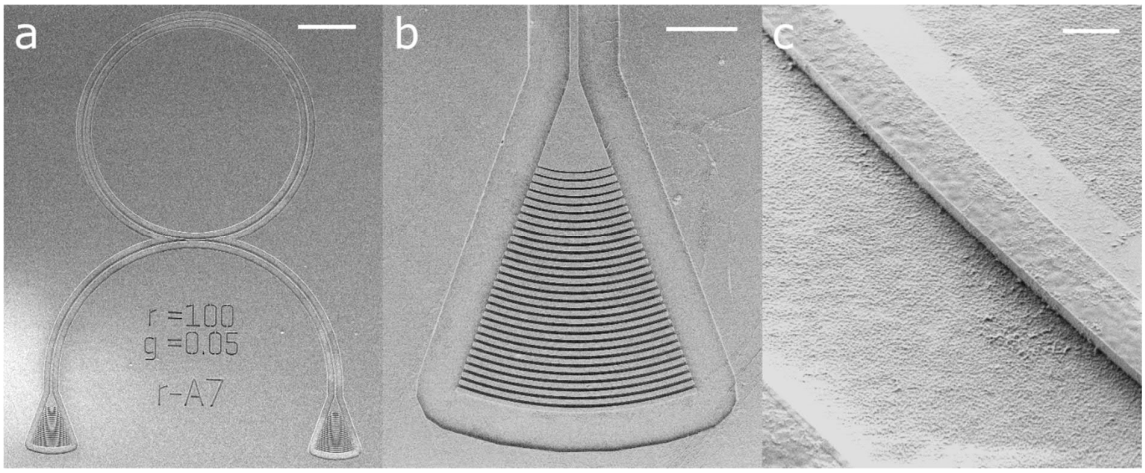

Figure 5- 7: SEM images of photonic devices etched in polymeric carbon nitride. a) microring resonator coupled to a waveguide (scale bar 50 µm). b) apodized grating coupler with a period of 1.21 µm and a filling factor of 0.6 to couple light with a center wavelength of 1550 nm into the integrated waveguide (scale bar 10 µm). c) 1.25 µm wide photonic waveguide (scale bar 1 µm).

5.4 Performance of photonic devices

Transmission measurements were carried out to study the performance of the photonic devices using a custom-build measurement setup. For this, the photonic chip is placed on a computer-controllable piezo stage. The grating couplers build the connection between the PICs and the fiber array, aligned with each other to maximize the transmitted signal. The input fiber is connected to a Santec TSL-510 tunable laser, and the polarization is adjusted with a polarization controller. A New Focus 2011 photodetector is used to detect the signal of the output fiber.

Figure 5- 8a shows the transmission spectrum of a polymeric carbon nitride-based photonic device consisting of two grating couplers connected via a semicircular waveguide with a bending radius of 63.5 µm and a width of 1.25 µm. The short waveguide losses can be neglected, resulting in a loss per coupler of approximately 10.5 dB at 1550 nm wavelength.

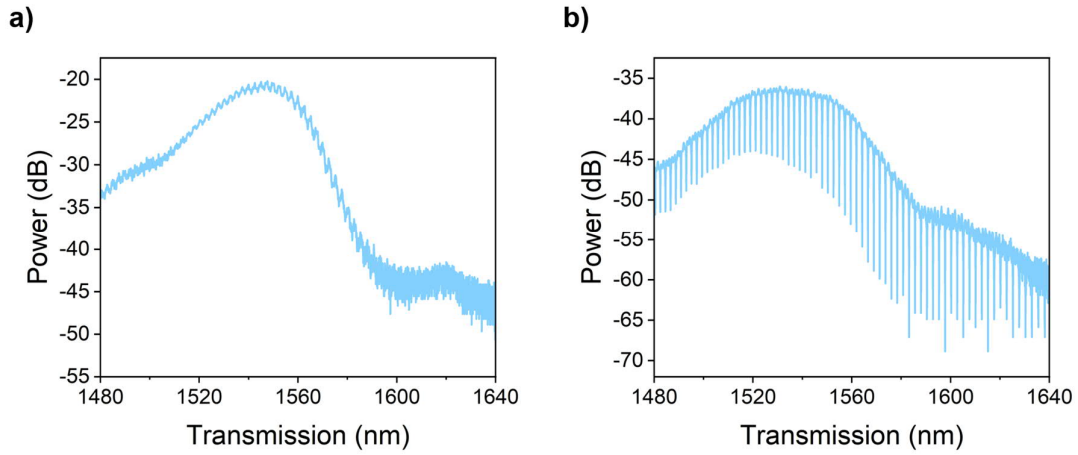

Figure 5- 8: Transmission measurement data for fabricated carbon nitride devices a) composed of two grating couplers at a distance of 127 µm connected by a semicircular waveguide. The loss per coupler is approximately 10.5 dB; b) coupled to a microring resonator (r=80 µm, g=50 nm). The highest measured Q-factor is 11721 (r=60m, g=300 nm), which corresponds to a waveguide propagation loss of about 31.32 dB/cm.

In order to determine the propagation losses of the carbon nitride waveguide, microring resonators with radii varying from 30-120 µm coupled to an input waveguide were investigated (Appendix, Figure A-19). The gap between the resonator and the waveguide was swept from 50-500 nm. A corresponding typical transmission spectrum is shown in Figure 5- 8b, where the resonant wavelengths of a 160 µm diameter ring can be clearly identified via the pronounced minima. By fitting a Lorentzian, the Q-factor can be extracted. The highest determined Q-factor was about 11721 for a ring with a radius of r=60 µm and a gap of g=300 nm. This relatively low Q-factor hints that the internal propagation losses in the microring are larger than the coupling losses. A plot of the extinction ratio as a function of the gap verified this assumption and that an even smaller gap than 50 nm would be necessary to achieve critical coupling. Thus, for a weakly coupled ring and waveguide with a gap of 300 nm, the coupling losses can be neglected, and the Q-factor is mainly limited by the internal propagation losses in the ring. The propagation losses can hence be related to the Q-factor as described in equation 5.1

$$Q \text{ via } \propto_{dB} = \frac{10}{\ln(10)} \frac{2\pi n_g}{\lambda Q} \tag{5.1}$$

where λ is the wavelength and n_g the group index. n_g can be extracted from the measured free spectral range (FSR) via the relation presented in equation 5.2 below and amounts 2.085.

$$FSR(\lambda) = \frac{\lambda^2}{n_g(\lambda)L+\lambda} \tag{5.2}$$

As a result, the propagation losses were determined to be about 31.32 dB/cm. We anticipate that this relatively high value can be improved by reducing the film deposition and fabrication process-related roughness of the surface and the sidewalls of the photonic devices. The waveguiding results show that pCN thin films are a potential replacement for inorganic materials in novel-optical devices. Furthermore, considering the measured optical properties illustrated in Figure 5- 2, the pCN thin films deposited on the chosen stacking materials also have high transparency and refractive index through the entire visible wavelength range. For future applications, pCN should also be considered in the development of well-performing photonic devices at lower wavelengths (visible range).

5.5 Conclusion

In this chapter, polymeric carbon nitride-based photonic devices for telecommunication wavelengths were developed. The high ordinary refractive index of the polymer of above 2 to 1.9703, covering the visible and near-infrared wavelength range, enables small footprint devices, strong mode confinement, and efficient coupling via grating couplers. Proof-of-concept experiments with microring resonators show a Q-factor of 11721 for a wavelength of 1550 nm, which translates into a propagation loss of approximately 31.32 dB/cm. We expect that this value can be further improved with an optimized fabrication process and that the outstanding material properties of carbon nitride will open new perspectives for polymeric photonic devices for a broad wavelength range.

Chapter 6

Thesis summary and Perspectives

The aim of the present thesis was twofold: to give more information on the composition, structure, and optical dispersion properties of chemical vapor deposited polymeric carbon nitride thin films; and to show the great potential of integrating polymeric carbon nitride thin films into optical devices.

As we have shown herein, pCN thin films have attractive optical and mechanical properties and may help to improve the flexibility and sustainability of novel-optical devices. Considering polymeric carbon nitride as the overall topic of this thesis, three different sub-themes were discussed. The first part described the influence of chemical vapor deposition conditions on the physical and chemical properties of pCN thin films, synthesized from a relatively cheap and sustainable precursor. The variation of parameters such as the precursor amount, polymerization time, and gas carrier flow rate allows changes in the real and imaginary part of the refractive index, carbon-to-nitrogen ratio, composition, structure, and morphology of the thin films. Moreover, ellipsometry results revealed a high optical uniaxial anisotropy between the in-plane (x or y, parallel to the surface) and out-of-plane (z, normal to the surface) directions, which is attributed to the molecular alignment and orientation of the thin films.

The second part of this thesis focused on revealing the mechanism of polymerization and the structure of the pCN thin films through an in situ on-surface polymerization process. Low-temperature STM/nc-AFM images were scanned using a passivated tip with an unknown molecule whilst sublimating melamine and depositing it on a hot single crystal copper surface. Interestingly, three different coexistent pCN phases were identified, and here-named g-C_3N_4, α-phase (1), and α-phase (2), according to the heptazines arrangements and hydrogen-bonding pattern. DFT calculations supported the statement in which a long-range polymer chain is unlikely to occur due to local effects. At much higher substrate temperatures than that of the pCN formation, result indicated that dehydrogenation of the amino groups gives place to nitrogen-copper bonds, resulting in a metal-organic hybrid.

The last part of this work explored the application of pCN thin films in waveguiding photonic devices. Due to its transparency through the visible and telecommunication wavelengths, combined with the highest intrinsic refractive index ever reported for organic polymeric thin films for the same range, pCN enables a compact waveguide design and strong mode confinement. However, the fabrication process needs to be further optimized to reduce sidewall roughness and, consequently, light scattering.

In conclusion, the results show that pCN has a great potential to guide and manipulate light, using starting materials that are sustainable and cost-effective. In addition, chemical vapor deposited high-quality and tunable thin films allow for free-standing and flexible devices. This could open the door for a new generation of organic-based and sustainable electromagnetic metamaterial systems with a small footprint and high throughput, which is a promising alternative to achieve enhanced light-matter interaction and replacement to inorganic materials, such as crystalline TiO_2.

Hereafter, I present an approach that has high potential to serve as a negative- and zero refractive index nano-optical device, using a pCN-based double-fishnet metamaterial structure.

Negative refractive index materials (NIMs) are of great interest for a variety of industrial applications. Veselago[1] had first theoretically predicted them more than 40 years ago as materials that have the real parts of both ε and μ to be simultaneously negative. In the past

several years, much effort has been made to engineer new materials with functional negative effective properties from microwave to optical frequencies. However, to satisfy the condition of having an effective medium at high frequencies, meta-atoms need to be engineered with sizes in the scale of several hundreds of nanometers, resulting in a significant drawback for NIMs nanofabrication. Due to the metallic nature of the metamaterial components, high dissipative losses at optical wavelengths limit desired feature properties. Overcoming the loss restrictions is one of the main challenges in the field nowadays[11]. One of the most recently proposed NIM structures, known as *double-fishnet* metamaterial, aims to compensate for the losses in optical metamaterials by using a pair of structured metal films separated by a dielectric layer[156,157]. And here is where the pCN thin films take place: as the dielectric media. In 2005, the low-loss alternative geometry of double-fishnet metamaterials was first reported working in the NIR range[158] and, later, in 2010, in the optical wavelength range; this was the first evidence that it was possible to overcome internal dissipative losses in optical NIM[159]. In the fishnet design, the "sandwiched" dielectric layer acts as an optically active "gain medium" that gives rise to an effective gain coefficient that can exceed its bulk counterpart when pumped by electrical injection. Further theoretical work has shown that besides loss-compensation, surface plasma amplification can also take part in a fishnet-designed structure, enhancing the negative RI response[157].

The fishnet structure is depicted in Figure 6- 1. It consists of an optically active system alternating metal-dielectric-metal layers with periodical nano-hole arrays with strong magnetic resonance. The design combines thick magnetic strips (short slabs along x) with thin electric strips (thin wires along y) in an arrangement that, when under the influence of an incident electromagnetic wave perpendicular to the xy-plane, ensures both lateral and normal coupling[160]. The alternating layers form small circuits that can bend light backward. Furthermore, the thin dielectric material sandwiched between the metal sheets strongly influences the tunability of the transmission and reflection of the metamaterial due to absorption[159].

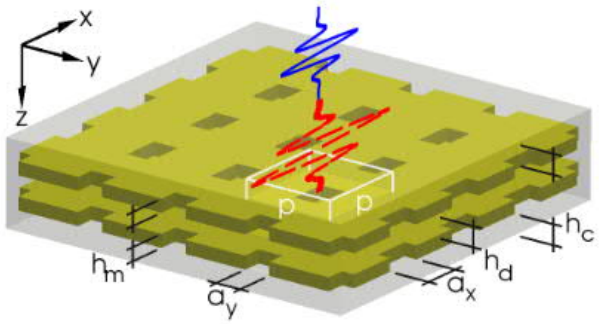

Figure 6- 1: Double fishnet material with two patterned silver films embedded in a dielectric host material under pump (red dashed line) and probe (blue line) pulses[11].

I would like to propose the same structure present in Figure 6- 1 composed of a gold double-fishnet alternated and embedded in pCN thin films. Such a pCN-based metamaterial can give rise to unconventional light-matter interactions, as negative- and zero refractive index and permittivity.

Over the past 50 years, the tech world of the silicon industry has faced enormous challenges pushing the fabrication limits of optical and electronic devices. Since the advent of the first transistor in 1947, much has been done about the miniaturization of integrated circuits (IC). "It is a staggeringly small world that is below", said Richard Feynman in his famous lecture "There's plenty of room at the bottom"[161], in 1959, followed by his discussion on miniaturizing computers and creating copies of tiny devices. Six years later, one of Intel's co-founders, Gordon Moore, coined his famous law about the shrinking of IC feature sizes. Moore's Law predicted that the number of transistors on a single chip would double every two years. In fact, the reality was faster than he had anticipated and, today, we are close to reaching the end of Moore's Law[36,162]. In less than 50 years, transistors downscaled from 10 µm to 10 nm, and it is now possible to have billions of transistors on a single chip, as opposed to a handful as at the beginning of the era[163–165]. Going after extremely small devices gave place to massive progress in lithography techniques, also concerning metamaterials. As we move toward high frequencies, the metamaterial features must become smaller and smaller to comply with the effective medium response. How can we overcome the fabrication constraints of such small features? Maybe that would be the new direction of Moore's Law – not trying to fit more and

more features on a chip but replacing them with a small number of components, with better performance (light-matter interaction), just by playing with their stack and geometry.

Chapter 7

Appendix

7.1 Characterization methods

7.1.1 Spectroscopic Ellipsometry

Spectroscopic ellipsometry is a reflection technique that allows us to perform contact-free non-destructive studies of thin films. Ellipsometry measurements in the visible as well as in the IR are used for thickness determination and structural investigation of thin films. Electronic or vibrational properties can be both examined depending on the photon energy.

Ellipsometry detects the phase change in polarization as light reflects from and/or is transmitted through samples. It does not measure the thickness and optical constants directly. Instead, it uses the collected data to solve models which estimate the thickness and optical parameters of interest. The machine measures Ψ and Δ using variable angles of incidence (45^{o}-90^{o}). The two mentioned angular parameters characterize the change in polarization as the light is reflected from the surface. Ψ represents the amplitude, and Δ represents the phase difference between p-

and s-polarized light waves (parallel and perpendicular to the plane of incidence, respectively). A scheme of a standard ellipsometry setup is shown in Figure 7-1.

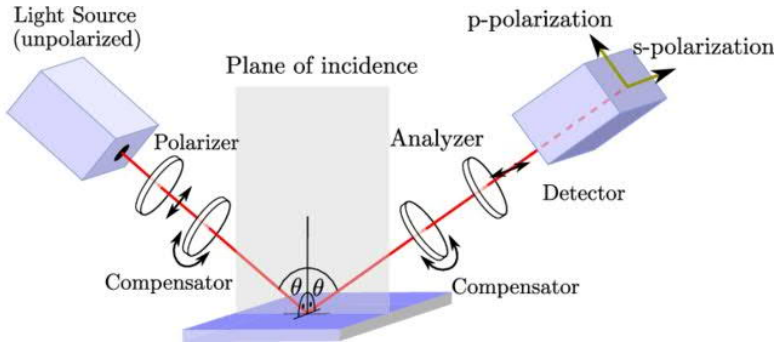

Figure 7- 1: Standard spectroscopy ellipsometry setup[166].

In order to avoid getting signals from the substrate and optimize the reflection only coming from the sample of interest, the measurements are made around the Brewster angle of the substrate (Table 7-12). The beam spot size is controlled by the angle of incidence, and it is described in Table 7-2.

Table 7-12: Brewster angle assigned to films on different substrates.

Brewster Angle*	
Thin Films on Si	65°, 75°
Thick Films on Si	60°, 75° or 55°, 65°, 75°
Films on Glass	50°, 60°, 70°
Films on Metals	65°, 75°
Anisotropic and graded films	55°, 65°, 75° or 45°, 60°, 75°

*Angle of incidence at which light with a particular polarization is perfectly transmitted through a transparent dielectric surface, with no reflection.

Table 7-13: Ellipsometer light beam angle vs. spot size.

Angle of Incidence	(spot-length)/(beam-diameter mm**)**
25º	1.1
35º	1.2
45º	1.4
55º	1.7
65º	2.4
75º	3.9

The main feature of ellipsometry measurements is the detection of the change in polarization. As seen previously in this thesis, light can be described as a transverse electromagnetic wave traveling through space, oscillating in the perpendicular direction to its travel direction (Maxwell's theory). A wave has a phase, a wavelength, and a polarity – the latter corresponds to the direction of the wave vector at any given point. Once the light reflects off of a surface, it gets polarized, at least partially, which means that, upon reflection, the direction of polarization is defined by the surface plane the light "hit" in the first place. Figure 7-1 shows the different light polarization states. When the light has a completely arbitrary orientation and phase, it is considered *unpolarized*. If two orthogonal waves are in phase, the resulting light is *linearly polarized*. A c*ircularly polarized* light is achieved when two perpendicular waves with the same amplitude are 90º out of phase. However, the most general polarization attributed to a monochromatic light wave is *elliptical,* and it is a combination of perpendicular waves of random amplitude and phase – and from where ellipsometry gets its name.

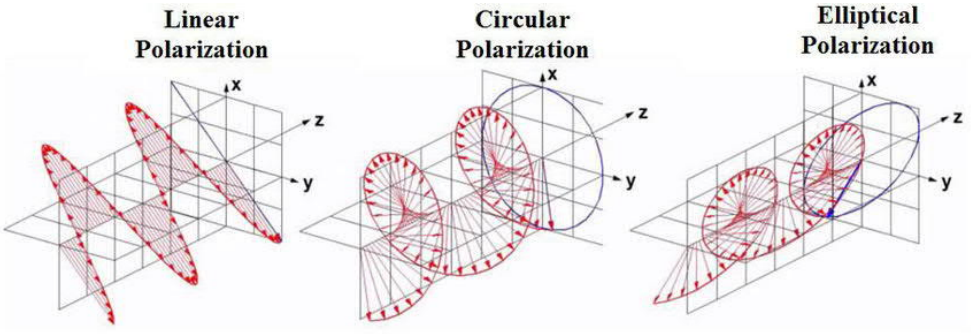

Figure 7- 2: Polarization types of the electromagnetic wave.

The ellipsometric angles Ψ and Δ used to express the polarized light are defined by the complex Fresnel coefficients, r_s, r_p, t_s, and t_p. These coefficients describe the amount of light reflected and transmitted at each interface between materials, considering the electric fields perpendicular and parallel (*s*- and *p-polarized*) to the plane of incidence, and are demonstrated from Equation 7.1 to 7.4[88,167].

$$r_s \equiv \frac{E_{rs}}{E_{is}} = \frac{n_i cos\theta_i - n_t cos\theta_t}{n_i cos\theta_i + n_t cos\theta_t} \tag{7.1}$$

$$r_p \equiv \frac{E_{rp}}{E_{ip}} = \frac{n_t cos\theta_i - n_i cos\theta_t}{n_t cos\theta_i + n_i cos\theta_t} \tag{7.2}$$

$$t_s \equiv \frac{E_{ts}}{E_{is}} = \frac{2n_i cos\theta_i}{n_i cos\theta_i + n_t cos\theta_t} \tag{7.3}$$

$$t_p \equiv \frac{E_{tp}}{E_{ip}} = \frac{2n_i cos\theta_i}{n_t cos\theta_i + n_i cos\theta_t} \tag{7.4}$$

Where:

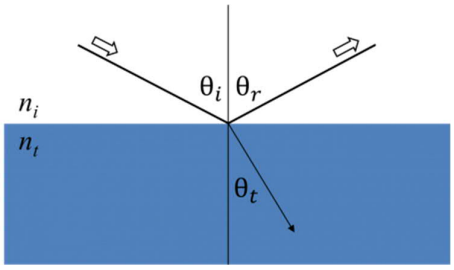

Figure 7- 3: Reflected and refracted light on an interface (Snell's Law).

The ellipsometry setups used in this thesis were the J.A. Woollam M-2000U® (measurements in the range of 245-1000 nm, 55º to 75º) and M-2000® (370-1670 nm, 55º to 75º). For the environmental ellipsometry porosimetry experiments, a chamber coupled to a mass flow controller was located on the sample holder of a J.A. Woollam M-2000U®, and the measurements were taken at 70º while flushing a controlled gas flow of isopropanol and ethanol. All the data analyses until here were performed using the CompleteEASE software. Ellipsometry IR experiments were performed using a variable angle spectroscopic ellipsometer (IR-VASE) with a rotating compensator ellipsometer (RCE), also from J.A. Woollam, from 260 to 5265 cm^{-1}. The IR data were treated using the WVASE32 software and converted to the CompleteEASE.

7.1.2 X-ray photoelectron spectroscopy (XPS)

X-ray photoelectron spectroscopy (XPS) is a surface chemistry characterization technique based on the photoelectron effect. When a surface is irradiated with a beam of x-rays (0.01 to 10 nm) of sufficient energy, hv, electrons from specific bound states are excited. Thus, the x-ray photons ionize the molecules or atoms, and electrons from the core levels are ejected with a specific kinetic energy, $E_{kinetic}$, which is equal to the difference between the x-ray photons and the binding energy of the electrons, $E_{binding,}$ as described in Equation 7.5.

$$E_{kinetic} = hv - E_{binding} - \emptyset \tag{7.5}$$

Where $\emptyset$ is the spectrometer work function.

The binding energy of the electrons is a unique characteristic of each different atom, making it a suitable parameter to determine elemental analysis. The emitted electrons are then collected by an electrostatic lens and analyzed by a spectrometer, producing an energy spectrum of intensity (or counts of the ejected electrons) versus the binding energy – the peaks displayed in the spectrum come from atoms emitting electrons of specific energy. The system operates under UHV to direct the electrons into the detector, avoiding scattering and contaminations. Furthermore, the probed depth is limited to a few nanometers within the sample due to elastic and inelastic interactions of the photoelectrons with other atoms[168,169].

In this work, XPS measurements were carried out under UHV conditions in a system connected to the low-temperature STM/nc-AFM setup for direct transfer of the in situ samples when needed. The XPS experiments were performed with a K-alpha from Thermo VG Scientific, consisting of a monochromated Al K_a x-ray source (standard: 75W, ~ 400 μm spot diameter). The photoelectron detection was carried in normal emission with a SPECS PHOIBOS 100 hemispherical analyzer with a 2D delay-line detector. The deconvolution and fitting of the peaks were performed using the CasaXPS software.

7.1.3 Electron Microscopy (SEM, EDX, HRTEM)

Analogous to the optical microscope, which uses photon energy to magnify projected images through a simple lens, electron microscopes use a beam of electrons (and their wave-like properties) that allow greater magnification through an electrostatic or electromagnetic lens, producing electric and magnetic fields to guide and focus the electrons. Electrons have wavelengths much shorter than photons, resulting in magnifications up to a million times, which is much more than the limited magnification of only around a thousand times of their optical counterparts.

There are two main types of electron microscopes – the scanning electron microscope (SEM) and the transmission electron microscope (TEM). In an SEM setup, the image is formed by scanning a high-energy electron beam onto the sample surface in a raster pattern under high

vacuum conditions. The focus position of the electron beam onto the sample is controlled by a set of scan coils placed above the objective lens. As the electrons interact with the sample, different signals such as low-energy secondary electrons (SE), high-energy backscattered electrons (BSE), x-rays, and other photons with different energies are produced and collected by specific detectors. Secondary and backscattered electrons are the most frequently used signals because they vary according to the topography and chemical composition (Z-contrast) of the scanned sample, respectively. It is crucial to highlight that, for SEM characterizations, the sample needs to be electrically conductive to allow the electrons coming from the electron beam to move freely and avoid charge accumulation, which can result in thermal damage. The preparation of non-conductive samples involves an ultrathin coating with an electrically conductive material.

The most common microanalysis equipment coupled to the SEM setup is the energy-dispersive X-ray spectrometer (EDX or EDS), which records x-rays of all energies simultaneously. X-ray photons are emitted when the electron beam hits the sample, knocking off an electron from the inner shell of an atom, leaving a positively charged electron-hole. A negatively charged electron from high-energy shells is then attracted to the hole in the lower-energy shell, releasing the difference in energy as x-ray photons. Each chemical element within the sample has a characteristic x-ray, meaning the output signal is proportional to the atomic number, making EDX a valuable tool for identifying and quantifying atomic elements.

As opposed to the SEM system, in a conventional TEM setup, the electrons are not scattered from the sample but are transmitted through it, giving additional information about the internal structure of the specimen. So that the electrons can pass entirely through the sample and arrive at the lenses and the detector below it, creating a 2D image, the sample needs to be extremely thin, of less than 100 nm. TEM has a magnification capacity of 10 to 50 million times, which is much more than that of SEM. Thus, it is possible to image morphological, compositional, and crystallographic information with high resolution (0.2 nm compared to 10 nm for SEM).

High-resolution TEM (HRTEM) systems use both transmitted and scattered electrons to create an interference image. The direct electron beam interacts with the diffraction electron beam resulting in a phase-contrast image, allowing for direct imaging of individual atoms within the sample[170–172].

The morphology of the pCN thin films was investigated using a Zeiss Leo 1550-Gemini SEM microscope, with acceleration voltages from 3 to 10 kV. Elemental mapping was performed through energy-dispersive x-ray spectroscopy (EDX) using an X-Max 80 mm^2 detector from Oxford Instruments. For the SEM imaging, the samples were sputtered with an ultrathin layer of Au/Pd. High-resolution TEM images of the amorphous pCN structure were obtained with a JEOL JEM-ARM200F operated at 80 kV, equipped with a cold-emission gun.

7.1.4 Scanning probe microscopy (SPM)

Scanning probe microscopy (SPM) comprises a group of scanning probe techniques for the characterization and manipulation of materials at the nanoscale. It uses a probe with a sharp tip (probe) to sense the probe-to-surface atom interaction, and the nature of this interaction is what distinguishes every different SPM method. For example, scanning tunneling microscopy (STM) is based on measuring the tunneling current between a very sharp metal wire tip and a conductive sample. A tunneling current results from a quantum mechanical effect that happens when an electron with wave-like properties can cross a barrier, which is thin enough for that to happen, even if the electron does not have enough energy to do so. Depending on the STM setup, voltage is applied either on the tip or the sample. When the tip is placed near the surface, a flow of electrons starts to tunnel through the vacuum space in between. Additionally, a feedback control mechanism is used to adjust the tip height and preserve the tunneling current while the tip scans the surface. With this, it is possible to image the surface at extremely tiny scales down to atomic resolution. However, due to the tunneling effect, STM has to be performed on conducting or semiconducting samples.

To overcome the STM drawback on non-conductive samples, another SPM technique can be used as an alternative. Atomic force microscopy (AFM) measures the small force between the tip and the sample as a signal instead of the tunneling current. In the AFM setup, the tip is attached to a cantilever which forms a spring. As the tip approaches the surface, the interaction force between the sample and the tip causes the cantilever to bend towards or away from the surface. By knowing the stiffness of the cantilever, the force can be calculated through its deflection, which is detected by a laser beam deflection system. AFM can be operated in different modes, overall classified as *contact mode (or static mode)*, *tapping mode,* and *non-contact mode (dynamic mode).* In contact mode, the surface is mapped by changing the z-position of the tip, keeping the tip-sample distance constant while scanning. The changes in the z-position applied to maintain the force constant in the repulsive regime are what results in the topography imaging of the sample. However, contact mode can damage the sample and the probe, causing artifacts in the acquired images. The intermittent tapping mode also brings the tip in contact with the sample, but instead of dragging it around, as with contact mode, the cantilever is oscillated close to the surface, partially extending it to the repulsive regime and slightly touching the surface. This intermittent tapping of the surface increases the lateral resolution when imaging. Dynamic modes (non-contact modes) use an oscillating cantilever, but only around the attractive regime, meaning it does not touch the sample. In this regime, the forces are low, and the force measurements are performed according to the cantilever amplitude. Non-contact modes are mainly applied to soft samples, such as polymers, which can get destroyed when in contact with the tip[173].

Hybrid STM/AFM systems are also commonly used to combine currents and force measurements simultaneously at the atomic scale.

For the topographic images of the pCN thin films, we used a Bruker JPK NanoWizard AFM system with standard Arrow-NCR probe tips (<10 nm diameter), force constant of 42 N/m, and resonance frequency of 285 kHz. The experiments were carried out under AC-mode (tapping mode). Additionally, the images had a pixel size of 512x512 and were taken within a 05-08 Hz LineRate range. All the images were flattened and processed using the JPK SPM data process software.

The in situ STM/nc-AFM measurements were carried out using a low-temperature SPM system (ScientaOmicron LT-STM/nc-AFM) under ultra-high vacuum conditions (UHV) and liquid nitrogen temperature. A commercial quartz tuning fork cantilever in qPlus configuration with a chemically etched tungsten wire probe tip (f_0 = 28 kHz; Q = 5822 at 78 K) was used for both STM and nc-AFM images.

7.1.5 X-ray diffraction (XRD)

X-ray diffraction is an analytical technique primarily used to identify an unknown inorganic or organic material and its unit cell dimensions. It works based on the principle that the incident x-rays are elastically scattered off of the atoms within the specimen, creating constructive interferences when the interatomic distances are larger than the wavelength of the x-rays, as expressed by Bragg's Law (Equation 7.6):

$$2dsin\theta = n\lambda \tag{7.6}$$

Where d is the interplanar distance, θ is the incident angle, n is an integer, and λ is the incident x-ray wavelength.

The diffraction phenomenon occurs when an electromagnetic wave encounters a periodic structure, and it splits itself into several waves traveling in different directions. In powder XRD, the x-ray scattering interferences create a characteristic reflection pattern, which gives the position and intensity of the peaks in the diffractogram. Thus, highly crystalline samples result in sharp peaks, and broadening of the peaks occurs when lattice defects are present or crystallites size becomes smaller. Amorphous materials have no reflection due to the randomness of the atomic packing[174,175].

The physical and chemical properties of thin films are quite different from the respective bulk counterparts, commonly used for XRD characterization. Therefore, partially amorphous thin films are more efficiently characterized using a different setup geometry, called grazing incidence x-ray diffraction (GIXRD). In this geometry, the incident angles for the incoming x-

rays are considerably small, and the Bragg reflections are only surface sensitive[176]. The θ geometry can also be used for nanostructured materials but with a much longer acquiring time.

The thin film XRD measurements were performed on a Bruker D8 thin film XRD with Cu-Anode (Kα1+2), Göbel mirror, Sol-X energy-dispersive single counter. The diffraction data were recorded for ~10h (per sample) in the range of 5°-100° 2θ, with a usual step width of 0.03°. The experiments were done in collaboration with Dr. Michael Tovar, from the Helmholtz Zentrum Berlin (HZB). The stacking was evaluated by applying the Rulan and Smarsly model[177]. This last part was a collaboration with Oliver Oßwald from the University of Giessen.

7.1.6 UV-VIS-NIR Spectroscopy

UV-VIS-IR spectrometers are employed for absorbance, transmittance, and reflectance measurements of solid and liquid samples by collecting the light intensity/energy at different frequencies. Measurements in the UV-VIS-NIR range cover the wavelengths from about 190 nm to 3300 nm. There are two basic absorption processes in the considered wavelength range: electronic transitions and vibrational transitions. When an atom or molecule absorbs UV-VIS light, the high-energy photons are absorbed by the bound electrons, leading to transitions among the electronic energy levels of the molecule. For most organic compounds, these transitions correspond to π-π^* or n-π^* transitions, and the spectra can reveal information about the color (when in the visible) and structure of a molecule. The transitions measured in the NIR region of the electromagnetic spectrum are related to molecular vibrations. When NIR or IR radiation strikes a molecule, it causes the molecule to bend and vibrate due to periodic changes of the dipole moment.

For solid samples, transmittance and reflectance are measured using an integrating sphere. The sample is located in front of the integrating sphere for transmittance mode and behind it for reflectance mode. The integrating sphere is needed so one can measure the overall values and compare them to the direct ones. The absorbance can be calculated considering the light percentage that was neither transmitted nor reflected.

Transmittance measurements of the pCN thin films were made using a UV-VIS-NIR Perkin Elmer Lambda 900, from 190 to 3300 nm. The experiments were performed by Dr. –Ing. Oliver Görke from the Berlin Institute of Technology (TU Berlin).

7.1.7 Nanoindentation

Nanoindentation is a technique applied to mechanical testing with micron spatial resolution. It is typically used to test the hardness, elastic modulus (Young's modulus), and related mechanical properties of thin films. It works similarly to conventional mechanical testing, but the penetration depth is measured in the nanometer range.

During nanoindentation measurements, a calibrated indenter tip (with known mechanical properties) is pressed into the sample's surface (with unknown properties) while force and displacement are recorded, resulting in a load-displacement curve, which provides quantitative information about the mechanical properties of the sample.

The hardness and Young's modulus of pCN thin films were analyzed with a Triboindenter TI-950 nanoindenter (Hysitron-Bruker), equipped with a standard 2D transducer and a Berkovich tip. The tip was calibrated for the contact depths of 5-100 nm using a standard Fused Quartz sample (E=69.6 GPa). The penetration depth was 20 nm for samples IP 10, IP 15, IP 20, t-2, t-3, and fw-1, and 7 nm for sample fw-3. To ensure that the probing areas were clean and smooth, scanning probe microscopy (SPM) has been done prior to the indentation studies. The Oliver-Pharr method was used for the calculation of the elastic modulus and hardness of the samples. The data are reported in mean+/- standard variation.

7.2 Materials

Melamine (99%, Sigma Aldrich), PMMA e-beam resist (AR-P 672.045), silicon wafer with native oxide (Prime CZ-Si wafer 2 inches, thickness = 400 ± 25 µm, (111), 1-side polished, n-type Arsenic, Microchemicals), silicon wafer with wet SiO_2 (Prime Si + wet SiO_2 wafer, 3 inches, thickness = 381 ± 25 µm, (100), 1-side polished, p-type Boron, 2000 and 3000 nm wet SiO_2, Microchemicals), fused silica wafer (JGS1 wafer 2 inches, thickness = 500 ± 25 µm, 2-side polished, Microchemicals), copper (111) single crystal substrate (9 mm x 9 mm x 1.80 mm, 1-side polished, MaTeck GmbH).

7.3 Supplementary Figures and Tables

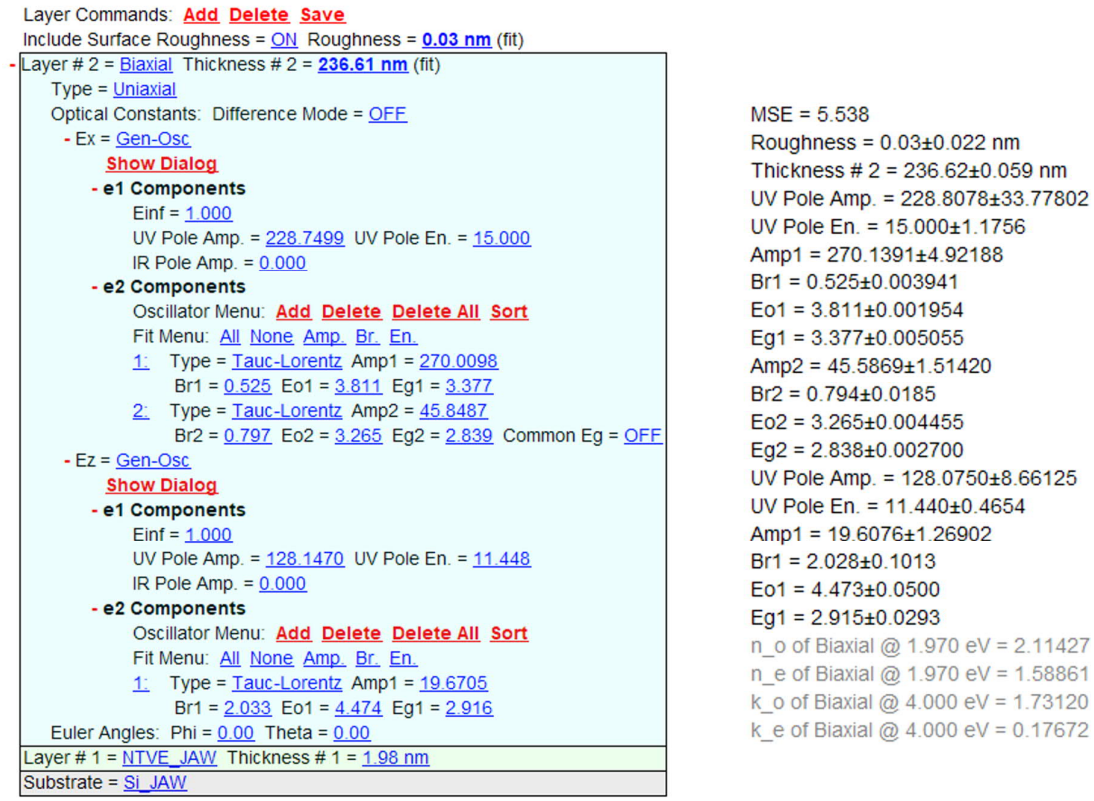

Figure A- 1: *Ellipsometry fitting model (CompleEASE software) for sample IP 10 detailing the two Tauc-Lorentz oscillators parameters applied for the in-plane and the one Tauc-Lorentz oscillator parameters in the out-of-plane.*

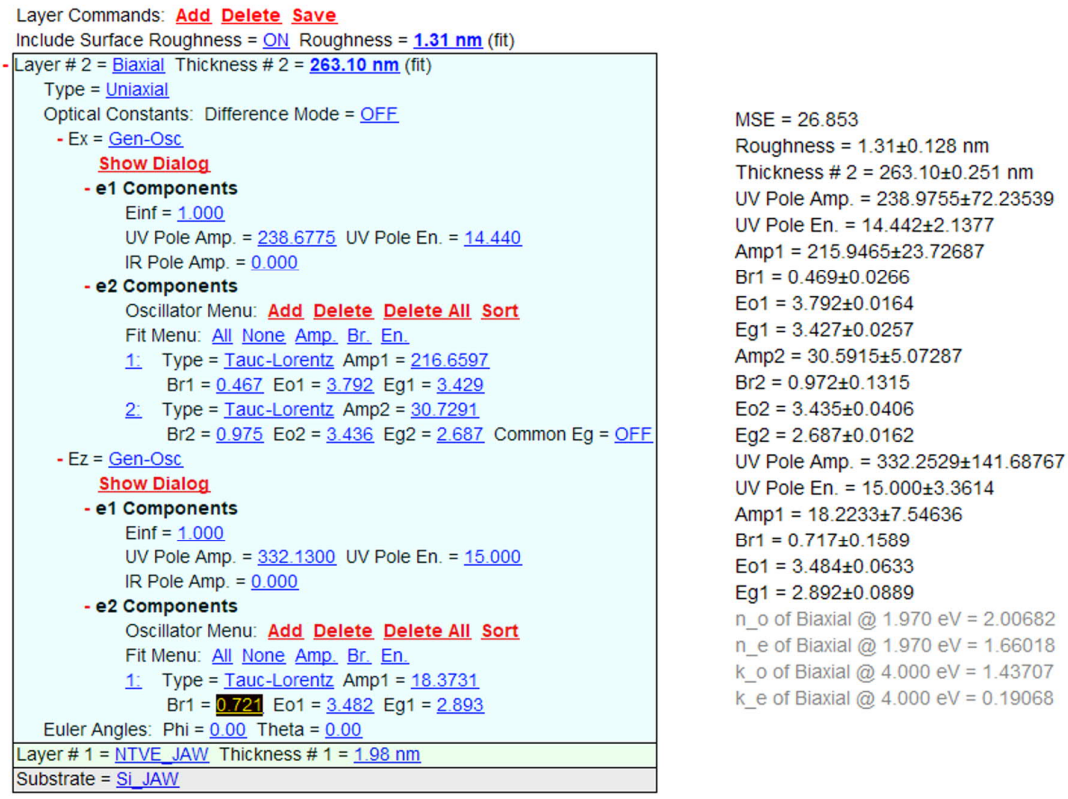

Figure A- 2: *Ellipsometry fitting model (CompleteEASE software) for sample IP 15 detailing the two Tauc-Lorentz oscillators parameters applied for the in-plane and the one Tauc-Lorentz oscillator parameters in the out-of-plane.*

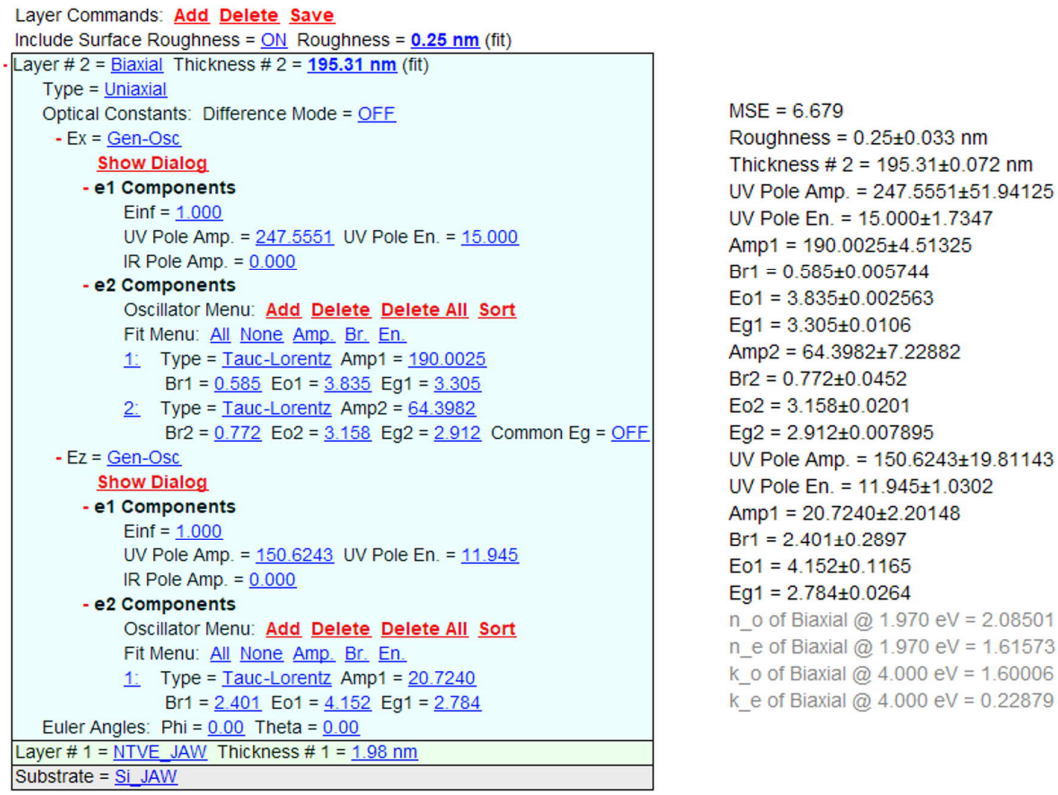

Figure A- 3: *Ellipsometry fitting model (CompleteEASE software) for sample IP 20 detailing the two Tauc-Lorentz oscillators parameters applied for the in-plane and the one Tauc-Lorentz oscillator parameters in the out-of-plane.*

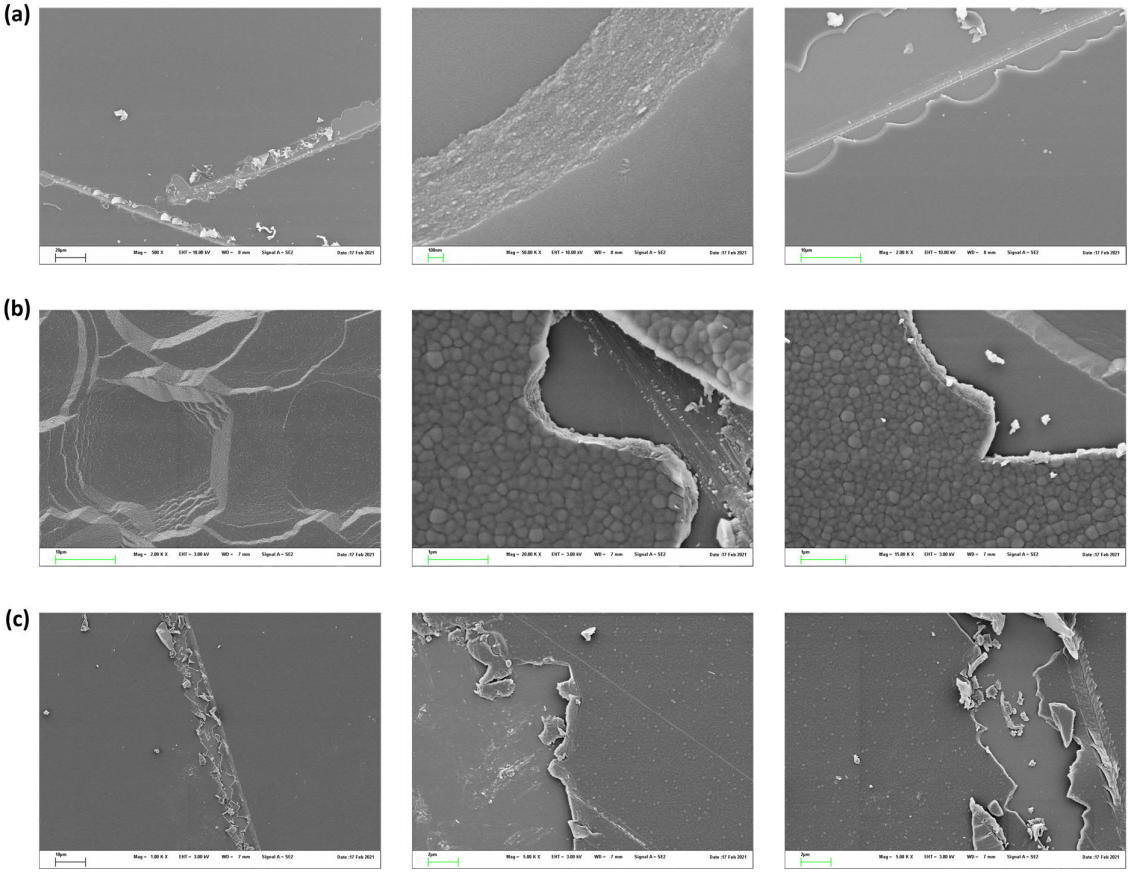

Figure A- 4: *Scanning electron microscopy (SEM) images of samples a) IP 10, b) IP 15, and c) IP 20.*

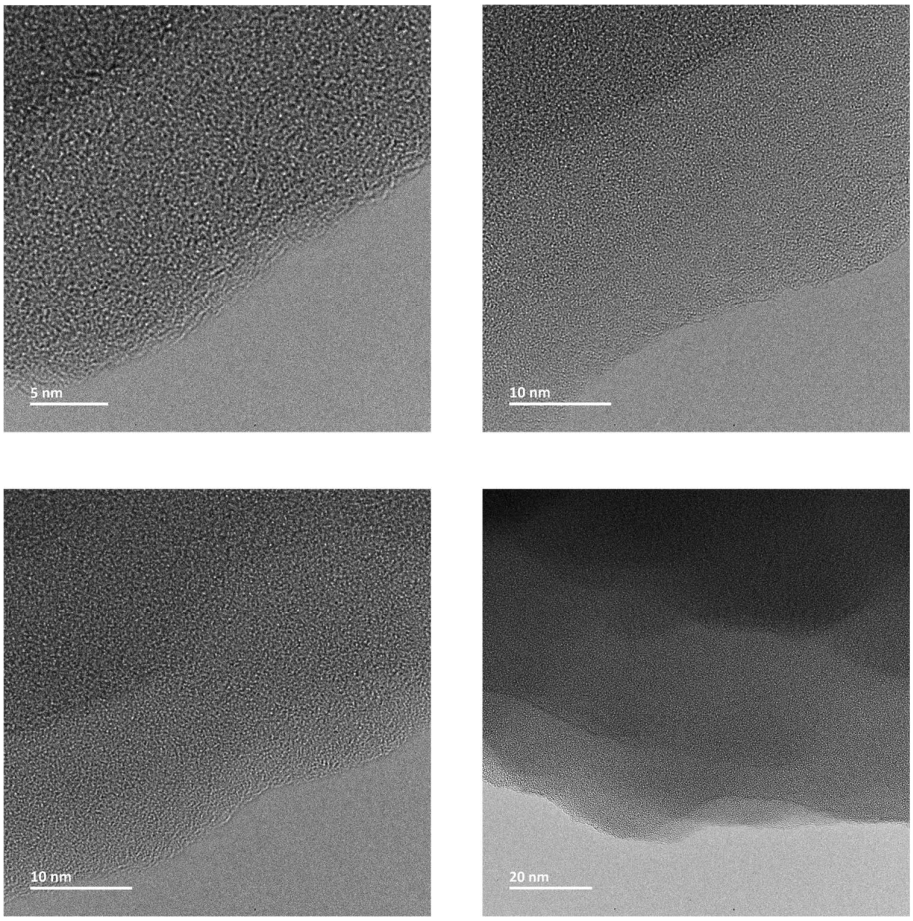

Figure A- 5: *High-resolution transmission electron microscopy (HRTEM) images of the amorphous and layered structure of pCN thin films (sample IP 15) prepared with an ultramicrotome cross-section cut.*

Table A- 1: *Nanoindentation measurements of sample IP 10. hc(nm) is the penetration depth, Er(GPa) is the Young's Modulus, and H(GPa) the hardness of the sample. The mean and standard values were 18.2 ± 3.9 GPa for Young's modulus and 1.32 ± 0.3 GPa for the hardness.*

IP 10		
hc(nm)	Er(GPa)	H(GPa)
12.110336	13.353419	1.053437
12.289239	13.912248	1.068699
12.551521	16.065228	1.223467
12.592317	20.968116	1.536587
12.950983	25.538805	1.800703
12.997551	14.624141	1.049782
12.442361	18.774325	1.419973
12.374895	26.044898	1.899394
12.863627	22.083308	1.535935

12.582943	19.262811	1.481027
12.134382	21.014062	1.678504
12.459019	15.139667	1.048433
13.422452	16.599272	1.029075
13.190234	19.762839	1.356227
12.788731	19.316225	1.368520
14.332397	19.707810	1.058162
12.236609	14.337817	1.135791
13.234207	19.690024	1.269212
13.470442	15.877186	1.001263
13.470992	21.081474	1.342420
12.622958	14.324151	1.089127
11.364568	11.536688	1.067485
12.594565	15.559145	1.115419
11.962603	23.827503	2.021135
12.915195	16.449747	1.232533

Table A- 2: *Nanoindentation measurements of sample IP 15. hc(nm) is the indentation depth, Er(GPa) is the Young's Modulus, and H(GPa) the hardness of the sample. The mean and standard values were 15.4 ± 1.4 GPa for Young's modulus and 1.17 ± 0.08 GPa for the hardness.*

IP 15		
hc(nm)	Er(GPa)	H(GPa)
13.172644	17.433283	1.167418
12.660452	15.847052	1.208379
12.432765	12.926336	1.047250
12.422094	14.916949	1.089846
12.470050	14.684278	1.183004
12.485546	15.663234	1.164018
12.162208	13.547048	1.086563
12.540487	16.109720	1.193589
12.721975	15.973756	1.186240
12.538304	13.281748	0.970913
12.678903	15.656370	1.177388
12.413328	13.807652	1.068078
12.767997	17.202704	1.269610
12.945862	15.290451	1.114434
13.051784	16.529300	1.203546
12.272436	14.571582	1.130999
12.399312	16.900147	1.233645
12.631113	14.753150	1.118936
13.029979	18.602776	1.296751

12.176353	14.009837	1.166100
12.268062	16.700010	1.331404
12.154200	14.732046	1.187022
12.451002	15.148136	1.223436

Table A- 3: *Nanoindentation measurements of sample IP 20. hc(nm) is the indentation depth, Er(GPa) is the Young's Modulus, and H(GPa) the hardness of the sample. The mean and standard values were 20.5 ± 2.9 GPa for Young's modulus and 1.39 ± 0.2 GPa for the hardness.*

IP 20		
hc(nm)	Er(GPa)	H(GPa)
14.190687	27.433831	1.567615
13.105299	21.635970	1.469055
12.892993	18.454306	1.286745
13.425226	16.703712	1.089000
13.133800	18.908212	1.297776
12.770196	17.470009	1.192675
13.711604	22.763026	1.471371
13.540697	23.028877	1.474482
13.047058	21.415874	1.468220
13.125486	19.069447	1.216092
12.991877	17.295176	1.246797
12.246044	21.684334	1.700843
13.885552	21.921564	1.399097
13.382090	14.660131	0.997571
12.722825	17.726189	1.261718
13.205251	23.882669	1.590192
13.982347	17.605415	1.061729
12.844707	21.361361	1.479910
12.935578	21.012033	1.492395
12.621051	23.630920	1.680068
14.040356	21.125614	1.276736
12.983262	22.229784	1.530409
12.835132	16.934862	1.194769
12.546026	20.100592	1.514464
12.766445	23.761731	1.671552

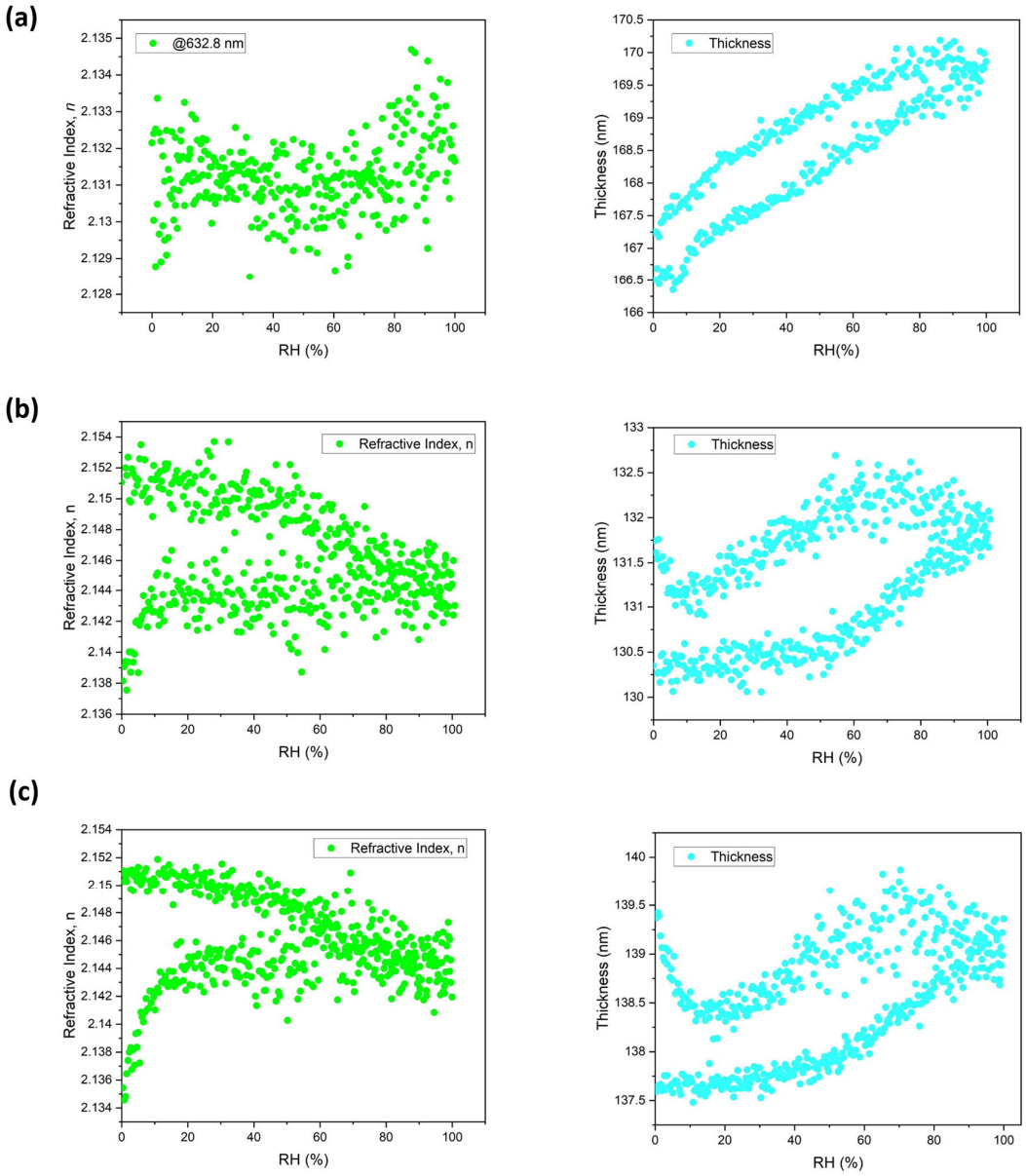

Figure A- 6: *Isotherms obtained with ellipsometry porosimetry experiments (EPP) for pCN samples with different thicknesses.*

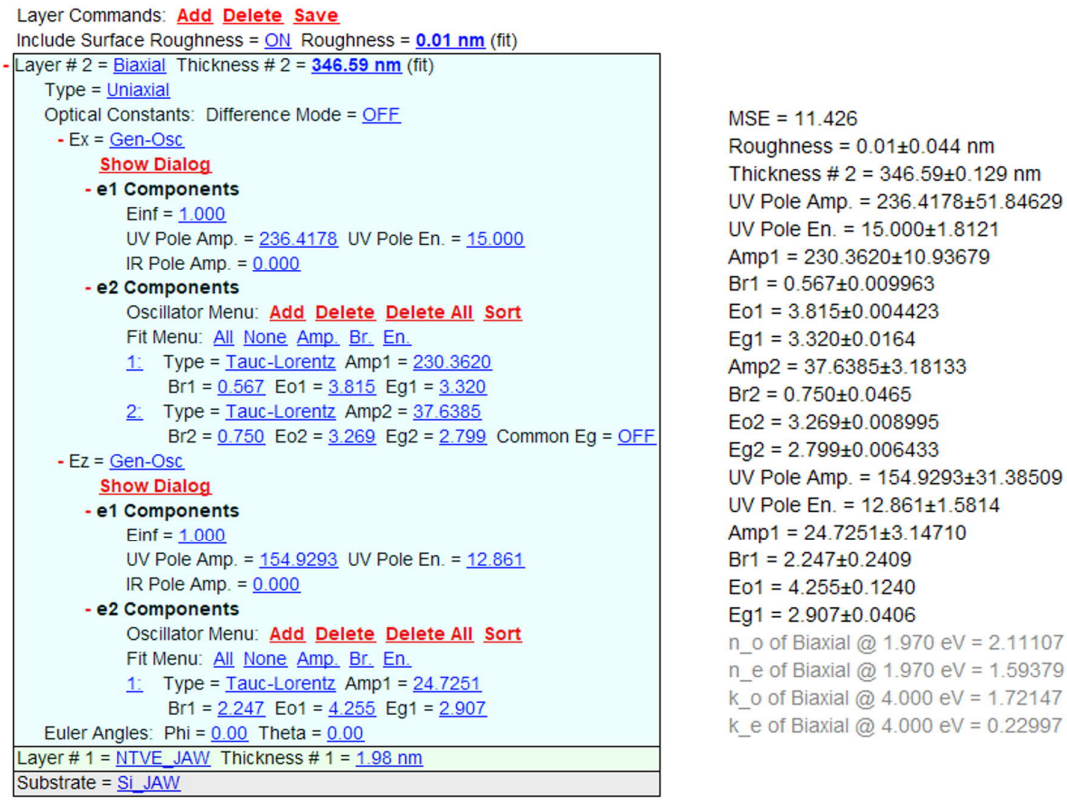

Figure A- 7: *Ellipsometry fitting model (CompleteEASE software) for sample t-2 detailing the two Tauc-Lorentz oscillators parameters applied for the in-plane and the one Tauc-Lorentz oscillator parameters in the out-of-plane.*

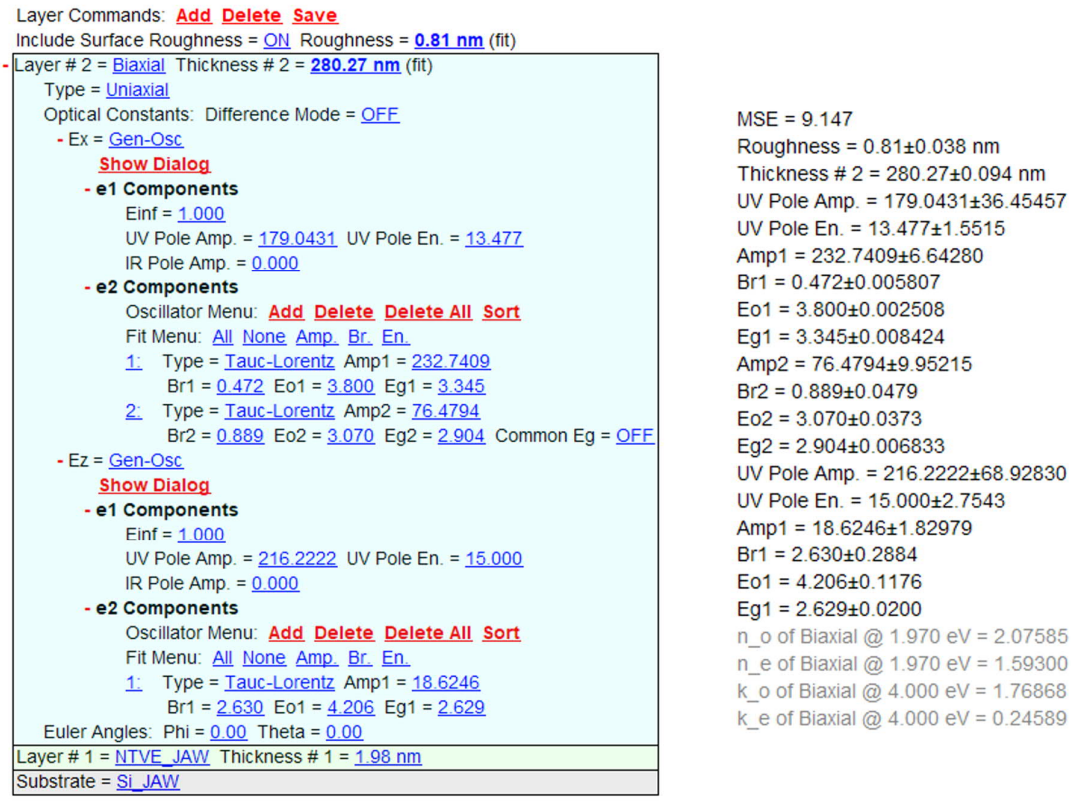

Figure A- 8: *Ellipsometry fitting model (CompleteEASE software) for sample t-3 detailing the two Tauc-Lorentz oscillators parameters applied for the in-plane and the one Tauc-Lorentz oscillator parameters in the out-of-plane.*

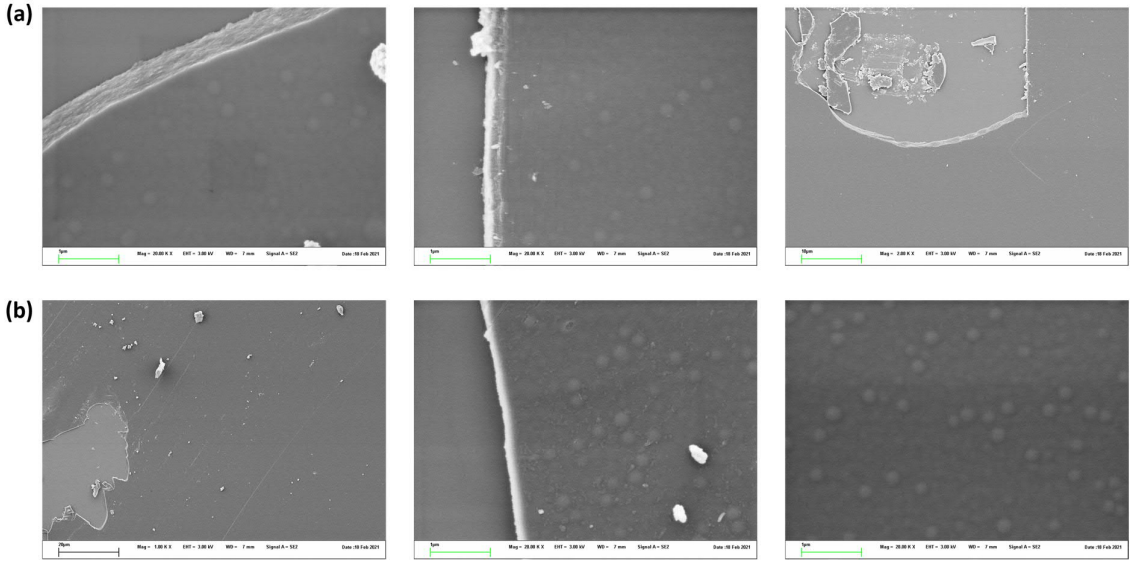

Figure A- 9: *Scanning electron microscopy (SEM) images of samples a) t-2 and b) t-3.*

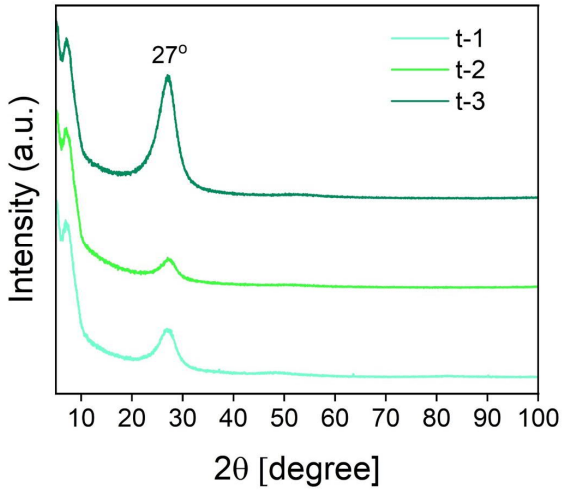

Figure A- 10: *Thin film x-ray diffraction (XRD) spectra of samples t-1, t-2, and t-3.*

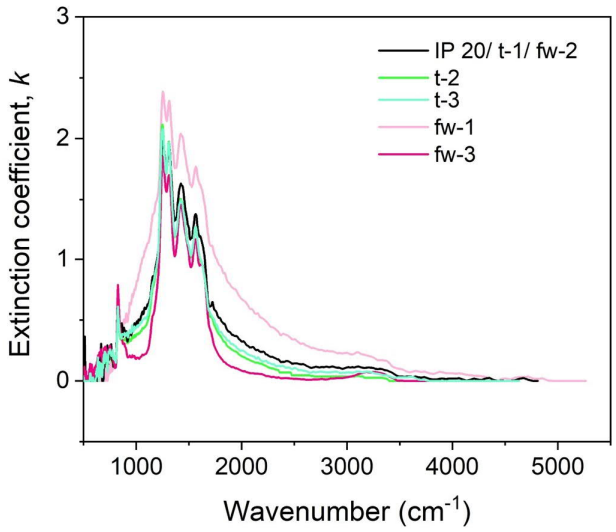

Figure A- 11: *IR ellipsometry spectroscopy spectra of samples IP 20/t-1/fw-2, t-2, t-3, fw-1, and fw-3.*

Table A- 4: *Nanoindentation measurements of sample t-2. hc(nm) is the indentation depth, Er(GPa) is the Young's Modulus, and H(GPa) the hardness of the sample. The mean and standard values were 14.8 ± 1.4 GPa for Young's modulus and 1.2 ± 0.13 GPa for the hardness.*

t-2		
hc(nm)	Er(GPa)	H(GPa)
12.136270	14.959881	1.157703
11.922225	13.718382	1.101473
11.611344	16.795638	1.453766
12.311958	13.058276	1.062225
11.939320	15.564063	1.222879
11.947425	13.330733	1.108143
12.335239	13.874034	1.125000
11.325518	16.455924	1.457498
11.684559	14.190091	1.204771
12.379822	14.489131	1.072024
11.907352	15.860409	1.301263
12.087153	14.255964	1.151438
12.637860	13.036960	1.013402
11.848286	12.225133	0.997228
12.072987	16.464385	1.229108
12.191941	14.894104	1.134363
11.717498	17.205567	1.405939
12.078964	13.278377	1.083527

12.362114	14.221971	1.111585
12.277104	14.248384	1.132242
12.536526	16.887769	1.353391
11.876309	16.545093	1.346203
12.479629	15.565630	1.269009
11.818723	15.118424	1.223266

Table A- 5: *Nanoindentation measurements of sample t-3. hc(nm) is the indentation depth, Er(GPa) is the Young's Modulus, and H(GPa) the hardness of the sample. The mean and standard values were 15.3 ± 1.9 GPa for Young's modulus and 1.09 ± 0.15 GPa for the hardness.*

t-3		
hc(nm)	Er(GPa)	H(GPa)
12.407567	9.360116	0.707624
12.857084	15.817012	1.151212
13.098017	16.023261	1.059854
12.528875	12.686845	0.988084
13.547396	16.753747	1.137855
13.256619	15.599437	1.037351
13.427602	13.687527	0.882393
12.440390	15.411476	1.105304
12.846456	16.948929	1.226935
12.871785	16.943943	1.230326
12.579032	14.306897	1.022794
13.362035	17.208317	1.142034
12.719472	16.712152	1.244887
13.772856	14.102376	0.924374
12.901172	14.060735	1.008266
13.043082	16.434525	1.130434
12.717349	15.546989	1.102520
12.683254	16.858829	1.256401
13.197163	13.025005	0.920509
13.151003	15.189298	1.077299
12.496137	15.081033	1.182721
12.240986	15.979188	1.290657
12.706588	17.015480	1.265440
12.638481	18.389258	1.335641
13.023358	13.559306	0.939121

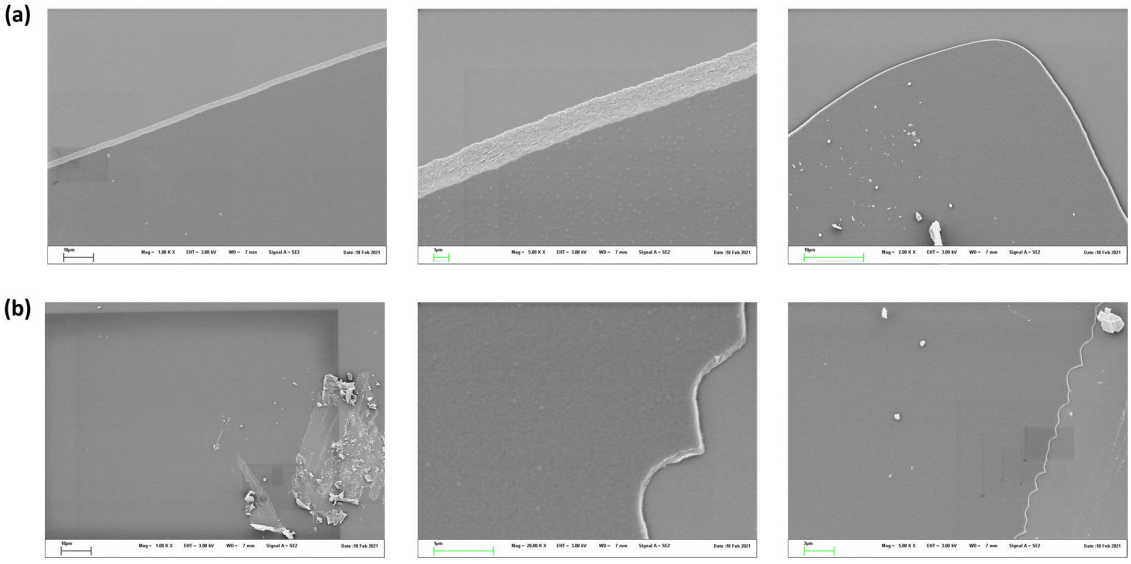

Figure A- 12: *Scanning electron microscopy (SEM) images of samples a) fw-1 and b) fw-3.*

Table A- 6: *Nanoindentation measurements of sample fw-1. hc(nm) is the indentation depth, Er(GPa) is the Young's Modulus, and H(GPa) the hardness of the sample. The mean and standard values were 13.4 ± 1.5 GPa for Young's modulus and 1.13 ± 0.1 GPa for the hardness.*

fw-1		
hc(nm)	Er(GPa)	H(GPa)
11.159849	12.227971	1.098659
10.753870	12.239912	1.244490
12.708770	17.605916	1.065763
11.136628	12.199120	1.141377
11.305193	12.609378	1.123952
11.872171	13.494454	1.181878
11.918464	13.554230	1.122677
11.463925	11.568154	1.048375
12.540195	13.109886	1.044292
11.435886	11.024112	1.026826
11.527911	12.565802	1.084080
11.645687	13.189364	1.158623
12.000353	13.079444	1.035632
11.915901	13.669965	1.129352
12.128314	16.574584	1.370705
12.947708	16.003767	1.102301
11.196176	13.530712	1.280658
11.934364	12.129365	1.009507
11.647462	13.245381	1.123087

11.660686	14.517256	1.285979
11.367497	14.393138	1.335853
12.586567	13.720292	1.041469
11.740004	12.379010	1.091092
12.345382	12.831718	1.043120
11.769225	13.579119	1.114049

Table A- 7: *Nanoindentation measurements of sample fw-3. hc(nm) is the indentation depth, Er(GPa) is the Young's Modulus, and H(GPa) the hardness of the sample. The mean and standard values were 22.0 ± 4.7 GPa for Young's modulus and 2.38 ± 0.47 GPa for the hardness.*

fw-3		
hc(nm)	Er(GPa)	H(GPa)
15.890819	63.910884	2.854060
15.194173	67.050874	2.839331
15.740575	68.058872	2.511522
15.069137	58.770138	2.601536
15.488657	56.650961	2.148526
15.492238	60.618160	2.514222
15.925525	53.425332	1.816262
15.832249	56.224833	2.214584
15.469007	57.750485	2.380381
15.447541	66.056022	2.488195
15.629949	84.254617	3.212337
15.630612	58.462707	2.105443
15.554287	45.420011	1.697866
15.553866	60.552165	2.356126
15.759239	61.242945	2.388885
15.781427	64.816285	2.526472
16.442164	62.168569	2.198449
16.200118	48.885016	1.752119
15.813759	85.361700	3.071729
15.785062	51.130377	1.961096
15.877705	48.002585	1.543028
15.838893	66.312051	2.539100
15.146894	80.839351	3.423161
15.461755	57.628987	2.208226
16.234366	56.134276	2.049691

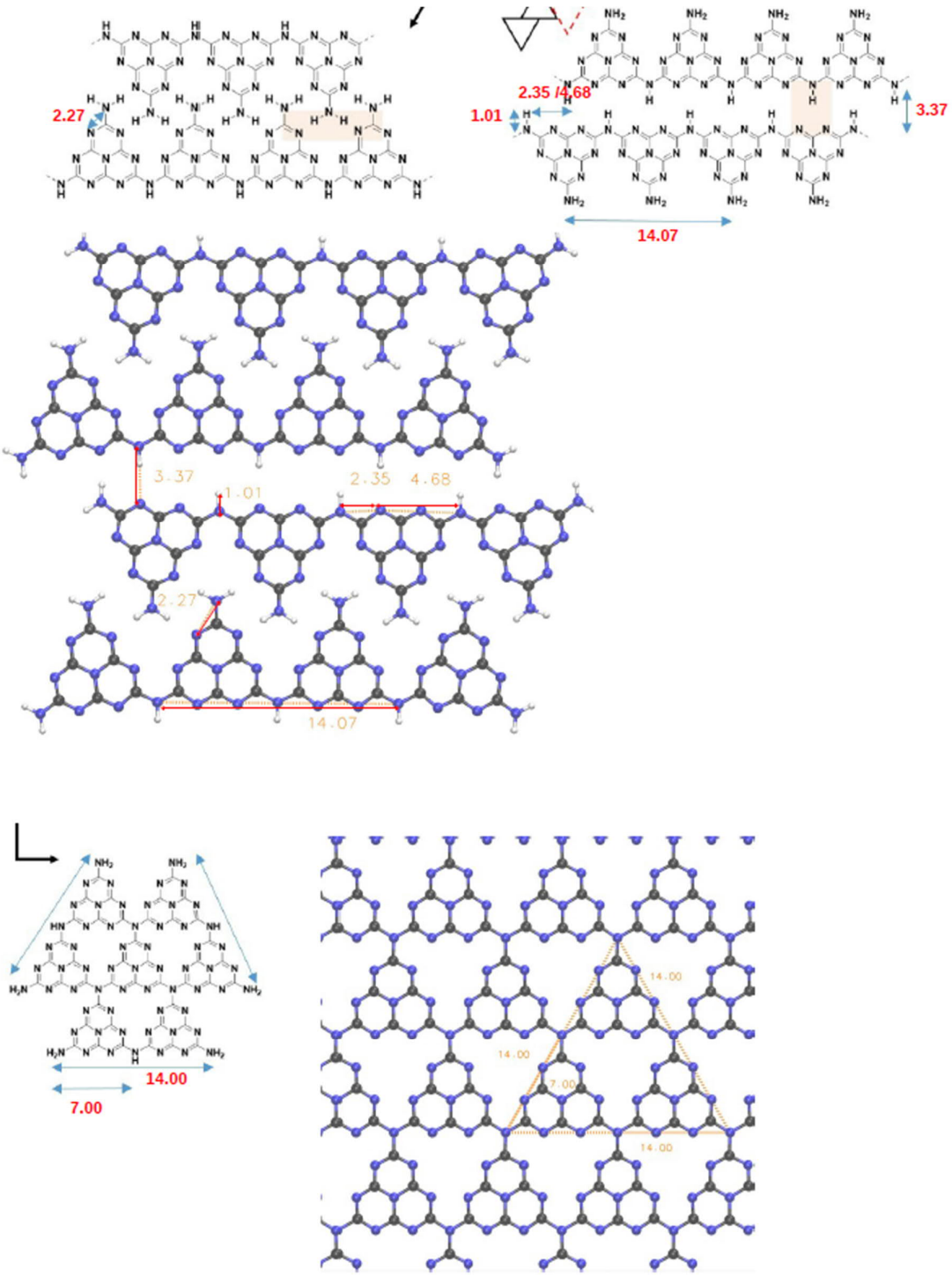

Figure A- 13: *DFT calculations of the interatomic distances for the pCN thin film structures observed in the low-temperature STM/nc-AFM images.*

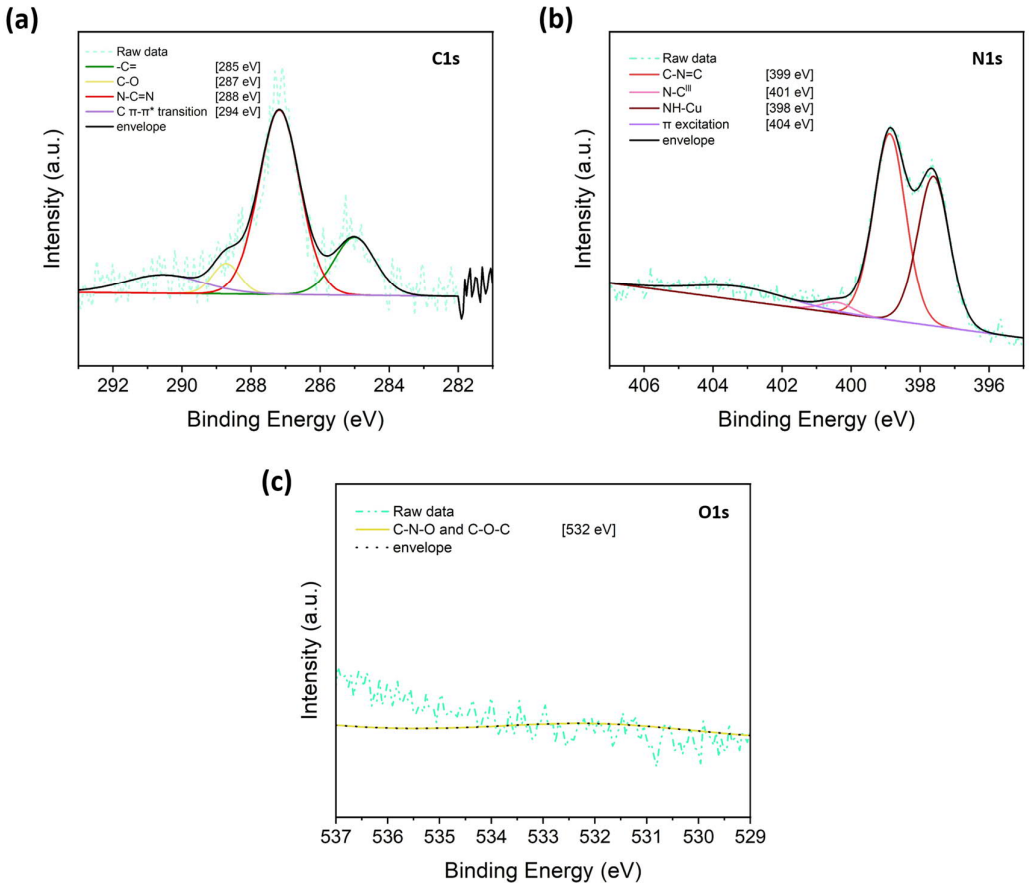

Figure A- 14: *XPS C1s, N1s, and O1s spectra of in-situ LT-STM/nc-AFM pCN sample on Cu(111) at the maximum deposition/annealing temperature supported by the system.*

Table A- 8: *Bonding types and composition as determined by the XPS spectra (C1s, N1s, and O1s) for in situ STM/nc-AFM pCN deposited on Cu(111) with maximum deposition/annealing temperature.*

In situ STM/nc-AFM pCN deposition/annealing on Cu (111)	
N-C=N (C1s)	33%
C-N=C (N1s)	36%
N-$(C)_3$ (N1s)	2%
NH-Cu (N1s)	29%
-C=/C_{all}	20%
O_{all}/C_{all}	-----

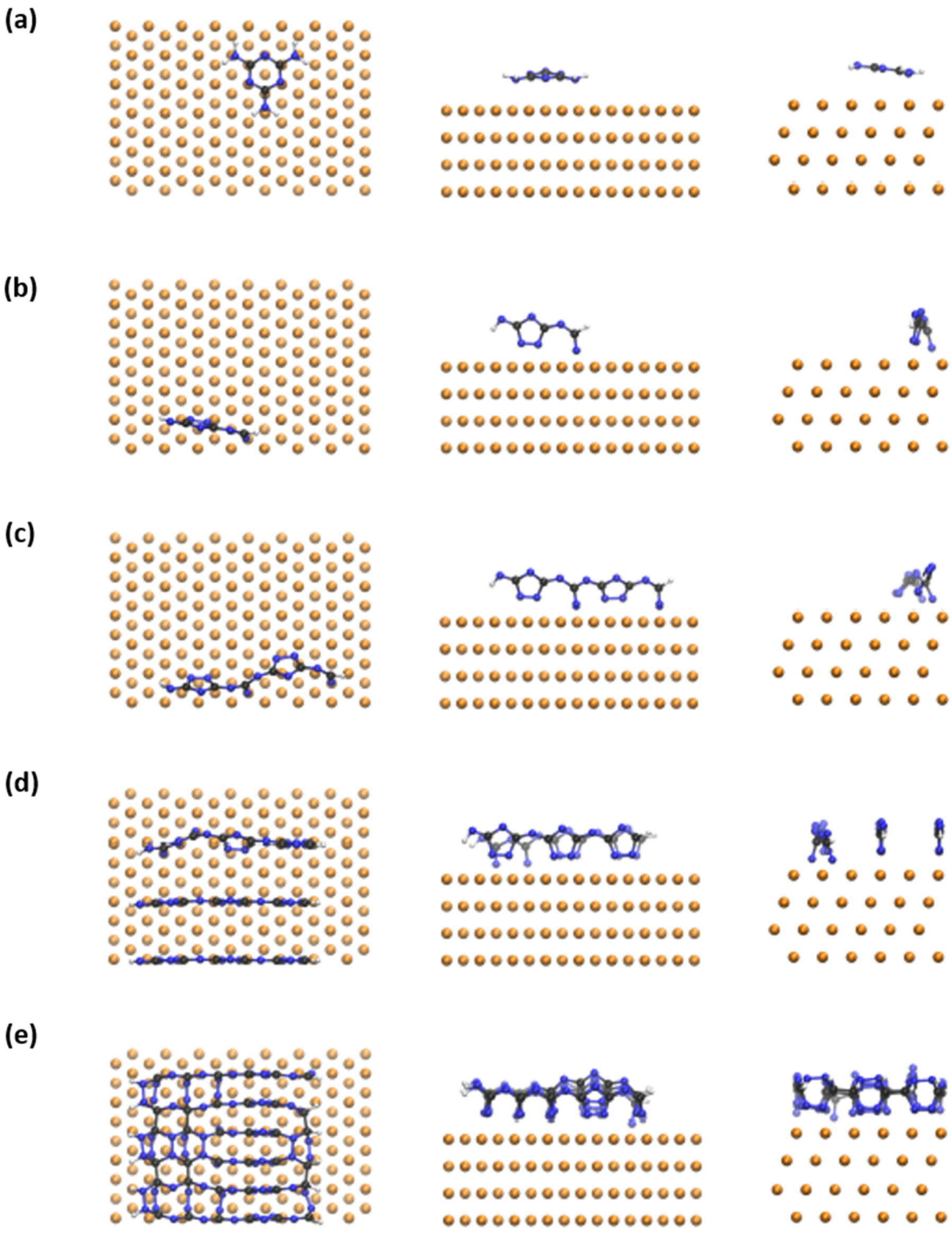

Figure A- 15: *Different structures adsorbed on Cu(111) surface. a) melamine, b) melamine after ring opening, c) dimer after ring opening, d,e) multiple dimers. Left images: top view, middle/right images: side views. Black: carbon, blue: nitrogen, orange: copper.*

Layer Commands: Add Delete Save
Include Surface Roughness = OFF
- Layer # 2 = Biaxial Thickness # 2 = 382.15 nm (MSA)
  Type = Uniaxial
  Optical Constants: Difference Mode = OFF
  - Ex = Gen-Osc
    Show Dialog
    - **e1 Components**
      Einf = 1.000
      UV Pole Amp. = 94.1439 UV Pole En. = 6.932
      IR Pole Amp. = 0.000
    - **e2 Components**
      Oscillator Menu: Add Delete Delete All Sort
      Fit Menu: All None Amp. Br. En.
      1: Type = Tauc-Lorentz Amp1 = 2.7107
      Br1 = 0.188 Eo1 = 3.728 Eg1 = 0.00
  - Ez = Gen-Osc
    Show Dialog
    - **e1 Components**
      Einf = 1.000
      UV Pole Amp. = 12.5677 UV Pole En. = 5.865
      IR Pole Amp. = 0.000
    - **e2 Components**
      Oscillator Menu: Add Delete Delete All Sort
      Fit Menu: All None Amp. Br. En.
      1: Type = Tauc-Lorentz Amp1 = 5.9649
      Br1 = 0.352 Eo1 = 6.820 Eg1 = 0.00
  Euler Angles: Phi = 0.00 Theta = 0.00
- Layer # 1 = SiO2 (Sellmeier) Thickness # 1 = 1988.77 nm
  Amp. = 0.756 Center En. = 0.10683 IR Pole Amp. = 0.00975
  Einf = 1.348
Substrate = Si_JAW

- **Multi Sample Analysis**

Add Fit Parameter Delete All Parms

Data Set	Thickness # 2
#1	389.98 nm
#2	374.80 nm
#3	340.62 nm
#4	382.15 nm

***Figure A- 16**: Ellipsometry fitting model (CompleteEASE software) for pCN thin film used for waveguide experiments. One Tauc-Lorentz oscillators was applied in the in-plane and two in the out-of-plane. The sample was measured with different focus spots and modeled using multi sample analysis.*

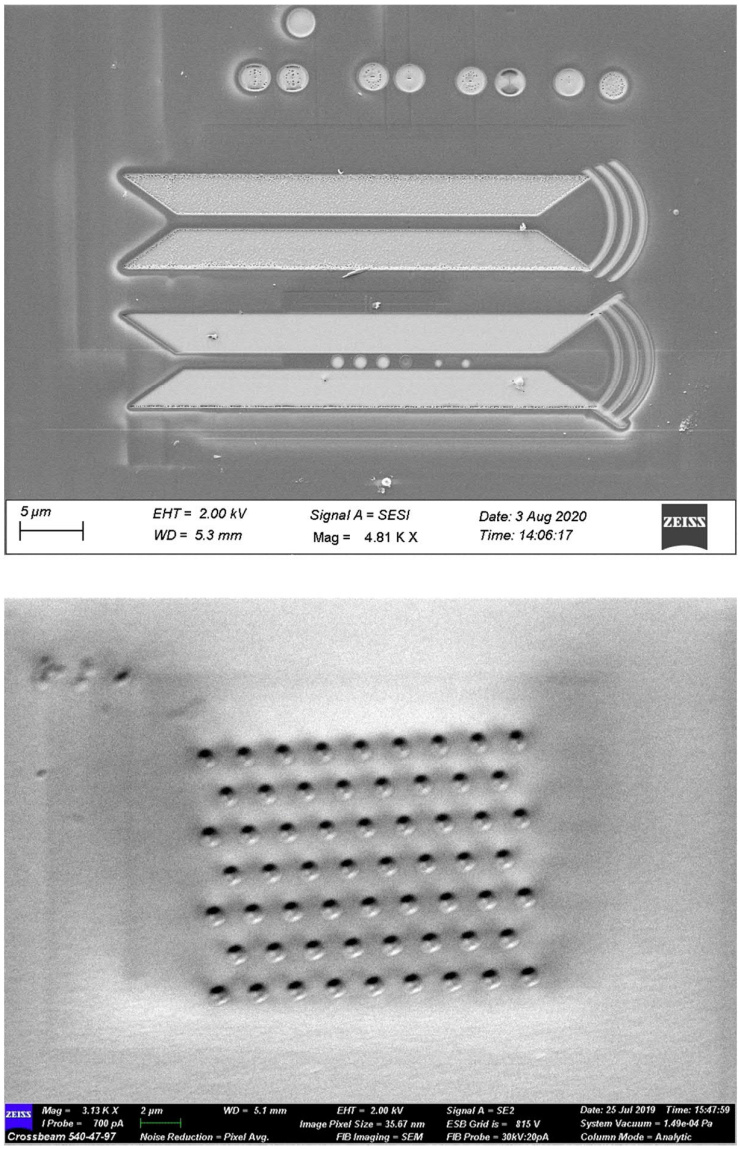

Figure A- 17: *Polymeric carbon nitride thin films patterned with focused ion beam (FIB). Optimal ion beam parameters: ion energy 30 kV, ion current 20 pA. Optimal processing parameters: dose 2.5 mC/cm^2, dose factor: 1, depth: set 120 nm, dwell time: 3.5 µs, mode: outside clockwise.*

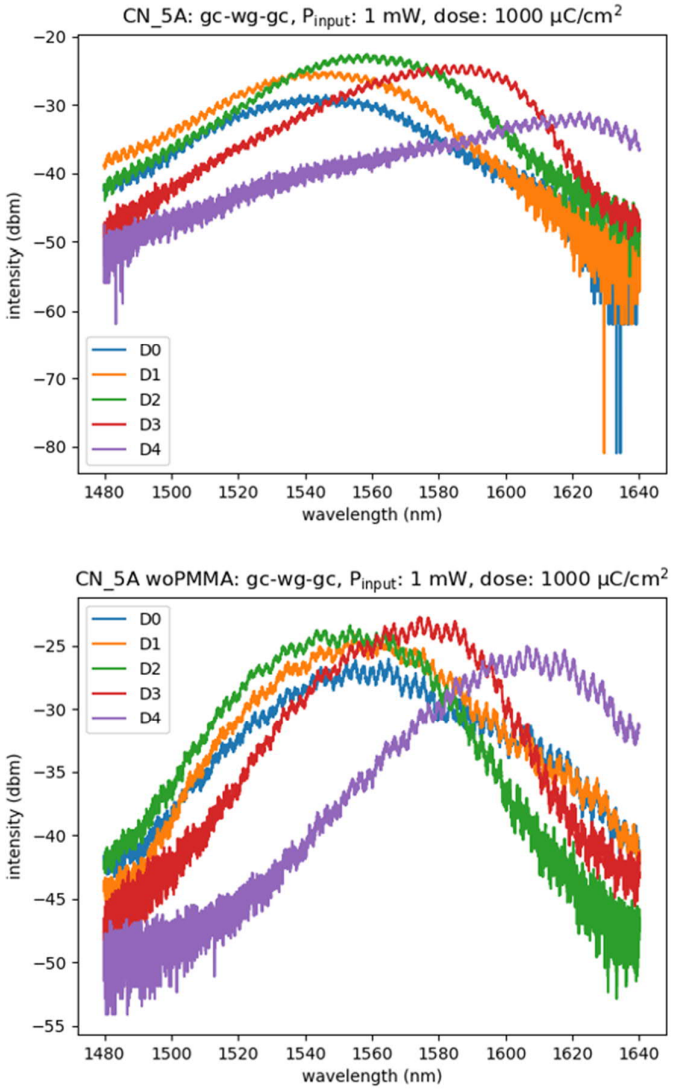

Figure A- 18: *Transmission spectra of the waveguides coupled to gratings with different fill factors (D is the period and the number, a certain filling).*

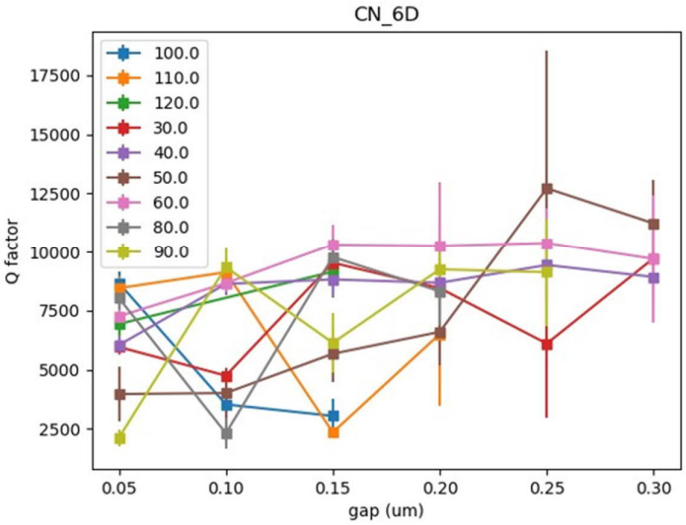

Figure A- 19: *Waveguide quality factor (Q-factor) as a function of the gap between the resonator and the waveguide.*

REFERENCES

1. Veselago, V. G. The Electrodynamics of Substances with Simultaneously negative values of ε and μ: Electromagnetic responses of relativistic electrons. *Sov. Phys. Usp* **10**, (1968).
2. Pendry, J. B. Negative Refraction Makes a Perfect Lens. *Phys. Rev. Lett.* **85**, 3966–3969 (2000).
3. Smith, D. R., Padilla, W. J., Vier, D. C., Nemat-Nasser, S. C. & Schultz, S. Composite Medium with Simultaneously Negative Permeability and Permittivity. *Phys. Rev. Lett.* **84**, 4184–4187 (2000).
4. Pendry, J. B., Holden, A. J., Robbins, D. J. & Stewart, W. J. Magnetism from conductors and enhanced nonlinear phenomena. *IEEE Trans. Microw. Theory Tech.* **47**, 2075–2084 (1999).
5. Liu, L., Kang, L., Mayer, T. S. & Werner, D. H. Hybrid metamaterials for electrically triggered multifunctional control. *Nat. Commun.* **7**, 13236 (2016).
6. Salvatore, S. *Optical Metamaterials by Block Copolymer Self-Assembly*. (2015).
7. Tanasković, D., Obradov, M., Jakšić, O. & Jakšić, Z. A low-loss double-fishnet metamaterial based on transparent conductive oxide. *Phys. Scr.* **T162**, 14048 (2014).
8. Vignolini, S. *et al.* A 3D optical metamaterial made by self-assembly. *Adv. Mater.* **24**, 23–27 (2012).
9. Capolino, F. *Theory and Phenomena of Metamaterials*. *Theory and Phenomena of Metamaterials* (2017).
10. Ghoshroy, A., Özdemir, Ş. K. & Güney, D. Ö. Loss compensation in metamaterials and plasmonics with virtual gain [Invited]. *Opt. Mater. Express* **10**, 1862 (2020).
11. Wuestner, S., Pusch, A., Tsakmakidis, K. L., Hamm, J. M. & Hess, O. Overcoming losses with gain in a negative refractive index metamaterial. *Phys. Rev. Lett.* **105**, 1–4 (2010).
12. Thomas, A. *et al.* Graphitic carbon nitride materials: Variation of structure and morphology and their use as metal-free catalysts. *J. Mater. Chem.* **18**, 4893–4908 (2008).
13. Giusto, P. *et al.* Shine Bright Like a Diamond: New Light on an Old Polymeric

Semiconductor. *Adv. Mater.* **32**, (2020).

14. Walser, R. M. *Electromagnetic metamaterials*. *Complex Mediums II: Beyond Linear Isotropic Dielectrics* vol. 4467 (2001).
15. Vohnsen, B. A short history of optics. *Phys. Scr. T* **T109**, 75–79 (2004).
16. Fowles, G. R. & Lynch, D. W. Introduction to Modern Optics. *American Journal of Physics* vol. 36 770–771 (1968).
17. Hecht, E. *Optics*. (Pearson, 2016).
18. M., S. V. Metamaterials: A New Paradigm of Physics and Engineering. (2008).
19. Jackson 1925-2016, J. D. *Classical electrodynamics*. (Third edition. New York : Wiley, [1999] ©1999).
20. Mohanty, S. P. *et al.* Waves in metamaterials. *AIP Conf. Proc.* **1832**, (2017).
21. Jackson, J. D. *Plane Electromagnetic Waves*. *Classical Electrodynamics* (1962).
22. Landau, L. D. The Classical Theory of Fields. *Nature* vol. 169 600 (1952).
23. Lucarini, V., Saatinen, J. J., Peiponen, K.-E. & Vartiainen, E. M. *Kramers-Kronig Relations in Optical Materials Research*. *Kramers-Kronig Relations in Optical Materials Research* (2005).
24. Jellison, G. E. & Modine, F. A. Parameterization of the optical functions of amorphous materials in the interband region. *Appl. Phys. Lett.* **371**, 69 (1996).
25. Levi, A. F. J. The Lorentz oscillator model. in *Essential Classical Mechanics for Device Physics* 5–21 (Morgan & Claypool Publishers, 2016).
26. Wooten, F. *Optical Properties of Solids*. *Academic Press, New York* (1972).
27. Kasap, S. & Capper, P. *Electronic and Photonic Materials*. *Springer Handbooks* (Springer Handbook of Electronic and Photonic Materials, 2017).
28. Tong, X. C. *Advanced Materials for Integrated Optical Waveguides*. *Springer Series in Advanced Microelectronics* vol. 46 (2014).
29. Zhang, C., Zhao, Y. S. & Yao, J. Optical waveguides at micro/nanoscale based on functional small organic molecules. *Phys. Chem. Chem. Phys.* **13**, 9060–9073 (2011).
30. Snyder, A. W. & Love, J. *Optical Waveguide Theory*. (Springer US, 1983).
31. Yeap, K. H., Teh, K. H., Yeong, K. C., Lai, K. C. & Loh, M. C. Propagation in dielectric rectangular waveguides. *Opt. Appl.* **46**, 317–330 (2016).
32. Goell, J. E. Rectangular Dielectric Waveguides. in *Introduction to Integrated Optics* (ed. Barnoski, M. K.) 73–103 (Springer US, 1974).

33. Jackson, M. J. *Micro and Nanomanufacturing*. (Springer US, 2007).
34. Kostic, I., Vutova, K., Koleva, E. & Andok, R. *Polymer science: research advances, practical applications and educational aspects - Chapter: Study on polymers with implementation in electron beam lithography*. (Formatex Research Center, 2016).
35. Murad, R. & Xichun, H. Promising Lithography Techniques for Next-Generation Logic Devices. *Nanomanufacturing Metrol.* **1**, 67–81 (2018).
36. Cui, Z. *Nanofabrication: Principles, Capabilities and Limits*. (Springer Science+Business Media, LLC, 2008).
37. Yan, S. C., Li, Z. S. & Zou, Z. G. Photodegradation Performance of g-C3N4 Fabricated by Directly Heating Melamine. *Langmuir* **25**, 10397–10401 (2009).
38. Wang, X. *et al.* Polymer Semiconductors for Artificial Photosynthesis: Hydrogen Evolution by Mesoporous Graphitic Carbon Nitride with Visible Light. *J. Am. Chem. Soc.* **131**, 1680–1681 (2009).
39. Bai, X. *et al.* A simple and efficient strategy for the synthesis of a chemically tailored g-C3N4 material. *J. Mater. Chem. A* **2**, 17521–17529 (2014).
40. Zhang, Y., Liu, J., Wu, G. & Chen, W. Porous graphitic carbon nitride synthesized via direct polymerization of urea for efficient sunlight-driven photocatalytic hydrogen production. *Nanoscale* **4**, 5300–5303 (2012).
41. Liebig, J. Uber einige Stickstoff-Verbindungen. *Ann. Der Pharm.* **10**, (1834).
42. Lotsch, B. V. & Schnick, W. From triazines to heptazines: Novel nonmetal tricyanomelaminates as precursors for graphitic carbon nitride materials. *Chem. Mater.* **18**, 1891–1900 (2006).
43. Liu, A. Y. & Cohen, M. L. Prediction of new low compressibility solids. *Science (80-.).* **245**, 841–842 (1989).
44. Fina, F., Callear, S. K., Carins, G. M. & Irvine, J. T. S. Structural investigation of graphitic carbon nitride via XRD and neutron diffraction. *Chem. Mater.* **27**, 2612–2618 (2015).
45. Lotsch, B. V. *et al.* Unmasking melon by a complementary approach employing electron diffraction, solid-state NMR spectroscopy, and theoretical calculations - Structural characterization of a carbon nitride polymer. *Chem. - A Eur. J.* **13**, 4969–4980 (2007).
46. Kessler, F. K. *et al.* Functional carbon nitride materials-design strategies for

electrochemical devices. *Nat. Rev. Mater.* **2**, (2017).

47. Wang, A., Wang, C., Fu, L., Wong-Ng, W. & Lan, Y. Recent Advances of Graphitic Carbon Nitride-Based Structures and Applications in Catalyst, Sensing, Imaging, and LEDs. *Nano-Micro Lett.* **9**, (2017).
48. Wang, X. *et al.* A metal-free polymeric photocatalyst for hydrogen production from water under visible light. *Nat. Mater.* **8**, 76–80 (2009).
49. Heavens, O. S. *Optical Properties of Thin Solid Films*. (Dover Publications, 1991).
50. Hummel, R. E. & Guenther, K. H. *Handbook of Optical Properties: Thin Films for Optical Coatings*. (Taylor & Francis, 1995).
51. Xu, W., Wang, L. & Kojima, I. Carbon nitride thin films prepared by radio-frequency magnetron sputtering combined with a nitrogen radical beam source. *J. Appl. Phys.* **94**, 7345–7350 (2003).
52. Sakamoto, Y. & Takaya, M. Growth of carbon nitride using microwave plasma CVD. *Thin Solid Films* **475**, 198–201 (2005).
53. Zocco, A. *et al.* Deposition of carbon nitride films by reactive pulsed-laser ablation at high fluences. *Diam. Relat. Mater.* **8**, 582–585 (1999).
54. Crunteanu, A. *et al.* Synthesis and characterization of carbon nitride thin films obtained by laser induced chemical vapour deposition. *Surf. Coatings Technol.* **125**, 301–307 (2000).
55. Jilani, A. *Advance Deposition Techniques for Thin Film and Coating*. (IntechOpen, 2017).
56. Urakami, N., Kosaka, M. & Hashimoto, Y. Thermal chemical vapor deposition and luminescence property of graphitic carbon nitride film for carbon-based semiconductor systems. *Jpn. J. Appl. Phys.* **58**, 10907 (2018).
57. Pierson, H. O. *Handbook of Chemical Vapor Deposition, 2nd Edition: Principles, Technology and Applications*. (Elsevier Science, 1999).
58. Jones, A. C. & Hitchman, M. L. *Chemical Vapour Deposition: Precursors, Processes and Applications*. (Royal Society of Chemistry, 2009).
59. Munson, B. R., Rothmayer, A. P. & Okiishi, T. H. *Fundamentals of Fluid Mechanics, 7th Edition*. (Wiley, 2012).
60. Kee, R. J., Coltrin, M. E. & Glarborg, P. *Chemically Reacting Flow: Theory and Practice*. (Wiley, 2005).

61. Nazabal, V. & Němec, P. Amorphous Thin Film Deposition. in *Springer Handbook of Glass* (eds. Musgraves, J. D., Hu, J. & Calvez, L.) 1293–1332 (Springer International Publishing, 2019).
62. Ohring, M. & (Firm), K. *Materials Science of Thin Films*. (Elsevier Science, 2002).
63. Kolasinski, K. W. *Surface Science: Foundations of Catalysis and Nanoscience*. (Wiley, 2019).
64. Ravindra, N. M., Ganapathy, P. & Choi, J. Energy gap-refractive index relations in semiconductors - An overview. *Infrared Phys. Technol.* **50**, 21–29 (2007).
65. Wang, X., Martin, P. J. & Kinder, T. J. Optical and mechanical properties of carbon nitride films prepared by ion-assisted arc deposition and magnetron sputtering. *Thin Solid Films* **256**, 148–154 (1995).
66. Lu, Y. F., Ren, Z. M., Song, W. D. & Chan, D. S. H. Electronic and optical properties of carbon nitride thin films synthesized by laser ablation under ion beam bombardment. *J. Appl. Phys.* **84**, 2133–2137 (1998).
67. Balaceanu, M., Grigore, E., Pavelescu, G., Ionescu, F. & Roger, J. P. Optical characteristics of carbon nitride films prepared by hollow cathode discharge. *J. Optoelectron. Adv. Mater.* **2**, 351–355 (2000).
68. Broitman, E. *et al.* Electrical and optical properties of CNx($0 \leq x \leq 0.25$) films deposited by reactive magnetron sputtering. *J. Appl. Phys.* **89**, 1184–1190 (2001).
69. Majumdar, A., Bogdanowicz, R. & Hippler, R. Ellipsometric study of carbon nitride films deposited by DC-magnetron sputtering. *Photonics Lett. Pol.* **3**, 70–72 (2011).
70. Miyajima, Y. *et al.* Electronic state modification in laser deposited amorphous carbon films by the inclusion of nitrogen. *J. Appl. Phys.* **104**, (2008).
71. Alibart, F. *et al.* Comparison and semiconductor properties of nitrogen doped carbon thin films grown by different techniques. *Appl. Surf. Sci.* **254**, 5564–5568 (2008).
72. Rodil, S. E., Muhl, S., Maca, S. & Ferrari, A. C. Optical gap in carbon nitride films. *Thin Solid Films* **433**, 119–125 (2003).
73. Hu, J., Yang, P. & Lieber, C. M. Nitrogen driven structural transformation in carbon nitride materials. *Appl. Surf. Sci.* **127**–**129**, 569–573 (1998).
74. Ferrari, A. C. Non-destructive Characterisation of Carbon Films. in *Tribology of Diamond-Like Carbon Films: Fundamentals and Applications* (eds. Donnet, C. & Erdemir, A.) 25–82 (Springer US, 2008).

75. Wei, W. & Jacob, T. Strong excitonic effects in the optical properties of graphitic carbon nitride g -C 3 N 4 from first principles. **085202**, 1–7 (2013).
76. Fujita, S., Habuchi, H., Takagi, S. & Takikawa, H. Diamond & Related Materials Optical properties of graphitic carbon nitride fi lms prepared by evaporation. *Diam. Relat. Mater.* **65**, 83–86 (2016).
77. Miller, T. S. *et al.* Carbon nitrides: Synthesis and characterization of a new class of functional materials. *Phys. Chem. Chem. Phys.* **19**, 15613–15638 (2017).
78. Huettel, I., Cerny, F., Gurovic, J., Chomat, M. & Matejec, V. Thin carbon nitride films for integrated optical chemical sensors. *Adv. Mater. Opt. Syst. Chem. Biol. Detect.* **3858**, 210 (1999).
79. Gioti, M. & Logothetidis, S. Dielectric function, electronic properties and optical constants of amorphous carbon and carbon nitride films. *Diam. Relat. Mater.* **12**, 957–962 (2003).
80. Thomas, A. *et al.* Graphitic carbon nitride materials : variation of structure and morphology and their use as metal-free catalysts. 4893–4908 (2008)
81. Yokoyama, D., Sakaguchi, A., Suzuki, M. & Adachi, C. Horizontal orientation of linear-shaped organic molecules having bulky substituents in neat and doped vacuum-deposited amorphous films. *Org. Electron.* **10**, 127–137 (2009).
82. Oh-E, M., Ogata, H., Fujita, Y. & Koden, M. Anisotropy in amorphous films of cross-shaped molecules with an accompanying effect on carrier mobility: Ellipsometric and sum-frequency vibrational spectroscopic studies. *Appl. Phys. Lett.* **102**, (2013).
83. Lin, H. W. *et al.* Anisotropic optical properties and molecular orientation in vacuum-deposited ter(9,9-diarylfluorene)s thin films using spectroscopic ellipsometry. *J. Appl. Phys.* **95**, 881–886 (2004).
84. Yokoyama, D., Sakaguchi, A., Suzuki, M. & Adachi, C. Horizontal molecular orientation in vacuum-deposited organic amorphous films of hole and electron transport materials. *Appl. Phys. Lett.* **93**, 1–4 (2008).
85. Tammer, M., Higgins, R. W. T. & Monkman, A. P. High optical anisotropy in thin films of polyfluorene and its affect on the outcoupling of light in typical polymer light emitting diode structures. *J. Appl. Phys.* **91**, 4010–4013 (2002).
86. Jones, R. L., Kumar, S. K., Ho, D. L., Briber, R. M. & Russell, T. P. Chain conformation in ultrathin polymer films. *Nature* **400**, 146–149 (1999).

87. McBranch, D., Campbell, I. H., Smith, D. L. & Ferraris, J. P. Optical determination of chain orientation in electroluminescent polymer films. *Appl. Phys. Lett.* **1175**, 1175 (1995).
88. Fujiwara, H. *Spectroscopic Ellipsometry: Principles and Applications*. (Wiley, 2007).
89. Chemical Vapor Deposition. in *Handbook of Nanophase and Nanostructured Materials* (eds. Wang, Z. L., Liu, Y. & Zhang, Z.) 102–144 (Springer US, 2002).
90. Vossen, J. L., Kern, W., Kern, W., Werner Kern, chimiste & (Firm), K. *Thin Film Processes II*. (Academic Press, 1991).
91. Hellgren, N., Haasch, R. T., Schmidt, S., Hultman, L. & Petrov, I. Interpretation of X-ray photoelectron spectra of carbon-nitride thin films: New insights from in situ XPS. *Carbon N. Y.* **108**, 242–252 (2016).
92. Akaike, K., Aoyama, K., Dekubo, S., Onishi, A. & Kanai, K. Characterizing Electronic Structure near the Energy Gap of Graphitic Carbon Nitride Based on Rational Interpretation of Chemical Analysis. *Chem. Mater.* **30**, 2341–2352 (2018).
93. Zambon, A. *et al.* S-Heptazine oligomers: Promising structural models for graphitic carbon nitride. *Chem. Sci.* **7**, 945–950 (2016).
94. Rosu, D. M. *et al.* Molecular Orientation in Octanedithiol and Hexadecanethiol Monolayers on GaAs and Au Measured by Infrared Spectroscopic Ellipsometry. *Langmuir* **25**, 919–923 (2009).
95. Parikh, A. N. & Allara, D. L. Quantitative determination of molecular structure in multilayered thin films of biaxial and lower symmetry from photon spectroscopies. I. Reflection infrared vibrational spectroscopy. *J. Chem. Phys.* **96**, 927–945 (1992).
96. Debe, M. K. Extracting physical structure information from thin organic films with reflection absorption infrared spectroscopy. *J. Appl. Phys.* **55**, 3354–3366 (1984).
97. Jürgens, B. *et al.* Melem (2,5,8-triamino-tri-s-triazine), an important intermediate during condensation of melamine rings to graphitic carbon nitride: Synthesis, structure determination by x-ray powder diffractometry, solid-state NMR, and theoretical studies. *J. Am. Chem. Soc.* **125**, 10288–10300 (2003).
98. Zimmerman, J. L., Williams, R., Khabashesku, V. N. & Margrave, J. L. Synthesis of Spherical Carbon Nitride Nanostructures. *Nano Lett.* **1**, 731–734 (2001).
99. Karabacak, T. Thin-film growth dynamics with shadowing and re-emission effects. *J. Nanophotonics* **5**, 1–19 (2011).

100. Rockett, A. *The Materials Science of Semiconductors*. (Springer US, 2007).
101. Zhao, Y. Dynamic Shadowing Growth and Its Energy Applications. *Front. Energy Res.* **2**, 38 (2014).
102. Chowdhury, S., Laugier, M. T. & Rahman, I. Z. Measurement of the mechanical properties of carbon nitride thin films from the nanoindentation loading curve. *Diam. Relat. Mater.* **13**, 1543–1548 (2004).
103. Bourgeois, A., Turcant, Y., Walsh, C. & Defranoux, C. Ellipsometry porosimetry (EP): thin film porosimetry by coupling an adsorption setting with an optical measurement, highlights on additional adsorption results. *Adsorption* **14**, 457–465 (2008).
104. Sanchez, C., Boissière, C., Grosso, D., Laberty, C. & Nicole, L. Design, synthesis, and properties of inorganic and hybrid thin films having periodically organized nanoporosity. *Chem. Mater.* **20**, 682–737 (2008).
105. Boissiere, C. *et al.* Porosity and mechanical properties of mesoporous thin films assessed by environmental ellipsometric porosimetry. *Langmuir* **21**, 12362–12371 (2005).
106. Bowden, N., Brittain, S., Evans, A. G., Hutchinson, J. W. & Whitesides, G. M. Spontaneous formation of ordered structures in thin films of metals supported on an elastomeric polymer. *Nature* **393**, 146–149 (1998).
107. Yu, H. & Hutchinson, J. W. Delamination of thin film strips. **423**, 54–63 (2003).
108. Yu, H. H., He, M. Y. & Hutchinson, J. W. EDGE EFFECTS IN THIN FILM DELAMINATION. **49**, 93–107 (2001).
109. Aarik, J. *et al.* Influence of carrier gas pressure and flow rate on atomic layer deposition of HfO2 and ZrO2 thin films. *Appl. Surf. Sci.* **252**, 5723–5734 (2006).
110. Gross, L., Mohn, F., Moll, N., Liljeroth, P. & Meyer, G. The Chemical Structure of a Molecule Resolved by Atomic Force Microscopy. *Science (80-.).* **325**, 1110–1114 (2009).
111. Yesilpinar, D. *et al.* High resolution noncontact atomic force microscopy imaging with oxygen-terminated copper tips at 78 K. *Nanoscale* **12**, 2961–2965 (2020).
112. Mönig, H. *et al.* Quantitative assessment of intermolecular interactions by atomic force microscopy imaging using copper oxide tips. *Nat. Nanotechnol.* **13**, 371–375 (2018).
113. Mohn, F., Schuler, B., Gross, L. & Meyer, G. Different tips for high-resolution atomic force microscopy and scanning tunneling microscopy of single molecules. *Appl. Phys.*

Lett. **102**, 73109 (2013).

114. Moll, N., Gross, L., Mohn, F., Curioni, A. & Meyer, G. The mechanisms underlying the enhanced resolution of atomic force microscopy with functionalized tips. *New J. Phys.* **12**, 125020 (2010).
115. Gross, L. *et al.* Bond-Order Discrimination by Atomic Force Microscopy. *Science (80-.).* **337**, 1326–1329 (2012).
116. Mönig, H. Copper-oxide tip functionalization for submolecular atomic force microscopy. *Chem. Commun.* **54**, 9874–9888 (2018).
117. Sweetman, A. M. *et al.* Mapping the force field of a hydrogen-bonded assembly. *Nat. Commun.* **5**, (2014).
118. Huber, F. *et al.* Intramolecular Force Contrast and Dynamic Current-Distance Measurements at Room Temperature. *Phys. Rev. Lett.* **115**, 1–4 (2015).
119. Mönig, H. Copper-oxide tip functionalization for submolecular atomic force microscopy. *Chem. Commun.* **54**, 9874–9888 (2018).
120. Morita, S., Giessibl, F. J. & Wiesendanger, R. *Noncontact Atomic Force Microscopy: Volume 2*. (Springer Berlin Heidelberg, 2009).
121. Giessibl, F. J. Advances in atomic force microscopy. *Rev. Mod. Phys.* **75**, 949–983 (2003).
122. Silly, F. *et al.* Melamine structures on the Au(111) surface. *J. Phys. Chem. C* **112**, 11476–11480 (2008).
123. Lin, Y. P. *et al.* Self-assembled melamine monolayer on Cu(111). *J. Phys. Chem. C* **117**, 9895–9902 (2013).
124. Wang, L. *et al.* Thickness-Dependent Adsorption of Melamine on Cu/Au(111) Films. *J. Phys. Chem. C* **121**, 7977–7984 (2017).
125. Lübbe, J. *et al.* Achieving high effective Q-factors in ultra-high vacuum dynamic force microscopy. *Meas. Sci. Technol.* **21**, (2010).
126. Björk, J. *et al.* STM fingerprint of molecule-adatom interactions in a self-assembled metal-organic surface coordination network on Cu(111). *Phys. Chem. Chem. Phys.* **12**, 8815–8821 (2010).
127. Zhang, H. *et al.* Surface supported gold-organic hybrids: On-surface synthesis and surface directed orientation. *Small* **10**, 1361–1368 (2014).
128. Feng, D., Zhou, Z. & Bo, M. An investigation of the thermal degradation of melamine

phosphonite by XPS and thermal analysis techniques. *Polym. Degrad. Stab.* **50**, 65–70 (1995).

129. Davies, P. R., Edwards, D. & Richards, D. STM and XPS Studies of the Oxidation of Aniline at Cu(110) Surfaces. *J. Phys. Chem. B* **108**, 18630–18639 (2004).
130. Lin, Y.-P. *et al.* Self-Assembled Melamine Monolayer on Cu(111). *J. Phys. Chem. C* **117**, 9895–9902 (2013).
131. Bettotti, P. Hybrid Materials for Integrated Photonics. *Adv. Opt.* **2014**, 891395 (2014).
132. Jiao, Y. *et al.* InP membrane integrated photonics research. *Semicond. Sci. Technol.* **36**, (2020).
133. Dai, D. & He, S. A silicon-based hybrid plasmonic waveguide with a metal cap for a nano-scale light confinement. *Opt. Express* **17**, 16646–16653 (2009).
134. Grote, R. R. & Bassett, L. C. Single-mode optical waveguides on native high-refractive-index substrates. *APL Photonics* **1**, 71302 (2016).
135. Beecroft, L. L. & Ober, C. K. High refractive index polymers for optical applications. *J. Macromol. Sci. - Pure Appl. Chem.* **34**, 573–586 (1997).
136. Liu, J. G. & Ueda, M. High refractive index polymers: Fundamental research and practical applications. *J. Mater. Chem.* **19**, 8907–8919 (2009).
137. Badur, T., Dams, C. & Hampp, N. High Refractive Index Polymers by Design. *Macromolecules* **51**, 4220–4228 (2018).
138. Zhou, M. Low-loss polymeric materials for passive waveguide components in fiber optical telecommunication. *Opt. Eng.* **41**, 1631 (2002).
139. Bojko, R. J. *et al.* Electron beam lithography writing strategies for low loss, high confinement silicon optical waveguides. *J. Vac. Sci. Technol. B, Nanotechnol. Microelectron. Mater. Process. Meas. Phenom.* **29**, 06F309 (2011).
140. Cardenas, J. *et al.* Low loss etchless silicon photonic waveguides. *Opt. Express* **17**, 4752–4757 (2009).
141. Sparacin, D. K., Spector, S. J. & Kimerling, L. C. Silicon Waveguide Sidewall Smoothing by Wet Chemical Oxidation. *J. Light. Technol.* **23**, 2455 (2005).
142. Urbonas, D. & Mahrt, R. F. Low-loss optical waveguides made with a high-loss material. *Light Sci. Appl.* (2021).
143. Vlasov, Y. A. & McNab, S. J. Losses in single-mode silicon-on-insulator strip waveguides and bends. *Opt. Express* **12**, 1622 (2004).

144. Vlugter, P., Block, E. & Bellouard, Y. Local tuning of fused silica thermal expansion coefficient using femtosecond laser. *Phys. Rev. Mater.* **3**, 1–8 (2019).
145. Ast, D., Nemchuk, N. & Krasula, S. *Low-Cost Glass and Glass- Ceramic Substrates for Thin- Film Silicon Solar Cells*. (2002).
146. Satyalakshmi, K. M. *et al.* Charge induced pattern distortion in low energy electron beam lithography. *J. Vac. Sci. Technol. B Microelectron. Nanom. Struct. Process. Meas. Phenom.* **18**, 3122–3125 (2000).
147. Arat, K. T. *et al.* Charge-induced pattern displacement in E-beam lithography. *J. Vac. Sci. Technol. B* **37**, 51603 (2019).
148. Joo, J., Chow, B. Y. & Jacobson, J. M. Nanoscale patterning on insulating substrates by critical energy electron beam lithography. *Nano Lett.* **6**, 2021–2025 (2006).
149. Kim, D. H. *et al.* One-step vapor-phase synthesis of transparent high refractive index sulfur-containing polymers. *Sci. Adv.* **6**, 1–9 (2020).
150. Flaim, T. D., Wang, Y. & Mercado, R. High-refractive-index polymer coatings for optoelectronics applications. *Adv. Opt. Thin Film.* **5250**, 423 (2004).
151. Melloni, A. The role of index contrast in dielectric optical waveguides. *Int. J. Mater. Prod. Technol.* **34**, 421–437 (2009).
152. Ebeling, K. J. Strip Waveguides. in *Integrated Optoelectronics: Waveguide Optics, Photonics, Semiconductors* 75–108 (Springer Berlin Heidelberg, 1993).
153. Kogelnik, H. Theory of Optical Waveguides. in *Guided-Wave Optoelectronics* (ed. Tamir, T.) 7–88 (Springer Berlin Heidelberg, 1988).
154. Manià, L., Corzani, T. & Valentinuzzi, E. The Finite Element Method in the Analysis of Optical Waveguides. in *Integrated Optics: Physics and Applications* (eds. Martellucci, S. & Chester, A. N.) 335–359 (Springer US, 1983).
155. Chen, X., Li, C. & Tsang, H. K. Fabrication-Tolerant Waveguide Chirped Grating Coupler for Coupling to a Perfectly Vertical Optical Fiber. *IEEE Photonics Technol. Lett.* **20**, 1914–1916 (2008).
156. Wuestner, S., Pusch, A., Tsakmakidis, K. L., Hamm, J. M. & Hess, O. Dynamics of light amplification and gain in nano-plasmonic fishnet metamaterials. in *Active Photonic Materials IV* (eds. Subramania, G. S. & Foteinopoulou, S.) vol. 8095 11–21 (SPIE, 2011).
157. Hamm, J. M., Wuestner, S., Tsakmakidis, K. L. & Hess, O. Theory of Light

Amplification in Active Fishnet Metamaterials. *Phys. Rev. Lett.* **107**, 167405 (2011).

158. Zhang, S. *et al.* Near-infrared double negative metamaterials. *Opt. Express* **13**, 4922–4930 (2005).
159. Xiao, S. *et al.* Loss-free and active optical negative-index metamaterials. *Nature* **466**, 735–738 (2010).
160. Valentine, J. *et al.* Three-dimensional optical metamaterial with a negative refractive index. *Nature* **455**, 376–379 (2008).
161. Feynman, R. P. There's plenty of room at the bottom. *Resonance* **16**, 890 (2011).
162. Hutcheson, G. D. The Economic Implications of Moore ' s Law. in *Into the Nano Era: Moore's Law Beyond Planar Silicon CMOS* (eds. Huff, H., R.M. Osgood, J., Parisi, J. & Warlimont, H.) (Springer Series in Materials Science, 2009).
163. Moore's deviation. *Nat. Nanotechnol.* **12**, 1105 (2017).
164. Moore, G. E. Progress in digital integrated electronics [Technical literaiture, Copyright 1975 IEEE. Reprinted, with permission. Technical Digest. International Electron Devices Meeting, IEEE, 1975, pp. 11-13.]. *IEEE Solid-State Circuits Soc. Newsl.* **11**, 36–37 (2006).
165. Moore, G. E. Lithography and the future of Moore's law. in *Optical/Laser Microlithography VIII* (ed. Brunner, T. A.) vol. 2440 2–17 (SPIE, 1995).
166. Negara, C. Fast Polarization State Detection by Division-of-Amplitude in a Simple Configuration Setup Fast Polarization State Detection by Division-of-Amplitude in a Simple Configuration Setup Introduction. (2019).
167. Tompkins, H. G. & Irene, E. A. *Handbook of Ellipsometry*. (Springer Berlin Heidelberg, 2005).
168. Zambonin, P. G. & Desimoni, E. X-Ray Photoelectron Spectroscopy: Principles, Instrumentation, Data Processing and Molten Salt Applications. in *Molten Salt Chemistry: An Introduction and Selected Applications* (eds. Mamantov, G. & Marassi, R.) 425–445 (Springer Netherlands, 1987).
169. Bluhm, H. X-ray photoelectron spectroscopy (XPS) for in situ characterization of thin film growth. *Situ Charact. Thin Film Growth* 75–98 (2011).
170. Goldstein, J. *et al. Scanning Electron Microscopy and X-Ray Microanalysis: Third Edition*. (Springer US, 2003).
171. Ayache, J., Beaunier, L., Boumendil, J., Ehret, G. & Laub, D. *Sample Preparation*

Handbook for Transmission Electron Microscopy: Methodology. (Springer New York, 2014).

172. Ul-Hamid, A. Contrast Formation in the SEM. in *A Beginners' Guide to Scanning Electron Microscopy* 77–128 (Springer International Publishing, 2018).
173. Voigtländer, B. *Scanning Probe Microscopy: Atomic Force Microscopy and Scanning Tunneling Microscopy*. (Springer Berlin Heidelberg, 2015).
174. Lee, M. *X-Ray Diffraction for Materials Research: From Fundamentals to Applications*. (Apple Academic Press, 2017).
175. Suryanarayana, C. & Norton, M. G. *X-Ray Diffraction: A Practical Approach*. (Springer US, 2013).
176. Pandey, A., Dalal, S., Dutta, S. & Dixit, A. Structural characterization of polycrystalline thin films by X-ray diffraction techniques. *J. Mater. Sci. Mater. Electron.* **32**, 1341–1368 (2021).
177. Ruland, W. & Smarsly, B. X-ray scattering of non-graphitic carbon: An improved method of evaluation. *J. Appl. Crystallogr.* **35**, 624–633 (2002).